Influence of Temperature and Stress on the Durability of Carbon Fiber Reinforced Polymer (CFRP) Strands in a Concrete Environment

---

A Thesis

Presented to
the faculty of the School of Engineering and Applied Science
University of Virginia

---

in partial fulfillment
of the requirements for the degree

Master of Science

by

Jonathon D. Tanks

May

2015

APPROVAL SHEET

The thesis
is submitted in partial fulfillment of the requirements
for the degree of

Master of Science

AUTHOR

The thesis has been read and approved by the examining committee:

Devin K. Harris

Advisor

Jose P. Gomez

Lindsay Ivey-Burden

Accepted for the School of Engineering and Applied Science:

James H. Ay

Dean, School of Engineering and Applied Science

May

2015

ABSTRACT

One of the main causes of structural deficiency in concrete bridges is the deterioration of the constituent materials. In order to achieve the goal of 75-100 year design lives, it is imperative that prestressed elements—girders, piles, and deck panels—contain corrosion-resistant strands. VDOT has started pursuing carbon fiber reinforced polymers (CFRP) as a corrosion-resistant alternative to steel prestressing materials for longer lasting concrete bridge structures in Virginia

The in-service performance of CFRP rods and cables can be hard to evaluate in certain structural applications, such as prestressed concrete bridges, where instrumentation is often limited and the material cannot be removed for inspection. To implement CFRP in prestressed concrete bridge structures with more confidence, this project was initiated to study issues pertaining to durability under in-service environmental conditions. Specifically, the intention was to extract some information about fundamental material behavior while contributing directly to engineering applications in VDOT and beyond. The main goal was to investigate the effects of temperature, alkaline and alkaline/chloride solutions, and temporary stress on material properties over time, in the context of reinforced and prestressed concrete structures.

The methodology was designed to examine any relationships that exist between various observations and material characteristics, including moisture content, glass transition temperature, interlaminar/intralaminar shear strength, and tensile properties. This approach will also help to establish a durability testing methodology for CFRP in concrete structures that can be adopted by VDOT and other laboratories.

There were several key findings from the results of this study: (1) pre-loading the CFRP to 75% of the ultimate strength—temporarily, not sustained—has a significant impact on durability compared to unstressed material; (2) higher temperatures accelerate degradation, (3) moisture sorption was the primary process responsible for the observed degradation, with plasticization and microcracking as the controlling mechanisms leading to fiber-matrix interfacial debonding, and (4) a new mechanistic analytical model was developed to predict residual properties after moisture-induced degradation, showing promising agreement with experimental data.

Keywords: *Carbon fiber reinforced polymers; environmental durability; structural composites.*

Table of Contents

Acknowledgements

I would first like to thank my supervisor from the Virginia Center for Transportation Innovation & Research (VCTIR), Steve Sharp. His mentorship and guidance over the last few years has been instrumental in my development as a researcher, and I could not have accomplished this project without his help. I owe many thanks to my advisor at UVA, Prof. Devin Harris, for his patience and help as I am the "oddball" of the group: working at VCTIR, and studying composites. I hope to adopt his style as a professor one day, and I look forward to meeting again as professional peers.

Great thanks to my committee: Dr. Jose Gomez, Prof. Harris, and Prof. Lindsay Ivey-Burden.

I would also like to express my deepest thanks to those at VCTIR who helped me continuously over the course of this project: Bill Ordel trained me on every single piece of equipment used at VCTIR and I could always go to him for help or suggestions in the laboratory; Dr. Celik Ozyildirim gave encouragement and helpful ideas when I hit roadblocks, reminding me of the practical aspects of our research; Mike Burton was very patient and helpful when I used space and resources from his lab; and students Kate Rader, Ethan Bradshaw, and Constance Tan helped enormously when I needed it.

From UVA, thanks go to Richard White from MSE for his help and resources with the microscopes. Professors Brian Smith and Tom Baber, thanks for influencing me during my time at UVA.

I could not have asked for better classmates and colleagues at UVA: Ethan Bradshaw, Evelina Khakimova, Keenan Parker, Mohamad Shawki Amine, Mark Saliba, Sherif Daghash, Muhammad Sherif, John Civitillo, and Lauren Bolton. Whether it was helping each other in the lab, playing pick-up soccer at The Park, or going out to dinner, you guys made this experience so much more enjoyable and memorable—I sincerely hope our paths cross continuously in the future.

Of course, I must sincerely thank my family for their love, encouragement, and support—especially my mother, grandparents, sisters Jordan and Sydney, my father, and stepmother. My wife Schianne has been so patient, loving, and supportive throughout this project—without her, there is no way I could have accomplished this while still enjoying life. My two "brothers", Michael and Peter: thanks for being the best friends I could ask for. Above all, I thank God for his love, guidance, and inspiration.

Finally, I would like to thank VCTIR/VDOT for the financial support to complete this research project, for the benefit of the Virginia Commonwealth, and ultimately for anyone this affects.

LIST OF TABLES

LIST OF FIGURES

CHAPTER 1: INTRODUCTION

1.1 General Introduction

One of the main causes of structural deficiency in concrete bridges is the deterioration of the constituent materials. The concrete itself can experience deterioration mechanisms such as service-load cracking, scaling, and delamination, but one of the leading causes of concrete cracking and deterioration is the corrosion of steel reinforcement [1]. The increasing costs associated with maintaining and repairing concrete bridges as a result of corrosion can outweigh the initial construction costs by as much as two to five times [2]. Since corrosion has a more critical impact on steel subjected to high levels of sustained stress, it is especially important to use corrosion-resistant material for prestressing tendons. A severe case is the external prestressing strands shown in the pile in Figure 1. The Virginia Department of Transportation (VDOT) has transitioned from epoxy-coated reinforcement in decks to corrosion-resistant reinforcement (CRR) as a way to mitigate deck maintenance costs and extend the service lives of bridges. However, in order to achieve the goal of 75-100 year design lives, it is also imperative that prestressed elements—girders, piles, and deck panels—contain corrosion-resistant strands.

Figure 1. Corroded steel prestressing strand with section loss [1].

Several state DOTs, listed in Table 1, have recently used carbon fiber reinforced polymer (CFRP) tendons in prestressed bridge elements in an effort to reduce corrosion damage [3]. One of the most prominent examples of its use is the Bridge Street Bridge in Southfield, Michigan. A CFRP product called carbon fiber composite cable (CFCC) was used as both pre- and post-tensioning strand, and after 12 years of continuous monitoring it shows optimal performance and no signs of corrosion. Additionally, between 1987 and 1996 over two dozen bridges and marine structures were constructed using CFRP prestressing tendons in Japan, Canada, and Europe [4]; several more are in progress in the USA.

Table 1. Projects Using CFRP Prestressing Tendons in US Bridges.

DOT	Structure	Application
Maine	Island Ave. Bridge	Post-tensioning
Michigan	Bridge St. Bridge	Pre- and post-tensioning
Missouri	Southview Dr. Bridge	Pre-tensioning
Ohio	Route 79 Bridge	Post-tensioning
	Route 23 Bridge	Post-tensioning
	Route 49 Bridge	Pre-tensioning
Virginia	Nimmo Parkway Bridge	Pre-tensioning
	Route 49 Bridge	Pre-tensioning

Starting in 2012 and continuing to-date, VDOT has been pursuing CFRP as a corrosion-resistant alternative to steel prestressing materials for longer lasting concrete bridge structures in Virginia. In the Nimmo Parkway bridge (Virginia Beach, VA), there are 18 concrete piles prestressed with the seven-wire CFRP strand product CFCC, made in Japan (Tokyo Rope Mfg, Inc). Figure 2(a) shows the 15.2 mm CFCC strand used as longitudinal pre-tensioning tendons with a full spool in Figure 2(b), and the 5 mm CFCC wire used as transverse reinforcement is shown in Figure 2(c).

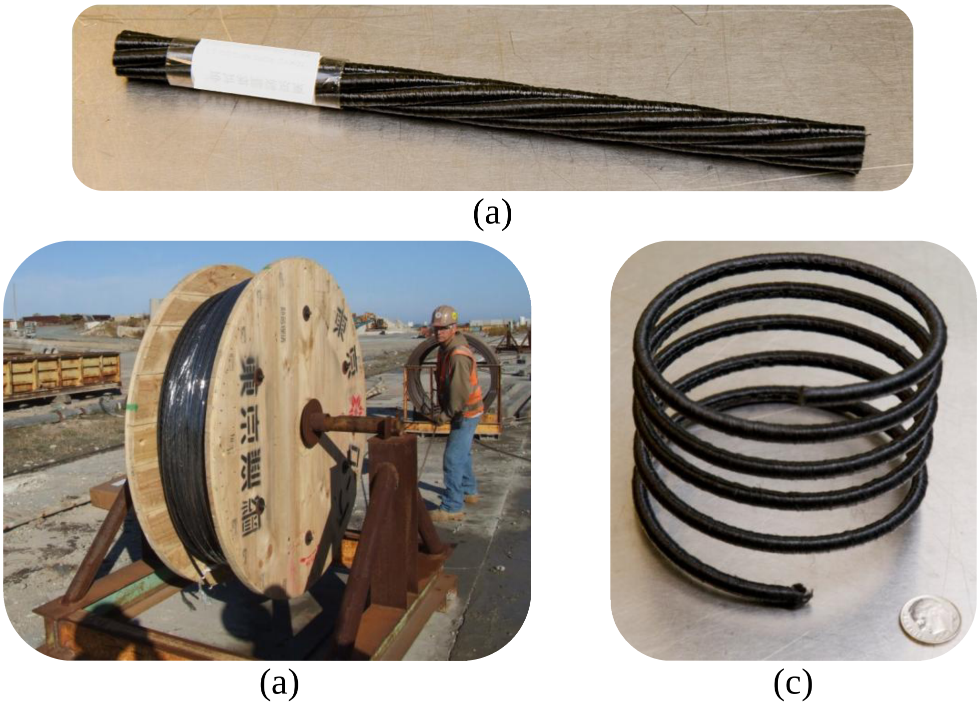

(a)

(a)

(c)

Figure 2. CFCC prestressing tendons: (a) 15.2 mm strand, (b) spool at the precast plant, (c) 5 mm CFCC wire for spiral ties.

The in-service performance of CFRP rods and cables can be hard to evaluate in certain structural applications, such as prestressed concrete bridges, where instrumentation is often limited and the material cannot be removed for inspection. Piles are primary examples of structural components that are subjected to moist, even aggressive or marine, environments and could last much longer if constructed using quality concrete and CFRP prestressing tendons. However, due to the documented effects of moisture and temperature on the mechanical properties of CFRP, it is important to understand how it behaves in concrete through realistic simulated environments [5]. While advances in this area of study have been made in the last decade, a great deal of information is missing from the literature in the area of environmental durability, particularly involving the effects of stress [5, 6, 7].

1.2 Motivation and Objectives

To implement CFRP in prestressed concrete bridge structures with more confidence, this project was initiated to study issues pertaining to environmental durability under in-service conditions. Specifically, the intention was to extract some information about fundamental material behavior while contributing directly to engineering applications in VDOT and beyond. That being said, the primary objectives of this study are as follows:

1. Investigate the effects of temperature, alkaline and alkaline/chloride solutions, and temporary stress on material properties over time, in the context of reinforced and prestressed concrete structures;
2. Determine whether a meaningful relationship exists between various observations, including moisture content, glass transition temperature, interlaminar/intralaminar shear strength, and tensile properties;
3. Establish a clear testing methodology for evaluating durability of CFRP for prestressing applications that can be adopted by VDOT and other laboratories, either by creating new guidelines or modifying existing standards.

1.3 Thesis Structure

- **Chapter 2** presents a comprehensive literature review regarding the previous research conducted on environmental durability of CFRP, both from civil engineering and other fields—aerospace, oil/pipeline, and wind energy industries have studied similar issues with similar CFRP materials. Both experimental data and modeling approaches are discussed.
- **Chapter 3** gives the experimental approach with description of the material under investigation and the testing methods applied.
- **Chapter 4** provides the experimental results , with an in-depth analysis based largely on the work mentioned in Chapter 2. Two modeling approaches are presented and compared to the experimental data—one from the literature, the other developed in this study.
- **Chapter 5** lists conclusions and other significant implications from the results and analysis, with a primary focus on durability behavior and durability testing methodologies for CFRP in prestressed concrete bridge applications.
- **Chapter 6** contains recommendations for future work in this area.
- Finally, a complete list of references is given, in the order they appear in the text. Appendices A and B include additional results from the experimental and modeling efforts of this study, that were repetitive to include in the main body of the thesis.

CHAPTER 2: LITERATURE REVIEW

2.1 Fiber Reinforced Polymer (FRP) Composites

Fiber reinforced polymer (FRP) composites have become more popular as a corrosion-resistant, light-weight alternative to steel and aluminum, typically with better mechanical performance than timber. These materials are multiphase systems that are designed to bear physical loads in structures, consisting of a reinforcing phase (fibers) and a matrix phase (polymer) that are bound together through chemical adhesion (interface). The primary load-carrying mechanism existing in FRP is the transfer of axial fiber stresses to nearby fibers through shear stresses in the matrix [8]. Since the fibers are typically much stronger than the matrix, they are responsible for carrying the majority of axial, torsional, and flexural stresses whereas the matrix is much weaker and serves to bind fibers together—thus the term, “composite action.”

Despite the advantages in mechanical performance, FRP composites can be susceptible to degradation when subjected to certain environmental and loading conditions. This is because the polymer matrix tends to be a material that is sensitive to moisture, heat, stress, and chemicals. This section provides an overview of CFRP constituents and structure, since it is the type used in this study and is the most common for concrete bridge structures [4].

2.1.1 Carbon Fibers

There are two primary precursor materials used to manufacture carbon fibers, polyacrylonitrile (PAN) and pitch, with rayon comprising a very small third precursor type [9]. The five largest carbon fiber manufacturers in the world (in order) are Toray Industries (Japan), TohoTenax–Tejin (Japan), Mitsubishi Rayon (Japan), Zoltek (USA), and Hexcel (USA) [10]. Carbon fibers consist of graphene sheets in hexagonal arrangements, which are stacked in parallel planes and weakly bonded through van der Waals forces [9, 11]. A schematic of this arrangement, forming regions called *crystallites*, is shown in Figure 3(a). The crystallites then pack together in various arrangements to form a carbon fiber, which are typically 7 μm in diameter; the most common cross-section morphology types shown in Figure 3(b).

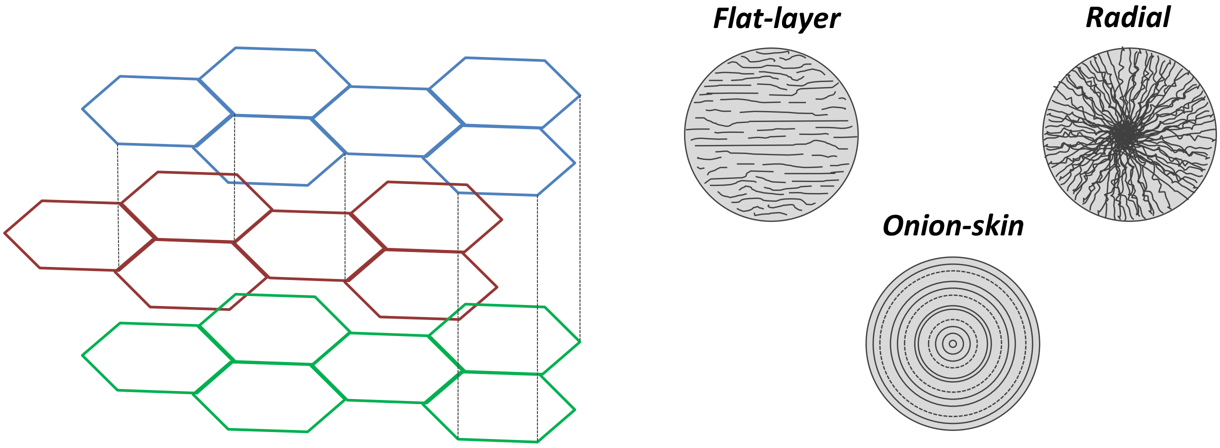

(a) (b)

Figure 3. Structure of carbon fibers: (a) schematic of graphene crystallites, and (b) common morphology of packed crystallites (inspired by [12]).

Aerospace grade carbon fiber is usually sold in bundles called *tows*, which contain a certain number of thousands of fibers: 3K, 6K, 12K, and 24K are the most common tow sizes. Industrial/commercial applications utilize larger tows, 24K or larger. Another difference between the aerospace and industrial/commercial grades is the elastic modulus, which are categorized as standard, intermediate, and high. The tensile properties for each category are given in Table 2. The key factors that separate these modulus groups are primarily microstructure, as well as carbon (graphene) content and diameter [11]. Finally, carbon fibers can be left untreated after production, or given some kind of treatment—chemical or thermal—or polymer coating (called *sizing*) to improve bonding with polymer matrices. Fiber-matrix bonding is further discussed in Section 2.1.3 and 2.6.2.

Table 2. Tensile and physical properties of PAN carbon fibers [11].

Property	**Industrial**	**Aerospace**		
	Standard	*Standard*	*Intermediate*	*High*
E_{tensile}, GPa (Msi)	228 (33)	220–241 (32–35)	290–297 (42–43)	345–448 (50–65)
σ_{tensile}, GPa (10^2 ksi)	3.8 (5.5)	3.45–4.83 (5.0–7.0)	3.45–6.20 (6.0–9.0)	3.45–5.52 (6.0–8.0)
$\varepsilon_{\text{failure}}$ (%)	1.6	1.5–2.2	1.3–2.0	0.7–1.0
Carbon Content (%)	95	95	95	≥ 99
Fiber Diameter, µm	6–8	6–8	5–6	5–8
Specific Gravity	1.8	1.8	1.8	1.9

2.1.2 Thermosetting Polymer Matrices

Thermosets are oligomers—meaning, low molecular weight polymers—that densely crosslink via reactive functional groups, forming a three-dimensional polymer network structure [13]. The term *crosslinking* refers to the connection between separate molecular chains by way of covalent bonding. Whereas a very ordered material (i.e., crystalline) packs a high number of molecules into a finite volume, the amorphous structure of crosslinked thermosets yields a certain amount of unoccupied volume between chains, called *free volume*. Figure 4 depicts the general nature of this morphology. The primary types of thermosetting polymers are: epoxy, phenolic, polyester, vinylester, urea, polyurethane, polyimide, bismaleimide, and furan [13]. All of these have fairly similar structures, compared to other polymers, but differ in precursor material and functional groups. This yields a variety of physical, mechanical, thermal, and sorption properties. Since epoxy is the most common thermoset used in CFRP, and is in fact the matrix in the material studied in this thesis (CFCC), it is given priority here. Vinylester resins are also common, and similar to epoxy, so they are cursorily described as well.

A standard epoxy resin is produced by reacting a phenol—like bisphenol A (BPA)—with a compound called an epoxide—usually epichlorohydrin (ECH), which is derived from the reaction between polypropylene, chlorine, and sodium hydroxide; a crosslinking curing agent such as amine is often included [13, 14]. The chemical structure of a standard BPA-derived epoxy is given in Figure 5. Various compounds can be added to the epoxy to change certain properties, such as flow viscosity or working time (uncured), or toughness (cured) and adhesion.

Vinylester resins are created through a reaction between epoxy and unsaturated carboxylic acid (such as acrylic or methacrylic acid), usually with a catalyst at elevated temperatures, which creates ester groups along the epoxy chains [13, 15]. It is known for sharing mechanical properties with epoxy and exhibiting processing properties similar to polyester. Typical mechanical properties for epoxy and vinylester are listed in Table 3.

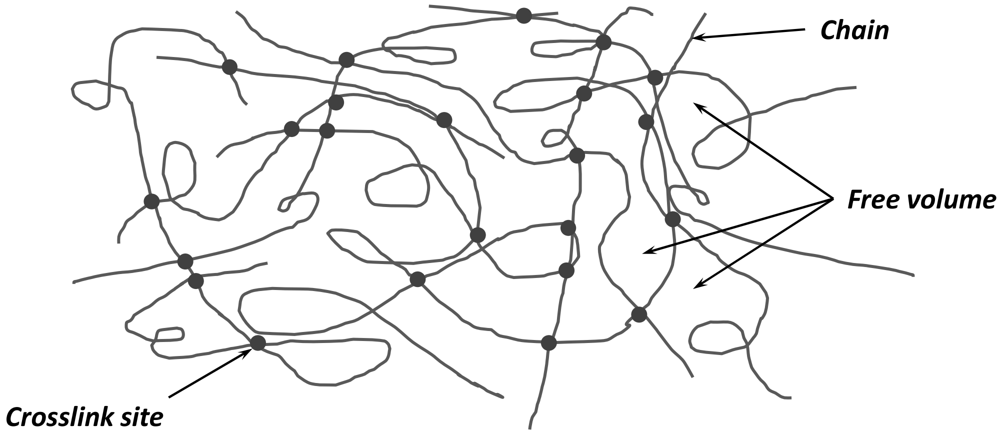

Figure 4. Diagram of an amorphous crosslinked thermoset (e.g., epoxy, vinylester).

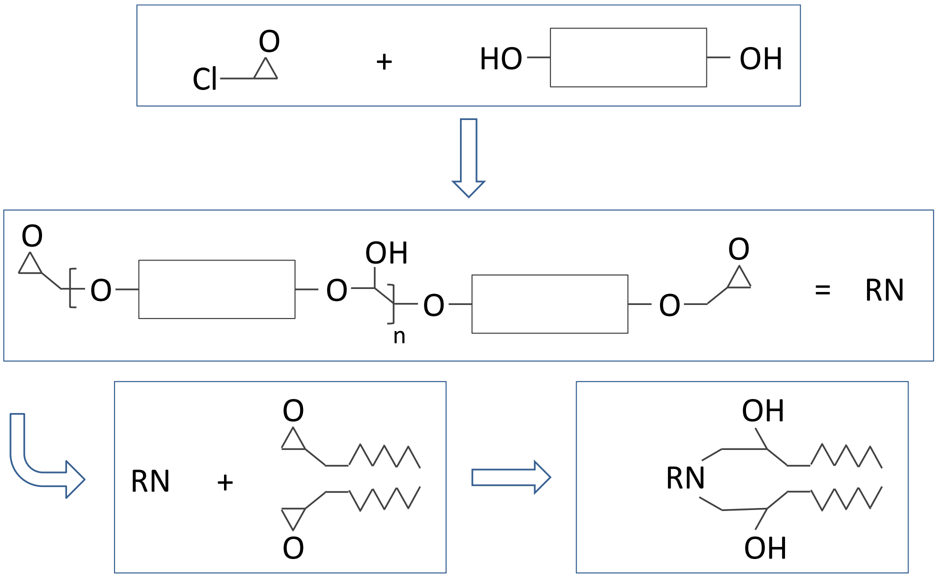

Figure 5. Chemical structure of standard epoxy thermosetting polymer (inspired by [14]).

Table 3. Mechanical properties of typical epoxy and vinylester thermosets [14, 16].

Property	**Epoxy**	**Vinylester**
E_{tensile}, GPa (ksi)	2.7–6.5 (392–943)	2.1–5.2 (327–876)
σ_{tensile}, MPa (ksi)	36–100 (5–15)	41–76 (6–11)
$\varepsilon_{\text{failure}}$ (%)	1.5–20	2–8
Specific Gravity	1.2	1.2

2.1.3 Interface and Interphase

Any system is only as strong as the weakest component. In concept, composite materials are comprised of two or more phases with distinct properties that act synergistically to provide desired (engineered) performance. In the case of FRP, this means the fibers must bond sufficiently to the polymer matrix so that (1) stresses are transferred to each fiber nearly uniformly, and (2) catastrophic failure—i.e., sudden and complete fracture—does not occur due to failure of select weaker fibers nearby stronger ones [17, 18, 19]. The interface is typically considered a zero-thickness shell in the field of composite mechanics, and simply represents both the partition and joint between material phases. However, those in the field of materials chemistry and processing consider the interface to be more complex, consisting of an *interphase* wherein the fiber and matrix blend chemically and thus has a mixture of their properties [18, 20]. The development of tailored interphases comes mainly from (polymeric) sizing and other low-molecular weight treatments on the fiber surfaces [13, 20]. Figure 6 is a simple diagram illustrating this concept.

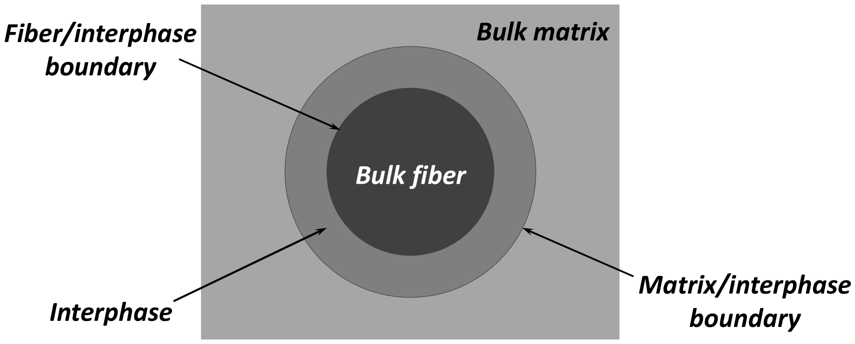

Figure 6. Concept of interphase (mixed-phases) at the fiber/matrix interface (not to scale).

2.1.4 FRP Pultrusion Process

Several methods have been developed for manufacturing FRP composites, such as hand lay-up, vacuum-assisted resin transfer molding (VARTM), compression molding, filament winding, and pultrusion. The value of each method depends on the shape, size, and constituents of the intended sections. Since the CFRP rods/bars and cables used in prestressed and reinforced concrete are linear profiles with symmetrical cross-sections, pultrusion is the most efficient manufacturing process and thus will be briefly described. The term *pultrusion* is a colloquial combination of “pull” and “extrusion” and reflects its inspiration in metals processing. As seen in Figure 7, this process is all in-line and generally does not require other equipment or stages beyond what is shown. First, the rovings of fibers (spools containing fiber tows of specified count) are fed through a guide plate into a resin bath. While impregnated with uncured resin, the bundle is then pulled through a die to give the composite the desired shape. Most pultrusion systems do not use temperature curing, since this can be difficult to regulate while the production process runs continuously. Finally, the FRP is cut to desired lengths at the end of the line.

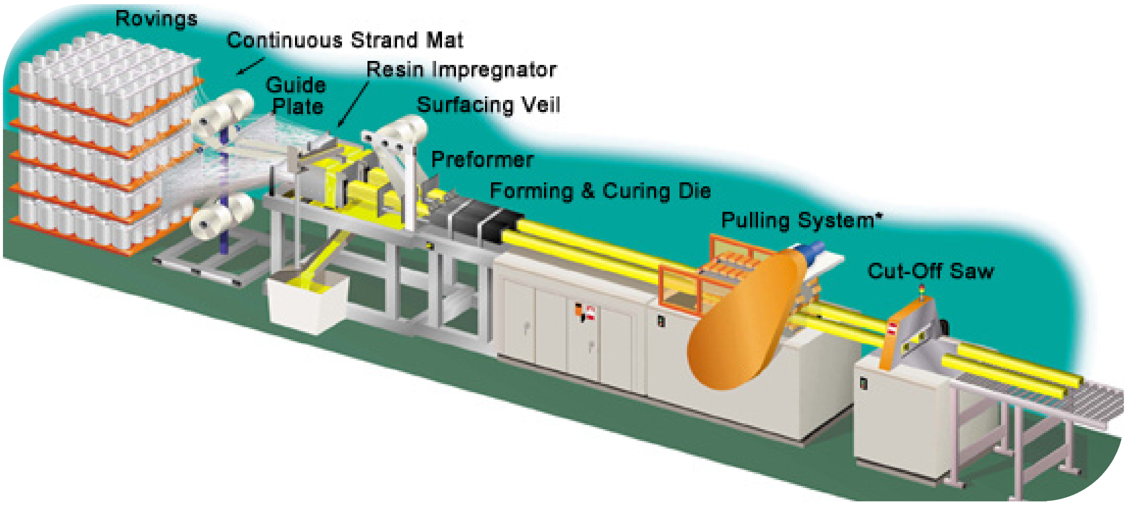

Figure 7. Diagram of the pultrusion manufacturing process for FRP composites [21] (Copyright 2015, Strongwell Corporation).

2.2 Overview of Durability Studies

In light of the information presented in Section 2.1, it is apparent that a multiphase material system like FRP is susceptible to various types of degradation that negatively affect mechanical performance; resistance to that degradation is referred to as durability. Considering the in-service conditions of CFRP composites used in prestressed concrete bridge applications, civil engineers are largely concerned with two types of durability:

- *Environmental* durability—resistance to material degradation caused by exposure to moisture, heat, reactants, or a combination;

- *Mechanical* durability—resistance to physical damage caused by sustained or cyclic stresses, impact, or other applied loading conditions.

This thesis is focused on the former, environmental durability, but some attention is given to the influence of mechanical stress (see Section 3.2.3). Mechanical durability is very important, and the durability under combined environmental and mechanical degradation is arguably the most important [5, 6], but this scope is limited to environmental degradation caused by temperature and alkaline solutions, given the time and resources available in this project. The following sections delve into the literature related to durability of FRP, with an emphasis on CFRP, considering environmental factors such as temperature, aqueous solutions, and applied mechanical stress. In many cases, pertinent research was conducted through aerospace, marine, and energy industries, but any relevant work regarding civil infrastructure was also reviewed.

2.3 Thermal Characteristics on FRP

2.3.1 Glass Transition in Amorphous Polymers

Unlike thermoplastics, which typically consist of 2D polymer chains arranged in a semi-crystalline structure, thermosets do not exhibit phase transitions such as melting. Instead, they comprise 3D cross-linked networks of chains existing in one of two states: glassy or rubbery. In the glassy state, thermosets are relatively rigid and strong. This changes gradually as the material reaches a particular temperature, known as the glass transition temperature T_g [13, 14, 22]. Above this value, the mechanical behavior of a thermosetting polymer can be described as very viscoelastic, like rubber—thus, the rubbery state. This effect on physical (specific volume) and mechanical (modulus) properties is illustrated in Figure 8.

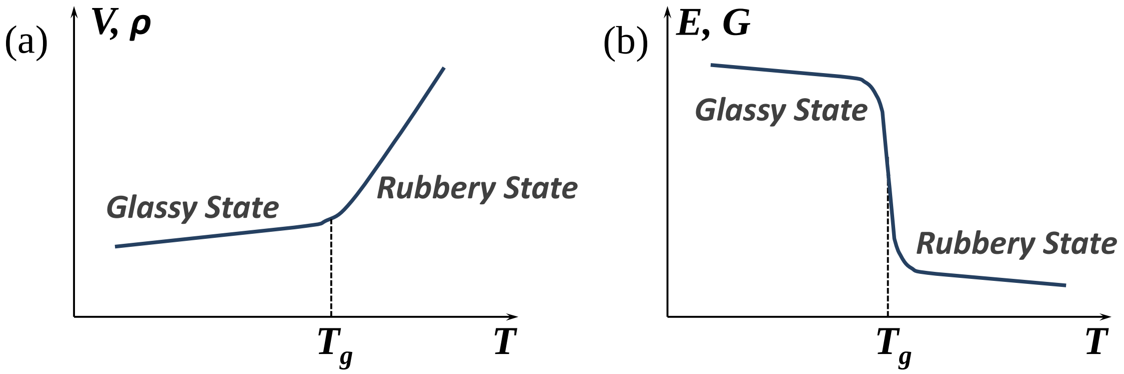

Figure 8. Relationship between (a) volume (density) and temperature, and (b) modulus and temperature in thermosetting polymers.

For a thermoset with a given chemical formula, T_g can be expressed in terms of heat capacity and degree of cure by the following expression [13]:

$$T_g = \frac{\alpha \Delta c_{p\infty} T_{g\infty} + (1-\alpha)\Delta c_{p0} T_{g0}}{\alpha \Delta c_{p\infty} + (1-\alpha)\Delta c_{p0}} \tag{1}$$

where α is degree of cure, T_{g0} is the value of T_g before cure, $T_{g\infty}$ is the value of T_g at maximum α, Δc_{p0} is the change in heat capacity corresponding to T_{g0}, and $\Delta c_{p\infty}$ is the change in heat capacity corresponding to $T_{g\infty}$ [13]. By using the relationship between heat capacity and glass transition proposed by Montserrat [22], Eq (1) can be reduced to the following:

$$\frac{1}{T_g} = \frac{(1-\alpha)}{T_{g0}} + \frac{\alpha}{T_{g\infty}} \tag{2}$$

However, sometimes it can be difficult to measure T_{g0} and $T_{g\infty}$ accurately due to the evolution of curing as the measurements are made, which can give erroneous predictions of T_g

based on degree of cure. This approach was not used in this thesis, but it is helpful to understand how T_g relates to α based on the physical structure (crosslinking) of the polymer.

2.3.2 Physical (Thermal) Aging

The condition of a thermoset's crosslink network changes over time, with the clock starting at the initial curing stage. It has been shown that subjecting FRP composites to a temperature below T_g for a certain period of time yields the network, and consequently mechanical behavior, of an older specimen. This is known as physical aging, and is reversible if the material is heated above T_g for at least 15 minutes; it differs from chemical aging, which is irreversible due to the occurrence of chemical reactions that alter a polymer's composition [23, 24, 25]. Since physical aging occurs very slowly in a natural environment, elevated temperatures are used—sometimes in conjunction with moisture, called *hygrothermal* aging—to accelerate the process for evaluating and predicting material performance in a reasonable period of time. However, the aging parameters must be chosen carefully for each composite system to avoid convoluting the aging with multiple mechanisms that cannot be accounted for properly [25].

2.4 Moisture Effects on FRP

2.4.1 Low-Molecular-Weight Mass Transport

In this thesis, the term *sorption* will be used when discussing the penetration of moisture (and aqueous solutions) into the polymer composite; *absorption* typically refers to the interstitial diffusion of water molecules through a material, *adsorption* is the adhesion of water molecules to a material, and *wicking* (capillary flow) is the channel-like flow of moisture through cracks, large voids, and other open areas in the material structure. The transport of aqueous solutions into FRP sometimes involves one of these processes, and sometimes all of them.

Work by Chin et al. [26, 27], Scott and Lees [28, 29], and Micelli and Nanni [30] confirmed that in the case of undamaged thermosetting resin, moisture sorption is typically governed by Fickian diffusion. However, after a certain degree of absorption is reached and the fluid has penetrated the composite sufficiently, damage occurs from swelling strains and the diffusion behavior changes from linear to anomalous [30]. Fick's second law in one dimension, taken to be the through-thickness direction for most FRP specimens, is expressed as [31]:

$$\frac{\partial C}{\partial t} = D(t)\frac{\partial^2 C}{\partial x^2} \tag{3}$$

where C is the concentration of the penetrant, t is time, x is the linear position in one dimension, and D is the diffusion coefficient, sometimes called the diffusivity. Note that the diffusivity can be constant or time-dependent, in which case $D(t)$ has been represented by a Prony series [32]:

$$D(t) = D' + \sum_{r=1}^{R} D_r\left(1 - e^{-t/\tau_r}\right) \tag{4}$$

where D' and D_r are temperature-dependent Prony coefficients, and τ_r is a corresponding retardation time. The relationship between D and temperature T can often be easily modeled with the Arrhenius equation, if enough experimental data is available for different temperatures [33]:

$$D = D_0 \exp\left(-\frac{E_a}{RT}\right) \tag{5}$$

where D_0 is the diffusivity when $1/T = 0$, R is the universal gas constant, and E_a is the activation energy. Activation energy is usually unique to a given process or mechanism, so it must be calculated from a controlled set of experiments for the desired process.

When considering moisture diffusion in terms of instantaneous moisture content as a weight percentage of the specimen, Eq (3) is written as the following [34]:

$$M(t) = M_\infty \left(1 - \sum_{n=0}^{\infty} \frac{8}{(2n+1)^2 \pi^2} \exp\left[\frac{-D(2n+1)^2 \pi^2 t}{4h^2} \right] \right) \tag{6}$$

with an equilibrium (saturated) moisture content M_∞ and a material thickness h. The temperature dependence of M_∞ is given by van't Hoff's equation, which looks similar to Eq (5) [33]:

$$M_\infty(T) = M_0 \exp\left(-\frac{\Delta H_{abs}}{RT} \right) \tag{7}$$

where M_0 is a temperature-independent constant and ΔH_{abs} is the heat of absorption, which is the heat per mole of water in the polymer. Studies have found that moisture sorption by diffusion in many amorphous polymers can be closely described by a two-stage model that simultaneously accounts for concentration-based diffusion and molecular relaxation [33, 35, 36, 37]:

$$M(t) = M_\infty \left(1 + k\sqrt{t} \right) \left(1 - \exp\left[-7.3 \left(\frac{Dt}{h^2} \right)^{0.75} \right] \right) \tag{8}$$

where k is a parameter that represents molecular relaxation in the polymer, and is obtained through curve-fitting. In many cases for epoxy, the values of D, k, and M_∞ depend on free volume and chemical potential in the polymer, which means they will be significantly influenced from both temperature and stress state [33, 37, 38, 39, 40, 41, 42, 43].

Conversely, another common moisture sorption model used in place of Fick's laws is the Langmuir diffusion model. Rather than treat moisture sorption as a concentration-based and relaxation-based process involving an unbound fluid, Langmuir moisture transport proposes that two phases exist in the penetrating media (such as water): a mobile (free) phase with molecular concentration n, and a bound phase with molecular concentration N [44]. This model assumes that water molecules enter the polymer as a mobile phase and can diffuse in a Fickian manner, but at any point in time and in spatial position they can become bound to the epoxy molecules due to dipole interactions [45]. The probability that mobile water molecules will become bound is defined as γ, and the probability that these bound molecules become mobile again is β. These quantities are related at equilibrium through the following expression:

$$\gamma n_\infty = \beta N_\infty \tag{9}$$

and the diffusivity is related to these probabilities through the partial differential equations:

$$D\frac{\partial^2 n}{\partial x^2} = \frac{\partial n}{\partial t} + \frac{\partial N}{\partial t} \tag{10}$$

$$\frac{\partial N}{\partial t} = \gamma n - \beta N. \tag{11}$$

The formulation for relative moisture content is given in Eq (12), and approximations are given in Eq (13) and Eq (14) for the cases of short exposure times ($t/\kappa < 0.7$) and longer exposure times ($t/\kappa >> 1.0$), respectively:

$$M(t) = M_\infty \left\{ \begin{aligned} &\left(\frac{\beta}{\gamma+\beta}\right) e^{-\gamma t} \left(1 - \sum_{p=1}^{\infty} \frac{8e^{-\kappa p^2 t}}{p^2 \pi^2}\right) \\ &+ \left(\frac{\beta}{\gamma+\beta}\right)\left(e^{-\beta t} - e^{-\gamma t}\right) + \left(1 - e^{-\beta t}\right) \end{aligned} \right\} \tag{12}$$

$$M(t) = M_\infty \left\{ \frac{4}{\pi^{3/2}} \left(\frac{\beta}{\gamma+\beta}\right) \sqrt{\kappa t} \right\} \tag{13}$$

$$M(t) = M_\infty \left\{ 1 - \left(\frac{\gamma}{\gamma+\beta}\right) e^{-\beta t} \right\} \tag{14}$$

where $\kappa = D\,\pi^2/h^2$ and it is assumed to be several orders of magnitude larger than γ and β. Figure 9 provides a comparison between linear diffusion (Fickian) and two-stage diffusion/relaxation sorption curves, as well as an example of mass-change indicative of material degradation, for a typical epoxy.

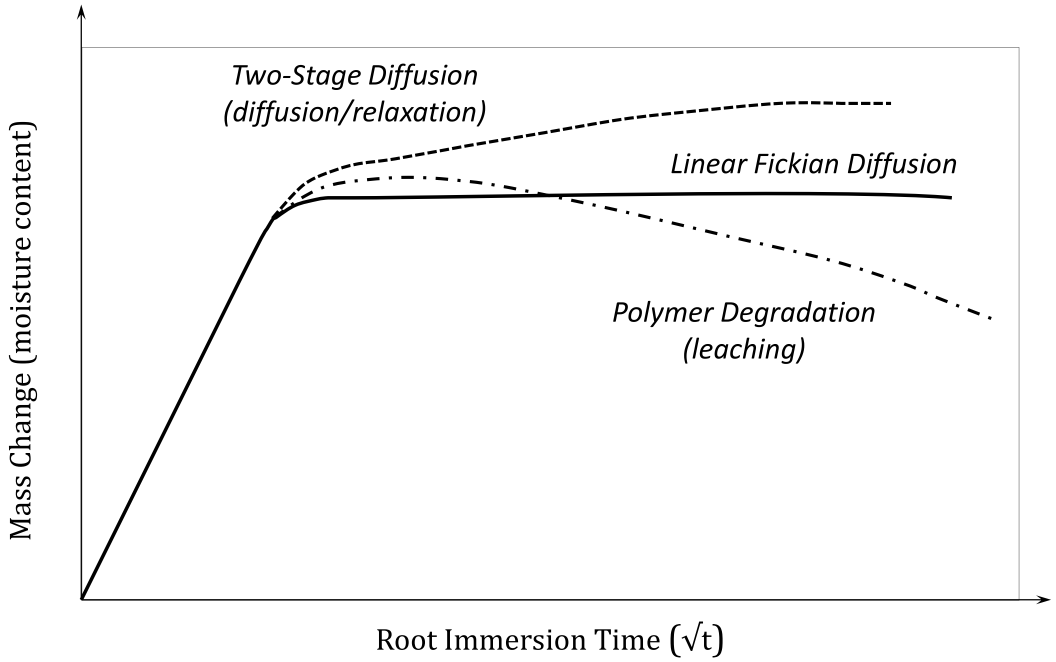

Figure 9. Moisture sorption curves corresponding to linear and two-stage models, showing the implications of accounting for moisture-epoxy interaction [46].

By treating an epoxy matrix as an assembly of packed thick spherical shells of different radii, Fahmy and Hurt [46] proposed the following equation to relate change in free volume to applied (external) stress:

$$f_\sigma = f_0\left(1 + \frac{\sigma(1+\nu)}{2E}\right) = f_0\left(1 + \frac{\sigma}{4G}\right) \tag{15}$$

where f_0 and f_σ are the initial and stressed free volumes, respectively, σ is the applied stress, ν is the Poisson's ratio, *E* is the Young's modulus, and *G* is the shear modulus. This is demonstrated experimentally in Figure 10, which shows the relationship between equilibrium moisture content and percentage of ultimate tensile strength (UTS) for neat epoxy and CFRP laminate [41].

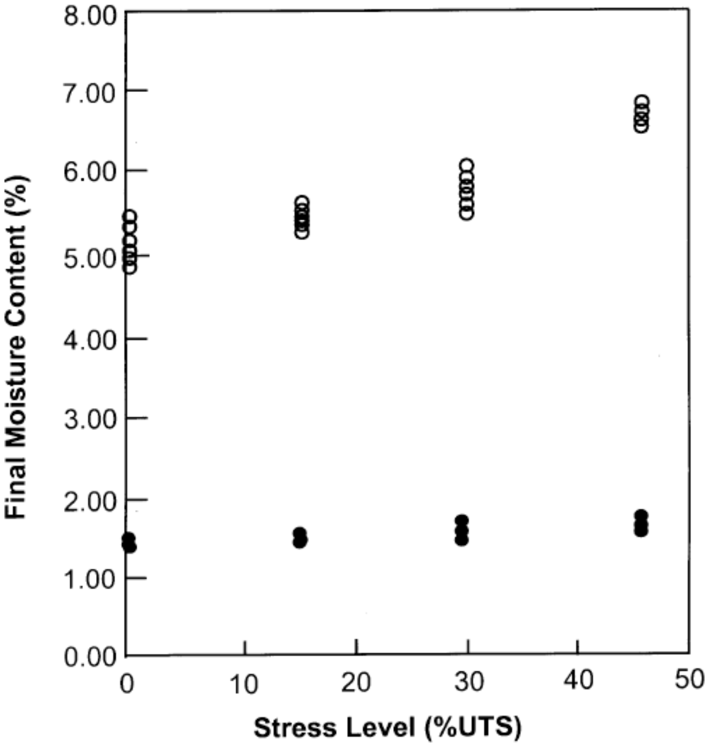

Figure 10. Influence of applied stress on the equilibrium moisture content of (○) neat epoxy and (•) unidirectional CFRP laminate [41] (with permission from Springer).

2.4.2 Matrix Plasticization and Swelling

Sorbed moisture in FRP tends to alter the polymer network of the matrix, leading to a decrease in T_g through a change in the energy needed to deform the material [36, 37, 44, 47]. This softening is called *plasticization* and is associated with both thermoset and thermoplastic polymers, and is caused by polar interaction between water molecules and the polymer chain in such a way that free volume increases; plasticization is basically reversible as long as the polymer chain is not chemically altered [37]. The amount of plasticization that occurs for a given moisture content depends on the degree of interaction between the water and the matrix, which comes from hydrogen bonds (H-bonds) formed between bound water molecules and polymer chains [48]. Increasing polymer segmental chain mobility is a direct consequence of this water-polymer interaction. Microscopic examination has indicated that these matrices are susceptible to bond degradation at the fiber-matrix interface, due in some cases to chemical mechanisms (Section 2.5) but largely due to plasticization [47]. Considering that the specific volume of an epoxy matrix increases with moisture content, yet carbon fibers are much less permeable and thus experience little or no moisture-related expansion, it is evident that the additional effect of plasticization in the polymer can contribute to interfacial debonding without any significant mechanical or thermal stresses applied to the composite [28, 38, 41, 47, 48].

After enough moisture has penetrated the FRP, pressure can potentially build up inside the material, due to the essentially incompressible nature of most liquids. To alleviate this pressure, an FRP specimen can respond in two ways: swell in a preferential direction (depending on fiber orientation and architecture), or crack [41]. The answer to which is more likely to occur depends on the geometric parameters of the specimen in question—aspect ratio, edges and angles of corners, and fiber orientation relative to specimen geometry [28].

Figure 11 illustrates all the moisture effects discussed in Section 2.4, except for chemical reaction effects and material degradation. While for some FRP, any of these processes alone could be a detriment to physical and mechanical properties, they often occur in combination and thus even high-performance epoxy resins and CFRP composites are susceptible to changes.

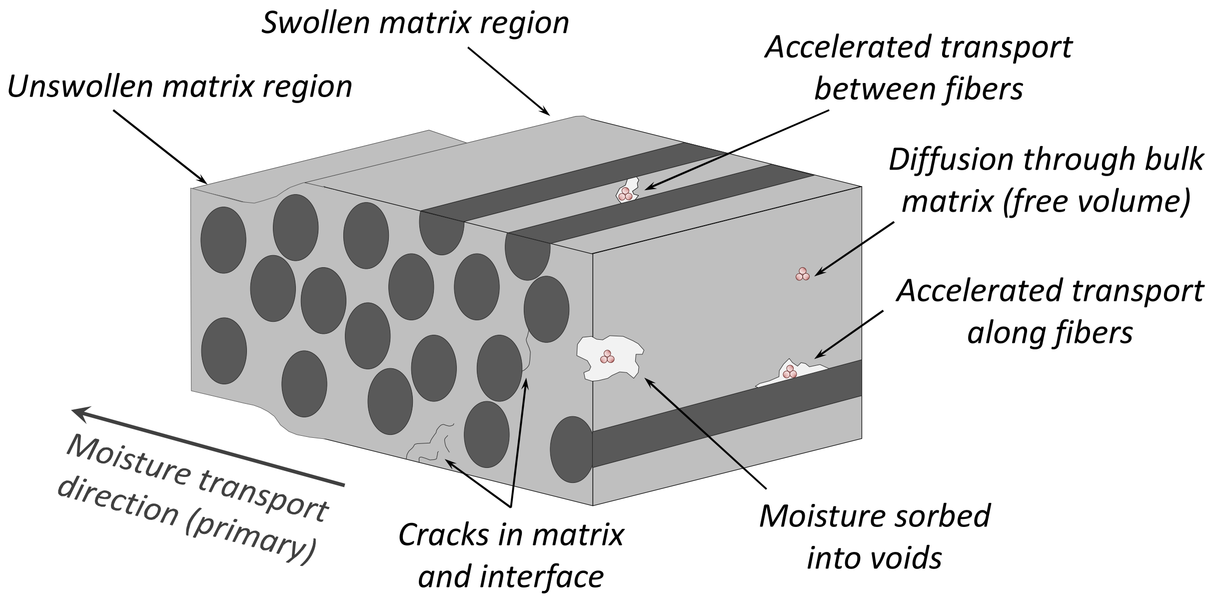

Figure 11. Schematic of all moisture-related effects on physical and mechanical properties of FRP composites, except for chemical attack (inspired by [42]).

2.5 Chemical Effects on FRP

2.5.1 Hydrolysis in Polymers

When the bonds holding organic molecules together are sufficiently weak or the temperature and pressure conditions are sufficient, water can react with them to form other compounds. This reaction process, called *hydrolysis*, takes place at reactive groups in polymer chains such as anhydride, ester, or amine groups [49, 50]. This occasionally takes place in thermosetting polymers, wherein molecules contributing to the structural integrity and mechanical properties of the material are separated via chain scission. Typically, the new compounds are not corrosive to the polymer, but they can possess a smaller density which leads to swelling strains and potential crack initiation sites [41]. Hydrolysis is most common among polyester and vinylester resins, but it is rarely an issue for ester-free epoxy.

2.5.2 Acidic and Alkaline (pH) Effects

Typically, carbon fibers are fairly stable chemically, and are even sometimes recycled from old composites using acidic solutions [51]. However, some thermosetting polymer matrices are susceptible to degradation through chemical reactions in acidic or basic solutions, despite higher resistance from polymers like epoxy. Sulfuric acid was found to decrease the flexural strength of amine-cured epoxy as much as 60% after just 15 days of exposure, and solution uptake was much greater than for pure water [52]. As the acid started degrading the epoxy through chemical reactions along the chains, the polymer morphology changed as damage increased, allowing further penetration, creating a cyclic process. When exposed to alkaline solutions, epoxy was found to exhibit a noticeable amount of degradation compared to pure water [26, 27, 44]. Exact details of the chemical interaction between alkaline solutions and epoxy resins are still not fully known, but empirical data indicate the effect is greater than pure water.

2.6 Mechanical Effects on FRP

Damage and morphological changes caused by mechanical loading can accelerate or exacerbate the other degradation mechanisms reviewed in Sections 2.3-2.5, so a brief survey of mechanical deformation and damage in FRP composites is given here. This section focuses on physical mechanisms and observations rather than mathematical aspects of damage.

2.6.1 Matrix Cracking

Matrix microcracking has often been observed as the first damage process in response to mechanical loading, thermal cycling or shock, and swelling stresses [53]. While the shear-yielding and tensile-failure natures of microcracking have been documented, the mathematical description and prediction of this process is still a work in progress, and numerous stress- or strain-based criteria exist [53, 54, 55, 56]. In any case, matrix microcracking is the first type of damage to occur in FRP from mechanical loading, unless the interfacial bond strength is deficient. Since microcracks allow moisture to transport via capillary flow more easily than bulk diffusion, aqueous solutions can penetrate the material to a greater degree (Section 2.4.1). This is important to consider in the case of FRP composites that carry high levels of stress, whether temporary or sustained, such as reinforcing or prestressing materials for concrete structures.

2.6.2 Interfacial Debonding

In a two-phase composite like FRP, three components can contribute to failure: the fibers, the matrix, and the interface. The relative ratios of strength and fracture toughness for each component dictate the failure progression in FRP, which is shown in Figure 12. Interface-dominated failure—indicated by the cleanly exposed fiber surfaces—is compared in Figure 13 to matrix-dominated failure wherein fragments of matrix are still adhered to the fibers.

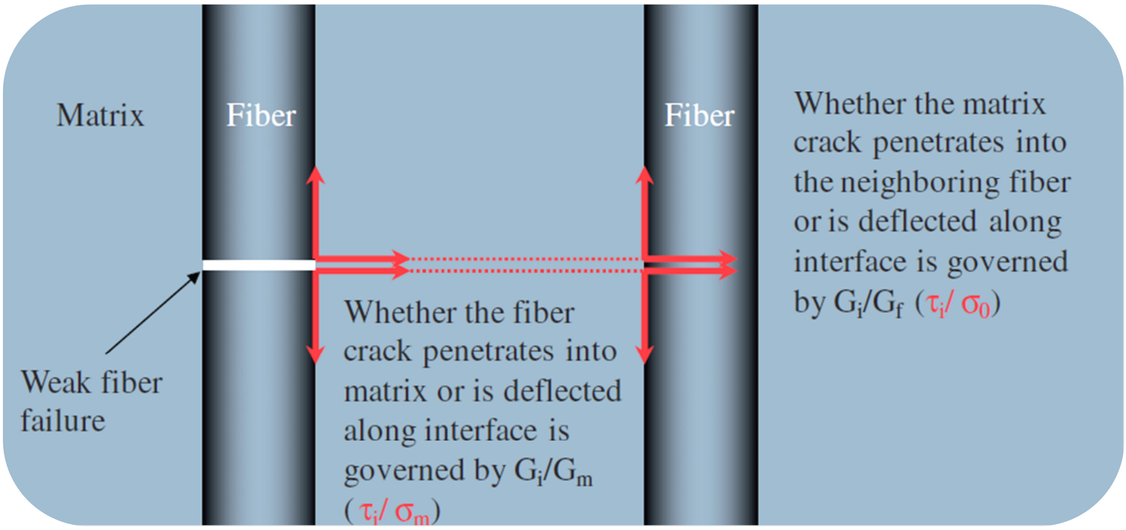

Figure 12. Process of failure progression in FRP considering the relative properties of fiber, matrix, and interface components [57] (with permission from Sage).

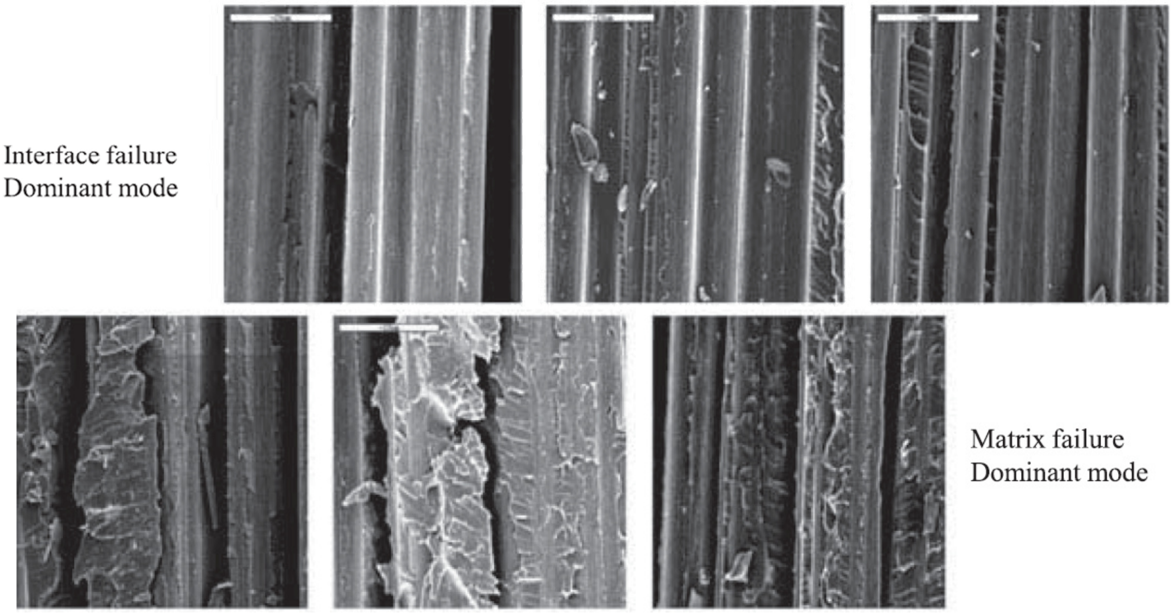

Figure 13. Comparison of interface-dominated vs. matrix-dominated failure in CFRP [58] (with permission from Elsevier).

Normal stresses (perpendicular to the fibers) contribute to the stress state at the interface during mechanical loading of the composite; however, in the case of unidirectional FRP without very thick dimensions, shear stresses are the dominant mechanism is causing debonding and pullout [17, 19]. As the bulk fibers and matrix become affected by the environmental conditions, the fiber-matrix interface is likewise affected. Thus, debonding can be observed as a common failure mode whether the FRP is tested in shear, flexure, or tension, regardless of the tensile strength of the composite or strengths of the constituents.

2.7 Durability Testing Methodologies for FRP Composites

2.7.1 Exposure Conditions and Accelerated Aging

Typical environments used in durability studies include moisture, heat, and sometimes cycles of both [6, 30]. In addition to pure water, alkaline solutions are often used to represent a moist concrete environment, consisting of one or more from KOH, NaOH, and $Ca(OH)_2$ depending on the pH desired, and salts like NaCl or $CaCl_2$ are used for marine environments [26, 27, 59]. Elevated temperature is the most common way to accelerate degradation [33, 59, 60].

2.7.2 Hygroscopic Testing Methods

Mass gain is a gravimetric method useful for approximating moisture sorption over time, since the relative increase in moisture content can be determined from the percentage change in specimen mass over time. Moisture concentration is calculated using Eq (16):

$$M(t) = \left(\frac{W_t - W_i}{W_i}\right) 100 \tag{16}$$

where $M(t)$ is the instantaneous moisture content (%), and W_t and W_i are the instantaneous and initial (dry) weights, respectively. When swelling is of interest, calipers can be used to measure changes in diameter to calculate swelling strains:

$$\varepsilon(M) = \left(\frac{d_t - d_i}{d_i}\right)100 \tag{17}$$

where $\varepsilon(M)$ is the instantaneous swelling strain (%) as a function of moisture content, and d_t and d_i are the instantaneous and initial (dry) diameters, respectively.

2.7.3 Evaluation of Residual Mechanical Properties

Since environmental degradation leads to a loss in mechanical properties, durability testing is intended to understand the impact of in-service environmental conditions on the pertinent properties of interest. By the same token, certain mechanical properties may be more sensitive to environmental degradation than others, making them strong indicators of certain degradation mechanisms and their corresponding rates. The most common mechanical properties tested for evaluating durability in unidirectional FRP after environmental exposure are tensile strength and modulus, transverse shear strength, interlaminar/intralaminar shear strength (ILSS), and flexural strength [23, 25, 27, 59, 60]. For unidirectional FRP bars, standard ASTM test methods have been developed for these through D7502, D7617, D4475, and D7264, respectively [61, 62, 63, 64]. Axial compression is a complex failure mode for FRP [65], so unless it is a specific property under investigation, it is not ideal for evaluating durability.

In general, there are tensile, flexural, and compressive testing configurations for measuring ILSS, but flexural methods like the short-beam shear (SBS) test used in ASTM D4475 is the most simple and viable configuration for round FRP bars; the other methods are more suitable for laminates or thick prisms. Section 2.7.4 discusses the basic mechanics associated with the SBS test used for measuring ILSS.

In the realm of fracture mechanics, the Charpy impact (CI) test has been an industry standard for qualitatively measuring material toughness in metals and composites as a quality control/assurance procedure, but is less useful for quantitative analysis or design applications [66]. However, the CI test can still be used for evaluating durability of FRP by measuring residual CI strength (CIS) after environmental exposures. The mechanics of CI testing are discussed in Section 2.7.5, using the CFCC in this study as an example.

2.7.4 Mechanics of Short-Beam Shear (SBS) Testing

Flexural loading of beams with very small span-to-depth (*L*/*d*) ratios causes high shearing forces and relatively lower bending moments, so the composite is not in a state of pure shear. However, if the loading configuration and span length is selected appropriately, failure will be dominated by shear and the apparent ILSS can be measured [67]. With four-point loading, a constant-moment region exists between the loading points and shear is maximum between the supports and the loading points; on the other hand, three-point loading produces a maximum moment at midspan loading point and maximum shear everywhere except the loading point. This is illustrated in Figure 14—moments (M) and shears (V) not to scale relative to each other.

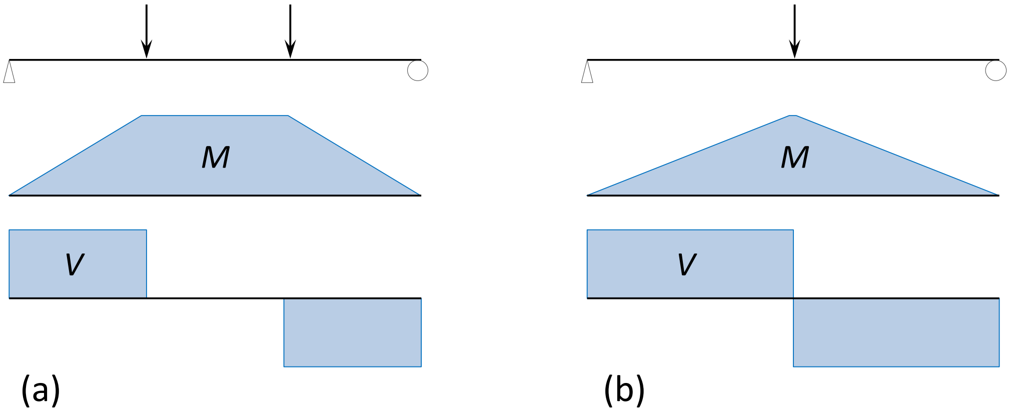

Figure 14. Moment and shear diagrams from SBS testing for (a) four-point bending, and (b) three-point bending.

As prescribed by ASTM D4475, the loading pin used in the three-point bending SBS test must be grooved so that it saddles the specimen, with a radius similar to the specimen radius [63]. Also, the standard specifies $3 \leq L/d \leq 6$ to ensure shear failure occurs, and $L/d = 3.8$ was considered for this example since it was used in the experimental study. This means the loading pin covers approximately 25% of the span, which constitutes a partially distributed load rather than a concentrated load; thus, under the loading pin, the moment is nonlinear and the shear varies linearly. This provision for a small distributed load also reduces concentrated bearing stresses at the loading pin [63, 68].

Shear stresses and deformations can be calculated from Timoshenko beam theory:

$$\int \left(\left(\frac{\tau}{G} \right) dx \, \tau \right) dA = \left(\frac{\tau_v}{G} \right) dx \, V \tag{18}$$

$$\tau_v = \frac{V}{A_v} = \frac{V}{\beta A} = \frac{V}{I^2} \int \left(\frac{Q}{t} \right)^2 dA \tag{19}$$

where τ_v (or τ_{rz} in cylindrical coordinates) is the shear stress, V is the shear force, G is the shear modulus, t is the width of the beam at the point of interest, Q is the static moment of area, I is the moment of inertia, and dA is the incremental area over the cross-section. A comparison is made in Figure 15 between axial tensile/compressive stresses and in-plane shear stresses for a CFRP beam having elastic modulus E = 148 GPa, L = 19 mm, d = 5 mm, and loaded with P = 1.05 kN.

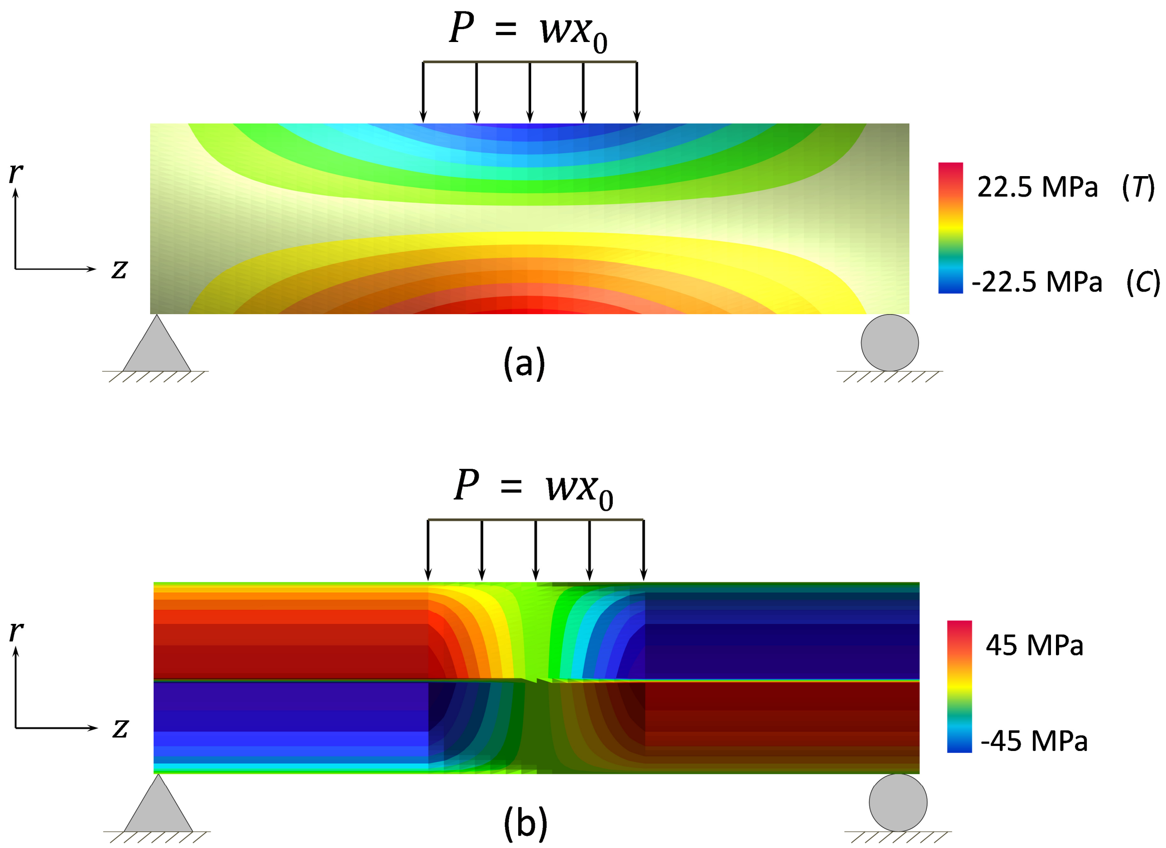

Figure 15. Stress distribution in CFRP rod under 3-point flexural loading during SBS testing, showing (a) axial stress (σ_{zz}), and (b) in-plane shear stress (τ_{rz} or ILSS).

For this example, it is clear that for a composite with fibers that are much stronger than the matrix or interface, interlaminar/intralaminar shear failure will dominate. Using an assumed axial tensile strength of 2500 MPa for CFRP, the calculated tensile stresses from beam theory only amount to 0.9% UTS of the composite and would not remotely approach tensile failure.

This flexural test indirectly measures “apparent horizontal” shear strength, according to ASTM D4475 [63]—commonly referred to as interlaminar shear strength (ILSS). However, this is only true for laminated (layered) FRP composites, since pultruded FRP is typically formed monolithically during manufacture and has no true “laminated” structure. Occasionally, the technical literature refers to the ILSS of pultruded FRP in the sense of *interfacial* shear stress between fibers and matrix. Nonetheless, this thesis more accurately refers to SBS testing as the *intralaminar* shear stress test, assuming the entire pultruded shape can be treated as a single "laminate" and thus the apparent ILSS measured is either fiber-matrix interfacial shear stress, matrix shear stress, or a combination. Therefore, degradation of the matrix or interface can be detected with this test, regardless of whether the apparent ILSS is a true material property.

2.7.5 Mechanics of Charpy Impact (CI) Testing

The literature mostly contains results of CI testing for the purpose of measuring apparent impact properties for aerospace and automotive applications, considering the effects of constituent materials and manufacturing techniques, physical aging, environmental exposure, or other treatments [69, 70, 71, 72]. In these papers, the authors have noted that other test methods tend to be more useful for quantitatively studying impact and fracture behavior of FRP. However, from the standpoint of characterizing environmental degradation in FRP using residual mechanical properties, this dynamic flexural test can indicate degradation of the matrix and/or the fiber-matrix interface through energy-absorption behavior during dynamic loading [72].

The only existing ASTM standard test methods for CI testing were developed for metals, ceramics, or neat plastics; no existing method covers FRP composites, especially not round profiles. However, based on the literature that discusses specimen geometry for measuring CIS in FRP, a limit of $L/d > 8$ should be imposed to avoid excessive amounts of impact-crushing and shear failure, rather than flexural failure [71]. While stress analysis using fracture mechanics for CI testing of FRP is still being refined, a basic example is presented here using a simple near-tip elastic stress field solution derived from the Westergaard function for Mode I (notch) [73]:

$$\sigma_{zz} = \frac{\sigma_0\sqrt{a}}{\sqrt{2r_1}}\cos\left(\frac{1}{2\theta_1}\right)\left(1+\sin\left(\frac{1}{2\theta_1}\right)\sin\left(\frac{3}{2\theta_1}\right)\right) \tag{18}$$

$$\tau_{rz} = \frac{\sigma_0\sqrt{a}}{\sqrt{2r_1}}\sin\left(\frac{1}{2\theta_1}\right)\cos\left(\frac{1}{2\theta_1}\right)\cos\left(\frac{3}{2\theta_1}\right) \tag{19}$$

where σ_0 is the far-field axial stress (from beam theory), a is the notch length at the instant of impact, and r_1 and θ_1 are coordinates around the notch tip seen in Figure 16. A comparison between axial stresses and shear stresses is made again in Figure 17, this time for a notched CFRP bar used in CI testing with d = 5 mm, L = 55 mm, and a = 1 mm. Note that this example assumes a V-notch, but blunted notches and slot (flat) notches are very common in real specimens; the mathematics are just simplified in this case.

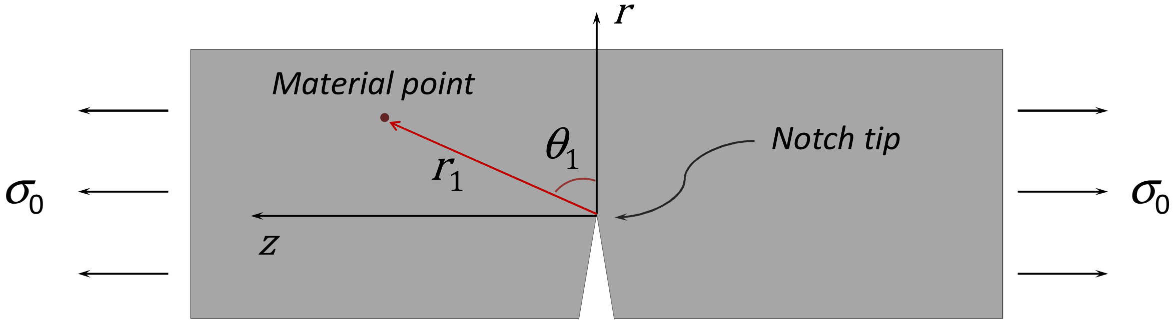

Figure 16. Diagram of notch geometry in Mode I fracture of CFRP bar (beam) during Charpy impact (CI) testing.

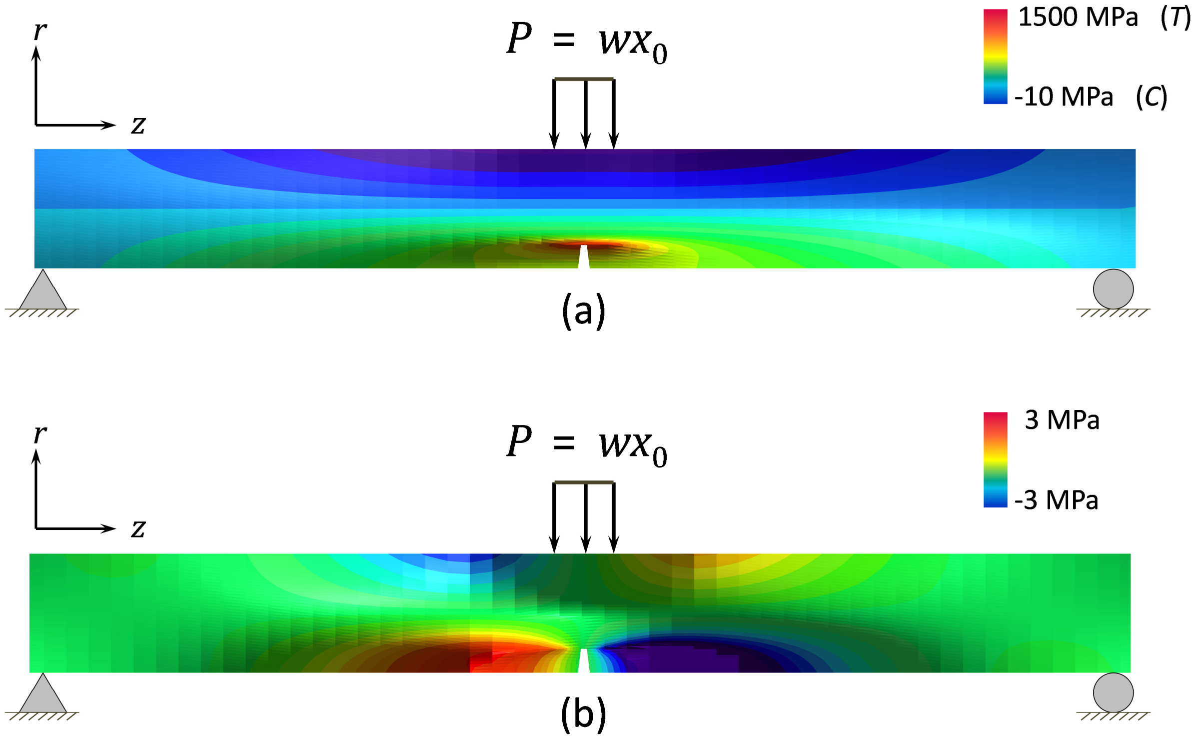

Figure 17. Stress distribution in notched CFRP rod under 3-point flexural loading during CI testing, showing (a) axial stress (σ_{zz}), and (b) in-plane shear stress (τ_{rz} or ILSS).

Unlike the stress distribution in Figure 15(a), which shows a relatively low tensile stress at the bottom-face of the specimen, very high stress concentrations are seen near the notch tip in Figure 17(a). By comparison, the largest shear stresses from CI testing in Figure 17(b) are much smaller than for SBS testing in Figure 15(b). This stark contrast means that specimens fail either by flexure (fiber fracture or pullout), or by shear (delamination). This is illustrated in Figure 18, where the striker impacts the specimen and the relative fiber, matrix, and interfacial strengths determine which failure mode occurs. This is consistent with observations in the literature [70].

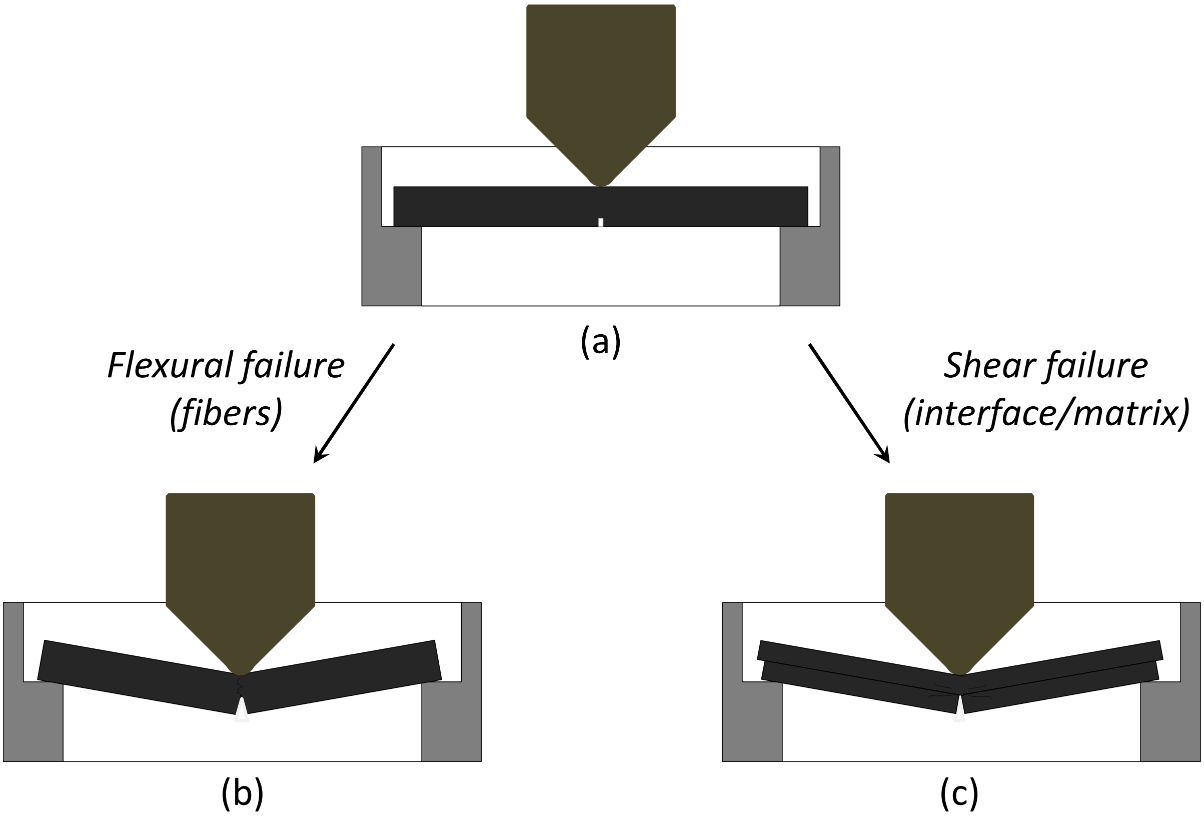

Figure 18. Schematic of the dynamic fracture process in CFRP during CI testing: (a) instant of striker impact, (b) flexural failure by fiber fracture or pullout, and (c) shear failure by delamination.

2.7.6 Analytical Techniques for Assessing Degradation in FRP

Two categories of analytical techniques are primarily used for durability testing with FRP composites: (1) thermal analysis, and (2) chemical analysis. Both destructive and nondestructive techniques exist within these categories, and the equipment and training necessary for performing these analyses can vary widely. A brief description of each is given below.

Thermal analysis techniques are used for measuring T_g and degree of cure, and can be performed with two main types of equipment: differential scanning calorimetry (DSC) and dynamic mechanical analyzer (DMA). While both techniques subject the specimen to a range of elevated temperatures, DSC simply compares the change in specimen temperature for a given input enthalpy compared to a reference cell, and is simpler to operate, whereas DMA applies mechanical load to the specimen and measures the change in modulus with temperature. Numerous studies have successfully applied DSC to durability testing as a way to detect degradation in FRP after environmental exposure [23, 33, 35, 74], while others have chosen DMA [26, 75].

Chemical analysis methods vary from x-ray and nuclear techniques, to infrared and chromatic techniques. The two most common types are Fourier transform infrared (FTIR) spectroscopy and energy dispersive spectroscopy (EDS), but some polymeric materials have been studied extensively with gel-permeation chromatography (GPC) as well. The chemical bonds in a polymer can be excited with infrared radiation, and FTIR identifies key signals from this bond excitation using transmission or reflectance configurations [76]. In cases where the polymer matrix has reacted with the aqueous environment and resulted in chemical degradation, such as hydrolysis or acidic/basic digestion, FTIR has been able to detect these reaction products and identify the process involved [52, 74, 77]. It has even been used to measure moisture sorption, and showed good agreement with gravimetric measurements [78, 79]. On the other hand, EDS is used for elemental mapping and relies on characteristic x-ray signals from elements heavier than boron [80]. Since it does not analyze chemical bonds or compounds, but the elements themselves, it is useful for 1D or 2D mapping of both location and concentration of contaminant particles, such as ions found in aqueous solutions [52, 59].

2.8 Modeling Approaches for Predicting Durability of FRP Composites

Phani and Bose [81] proposed a model that invokes viscoelasticity to explain losses in mechanical strength due to environmental degradation. The degradation processes considered were: (1) moisture-induced swelling that causes internal stresses, plasticization of the matrix, and deterioration of interfacial bond, and (2) viscoelastic relaxation of this swelling, based on a characteristic relaxation time τ, which depends on temperature [59, 81, 82]:

$$R_p(t) = R_{p\infty} + \left(1 - R_{p\infty}\right)e^{-t/\tau} \tag{20}$$

$$\tau(T) = \tau_0 \exp\left(\frac{-E_a}{RT}\right) \tag{21}$$

where $R_p(t)$ is the residual property at time t, $R_{p\infty}$ is the residual property at very large t (approaching infinity), τ is the characteristic relaxation time for damage to occur, R is the universal gas constant, and T is the exposure temperature. It is assumed that unless environmental conditions change, $R_{p\infty}$ is some limit to the loss of the property in question. Thus, this phenomenological model is based loosely on observed physical behavior of glassy polymers, but essentially uses a curve-fitting method for the mathematical formulation.

A different model was created by Pritchard and Speake [83] for predicting residual strength in FRP as a function of moisture content. No clear physical basis or mechanism was described in this model, but they found the predictions to agree with experimental data for glass/polyester composites at a wide range of temperatures, using the following:

$$R_p(t) = a\left(1 - e^{-bexp(-cM_t)}\right) + d \tag{22}$$

where M_t is the same as $M(t)$, and a, b, c, and d are all empirical constants to be found through curve-fitting. They did not clearly suggest a physical meaning for these constants.

2.9 Durability of CFRP in Concrete Structures: Research Need

Significant effort has been devoted to researching the durability of FRP used in concrete structures, considering moisture, temperature, and stress [5, 30, 60, 84, 59]. However, since concrete is an alkaline material, a major focus has been glass FRP (GFRP) since it is susceptible to alkali-silica reactions (ASR), whereas carbon fibers are more resistant to chemical attack and are less of a concern. Aramid (AFRP), basalt (BFRP), and hybrid FRP (HFRP) are becoming more prevalent as well. Robert and Benmokrane [74] found that by pre-loading GFRP bars to various levels of UTS, then unloading them before starting the solution exposure, notable changes in specific volume, moisture sorption, and residual strength were observed.

Despite the progress made in some aspects of durability characterization and predictive modeling for CFRP, more information is needed in alkaline environments and elevated temperatures, and stress effects are also rare in the literature [6]. Furthermore, a sound and repeatable testing protocol is needed for evaluating CFRP durability in the laboratory before use in concrete bridge structures [85]; improvements to current protocols could help researchers, designers, and state DOTs incorporate CFRP in their bridges more easily and confidently.

CHAPTER 3: EXPERIMENTAL APPROACH

3.1 Materials and Specimens

The material in this study is a well-known CFRP prestressing tendon having a seven-wire strand profile (Figure 2a), manufactured by Tokyo Rope Mfg. Co., Ltd., with the trade-name carbon fiber composite cable (CFCC). This pultruded composite comes from prepreg tows produced by a roving process, consisting of PAN carbon fibers (Toho Rayon) with nominal volume fraction $v_f = 0.68$ in an amine-cured epoxy matrix. After the matrix is cured, each wire is wrapped with a synthetic yarn to provide protection against UV radiation and abrasion, as well as to improve the bond performance with concrete.

Specimens were cut from the spool provided by the manufacturer (Figure 2b) using a carbide blade. Although the material is a seven-wire stranded cable, it was decided that the experiments could be simplified by using the single straight wire from the center—termed the center-wire or king-wire. The wires in a full cable do not always act in complete unison, and the six outer wires are spiral shaped, so standard mechanical tests would not yield representative stress/strain data; e.g., a tensile test would cause both tensile and shear stresses in the spirals, and a three-point load flexural test would not be suitable for such an irregular cross-section.

3.2 Environmental Conditions

Realistic field conditions for bridge structures can be very difficult to achieve in a laboratory, so common research practice is to err on the side of aggressive conditions. Since this study is mainly concerned with the durability of CFRP in reinforced and prestressed concrete bridge elements, such as piles and girders, the major factors considered for the environmental conditions were: (1) highly alkaline solution similar to concrete, (2) various temperatures similar to and more extreme than service conditions, and (3) effects of temporary tensile stress, such as resulting damage or other morphological changes.

3.2.1 Aqueous Solutions

Aqueous $Ca(OH)_2$ (calcium hydroxide) provides a high pH value with one of the core elements found in concrete (calcium). Since marine and brackish areas cause great concern for corrosion of prestressing steel, potentially encouraging implementation of CFRP, it is important to also consider saline (chloride) conditions as well. In addition to the $Ca(OH)_2$ solutions, a second solution made of $Ca(OH)_2$ combined with NaCl (sodium chloride) was included. For convenient nomenclature, the liquid that represents concrete pore solution (calcium hydroxide) is abbreviated CPS, and the combination with saltwater (sodium chloride) is referred to as CPSSW. To create the CPS, powdered $Ca(OH)_2$ product (Fisher Scientific) was mixed into de-ionized water at a concentration of 8.1 g/L, with a pH of 12.7. For the CPSSW mixture, crystalline powder NaCl was added to the CPS at a concentration of 31 g/L (water) and gave a pH of 12.5.

3.2.2 Immersion Temperatures

In the Virginia commonwealth, mean annual temperatures fall in a tight range between -3 and 32 ^{o}C (26–86 ^{o}F) [86]. However, as discussed in Sections 2.3-2.5, temperature is a major factor in the various degradation mechanisms common to FRP and can be used to accelerate aging. Therefore, the two solutions were poured into either PVC containers or glass beakers (depending on specimen type) and maintained at four temperatures—20 ^{o}C (68 ^{o}F), 40 ^{o}C (105 ^{o}F), 60 ^{o}C (140 ^{o}F), and 80 ^{o}C (176 ^{o}F)—with a fluctuation of about ±1 ^{o}C (1.8 ^{o}F), using stainless steel immersion heaters (Omegalux TH750, Omega Engineering) with integrated temperature controls and benchtop industrial ovens.

3.2.3 Pre-loading (Temporary Stress)

In addition to the environmental conditions mentioned, the effect of tensile stress in prestressed CFRP was also incorporated into the treatment for some CPS environments at 20 and 60 ^{o}C. Environmental exposure under sustained tensile stress is still ongoing—as part of a larger research project funded by VDOT—but the morphological effects of temporary prestressing loads were studied for this thesis. Therefore, due to the convenience and potential significance of accelerated durability testing with pre-loading compared to sustained loading, this approach was adopted for 75% UTS of the CFCC.

3.2.4 Summary

Considering the three environmental factors incorporated in the experimental program, the specimen labeling system used in this study is as follows:

Solution – Stress(%UTS) *– Temperature – Exposure Time*

For example, specimens subjected to CPS at 60 ^{o}C with pre-load for 1000 hours would be labeled as CPS-75-60-1000; likewise, a specimen from the environment with CPSSW at 20 ^{o}C with no pre-load for 1500 hours would be called CPSSW-0-20-1500. Table 4 summarizes the conditions studied in this thesis, showing the combinations of solution, temperature, and pre-loading. Considering limitations on laboratory equipment, space, and time, these conditions were not used for all specimen types—a complete test matrix is given after the testing methods employed are described in Section 3.3 (Table 6).

Table 4. Summary of combined environmental conditions for studying durability of CFCC.

Temperature (^{o}C)		20		40		60		80	
Medium		CPS	CPSSW	CPS	CPSSW	CPS	CPSSW	CPS	CPSSW
Pre-load	0% UTS	X	X	X	X	X	X	X	X
	75% UTS	X	-	-	-	X	-	-	-

3.3 Testing Methods

In order to better understand the durability of CFRP prestressing tendons in the realistic conditions described in Section 3.2, a rigorous testing program was devised. Some testing methods were proven, or at least very common, for FRP durability assessment while others were more exploratory. The intention for the experimental approach taken here was to obtain as much data as could potentially draw connections between properties that were scarce in the literature.

3.3.1 Physical Testing

Mass Gain (MG)

Mass changes were measured using a digital balance with 0.1 mg precision (Mettler, AE260). The specimens used for this physical/gravimetric testing were king-wires cut to 55 mm long. They were cut, the surfaces cleaned with soap and water, then dried completely and weighed before the exposure began. After the specified durations, specimens from each condition were removed and weighed after reaching a surface-dry state using a towel, before being immediately replaced in the environments. Since the aqueous environments selected for this study were alkaline and chloride (saline) solutions, dissociated ions from $Ca(OH)_2$ and NaCl populate the water and thus any sorbed moisture quantified by gravimetric methods must be corrected. To account for the ions in CPS and CPSSW, measured moisture was multiplied by the ratio of densities for water and solution:

$$M(t)_{cor} = M(t)\left(\frac{\rho_{wat}}{\rho_{sol}}\right) \tag{23}$$

to give the corrected moisture content, $M(t)_{cor}$, for the calculated densities of ρ_{CPS} = 1003 g/L and ρ_{CPSSW} = 1020 g/L (ρ_{wat} = 1000 g/L). Since the density of CPSSW is greater than CPS, containing more solute of heavier ions, the difference in perceived moisture sorption is actually less between the two solutions after this correction. The moisture contents presented in subsequent figures represent true water content rather than solution content, which means that any difference in sorption kinetics is due to the chemical nature of the solution.

3.3.2 Mechanical Testing

Uniaxial Tensile (UT) Testing

Tensile strength and modulus strain are primary mechanical properties pertaining to prestressed concrete, and since losses in these can negatively influence structural performance, tensile testing constitutes an important basic durability test. King-wire specimens were tested on a servohydraulic universal testing machine (810 Series, MTS), and strain data was collected with a noncontact laser extensometer (LX500, MTS). The gauge-length between laser targets was set at 50 mm. Based on ASTM D7502 [61], specimens were loaded at a strain-rate of 10^{-4} s^{-1} to ensure quasi-static failure without time-dependent loading effects. Regarding the free-length between grips, it was determined that a length-to-diameter (L/d) ratio greater than 50 was sufficient to cause proper failure without gripping interference; thus a free-length of about 300 mm (± 20 mm) was selected. Specimens were tested within one hour of removal from immersion to avoid any moisture loss or other changes. Tensile force, crosshead displacement, and laser displacement data were collected at a rate of 5 Hz.

Figure 19. Test setup for measuring uniaxial tensile properties of CFRP king-wires.

Short-beam Shear (SBS) Testing

Samples were cut to 30 mm lengths and loaded in a servohydraulic universal testing machine (810 Series, MTS) at a displacement rate of 1.3 mm/min, within one hour of removal from immersion. A fixture was fabricated to provide a span-to-thickness (*L*/*d*) ratio of 3.8. Force and crosshead displacement were recorded at a rate of 0.8 Hz (1.3 mm^{-1}), all according to the procedure described in ASTM D4475 [63].

Figure 20. Test setup for measuring intralaminar shear strength (ILSS) of CFRP through SBS testing.

Charpy Impact (CI) Testing

Charpy impact strength (CIS), or impact toughness in general, has very little value as a material property for CFRP in prestressed concrete design. However, impact toughness can be used as a relative value to measure changes after exposure to environmental conditions. This test was performed on specimens within one hour of removal from immersion using a standard Charpy/Izod pendulum tester with 45^{o} tup (Tinius Olsen) shown in Figure 21, having a striking velocity of 3 m/s and maximum impact energy of 330 J.

Figure 21. Charpy impact tester for measuring impact strength of CFRP.

3.3.3 Chemical Analysis

Energy Dispersive (X-ray) Spectroscopy (EDS)

Using point, line (1D), and mapping (2D) scans, the amounts and location of various elements can be established. Thus, the penetration of ions from the aqueous solutions can be mapped to correlate with the more approximate gravimetric method of measuring moisture sorption. EDS was performed using the SEM instrument described in Section 3.3.5.

3.3.4 Thermal Analysis

Differential Scanning Calorimetry (DSC)

Glass transition temperature (T_g) is a key property for polymeric materials, marking the transition from glassy to rubbery behavior. Since increased moisture content is known to decrease T_g, thermal analysis with DSC indicates whether a loss in mechanical properties has occurred. Any uncured resin left in the material undergoes post-curing when exposed to heat; as expected, both post-cure and degree of cure can be measured with DSC. Thermal analysis in this research was performed with a heat-flux DSC instrument (Q1000, TA Instruments) as shown in Figure 22, and with 6.7 mm aluminum pans and lids according to ASTM E1356. Within one hour of removal from immersion, samples were cut to about 1 mm thickness (~12 mg) using a diamond-coated saw blade, and heated at a rate of 10 ^{o}C/min within a temperature range of 0–200 ^{o}C and purged with nitrogen at 10 mL/min.

Figure 22. Q1000 (TA Instruments) DSC unit used for thermal analysis of CFRP.

3.3.5 Microstructural Analysis

Scanning Electron Microscopy (SEM)

In order to qualitatively observe degradation and other changes in morphology, microstructural analysis was conducted via SEM. Additionally, some features—like cracks and fiber-matrix interfacial debonding—can even be measured quantitatively through precise digital tools. This means results from other tests can be visually corroborated with microstructural characterization. Microscopic analysis was performed on exposed specimens, both tested and as-removed, using the field emission gun SEM (Quanta 650, FEI) shown in Figure 23.

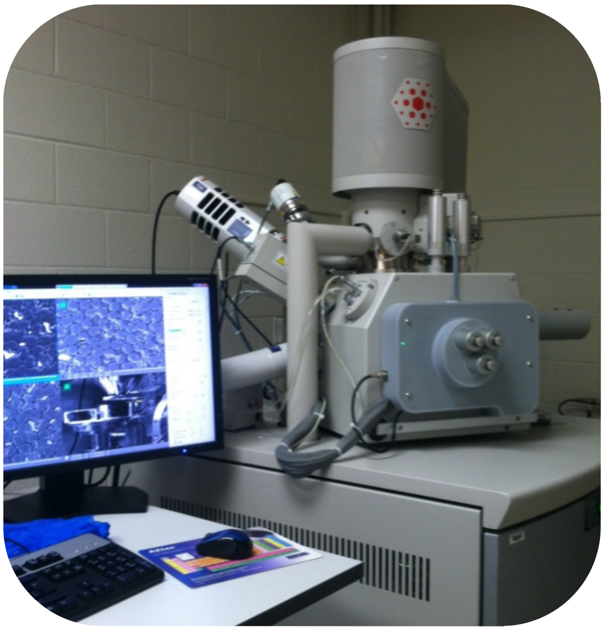

Figure 23. Quanta 650 (FEI) SEM used for microstructural analysis.

Extensive work was devoted to the sample preparation and imaging processes used with the SEM [87], and a summary is given here. Samples were pulse cut using a diamond wafer saw blade at 2000 rpm and a feed-rate of 0.1 mm/s with inert coolant. Two polishing methods were compared (Table 5), one using SiC (silicon carbide) paper from 600-grit down to 1200-grit, and the other using alumina slurry from 15 μm down to 0.5 μm particle size. This preliminary work helped determine that the alumina slurry method (Method 2) produced the best results for the time and materials required [87]. Two primary imaging methods were compared as well, one at higher accelerating voltages of 10 kV and a working distance (WD) of 10-12 mm on samples coated with 300 nm thick Au/PD, and the other at lower accelerating voltages of 1.0-1.5 kV and a WD of 8.5-10 mm on uncoated samples. While the uncoated method provided sufficient detail for general examination (fiber diameter, fiber volume content, large cracks), the coated method yielded much better results for higher magnifications.

Table 5. Polishing methods for CFCC samples observed in the SEM [87].

Method 1		**Method 2**	
Step	**Time (per sample)**	**Step**	**Time (per sample)**
600 grit SiC	3 min	15 μm alumina slurry	3 min
800 grit SiC	3 min	5 μm alumina slurry	3 min
1200 grit SiC	3 min	3 μm alumina slurry	3 min
1 μm alumina slurry	3 min	1 μm alumina slurry	3 min
-	-	0.5 μm alumina slurry	6 min
Total	12 min	Total	18 min

3.3.6 Test Matrix

The test matrix for studying the durability of CFRP used in prestressed concrete bridge applications is given in Table 6. Each test method described in Section 3.3 is listed by its abbreviation, according to the selected environments from Section 3.2 for that type of test.

Table 6. Test Matrix for Durability of CFRP.

Condition	Temperature (^{o}C)	20		40	60		80	
	Medium	CPS	CPSSW	CPS	CPS	CPSSW	CPS	CPSSW
Material Characterization	MG	X	X	X	X	X	X	X
	UT	X	X	-	X	X	-	-
	SBS	X	X	-	X	X	-	-
	CI	X	X	-	X	X	-	-
	EDS	X	X	-	X	X	-	-
	DSC	X	X	-	X	X	-	-
	SEM	X	X	-	X	X	-	-

CHAPTER 4: RESULTS and DISCUSSION

Results from the experimental methodology described in Chapter 3 are presented here, accompanied by an in-depth analysis inspired by the information given in Chapter 2. Interpretation of the analysis and the significance of all the present findings are discussed as well, and a newly developed model is compared to a well-known existing model for predicting the durability of CFRP composites used in concrete structures.

4.1 Moisture Sorption

4.1.1 Experimental Results

Based on the gravimetric method described in Section 3.3.1, moisture sorption profiles were compiled for the CFCC wires for all environmental conditions listed in the "MG" row of Table 6. These profiles are displayed in Figure 24 up to 1000 hours of exposure, beyond which the curves maintain the same trend as they slowly reach a long-term saturation. A consistent graphical nomenclature is used through this chapter: filled squares stand for CPS, empty squares for CPSSW, filled circles for pre-loaded CPS, and shaded triangles for air (control) specimens; grey indicates 20 ^{o}C, green is 40 ^{o}C, blue is 60 ^{o}C, and red is 80 ^{o}C.

Mass change was also measured for baseline specimens exposed to air at 60 and 80 ^{o}C in order to determine the true initial moisture content, the way CFCC would be delivered from the manufacturer. It was found to be 0.065% based on the identical mass loss for both temperatures up to 45 hours; after this point, mass loss comes from excess volatiles and fillers in the matrix and reached equilibrium after 500 hours of exposure time. Within the duration studied here, there was no observed mass loss that would indicate chemical or thermal breakdown of the epoxy.

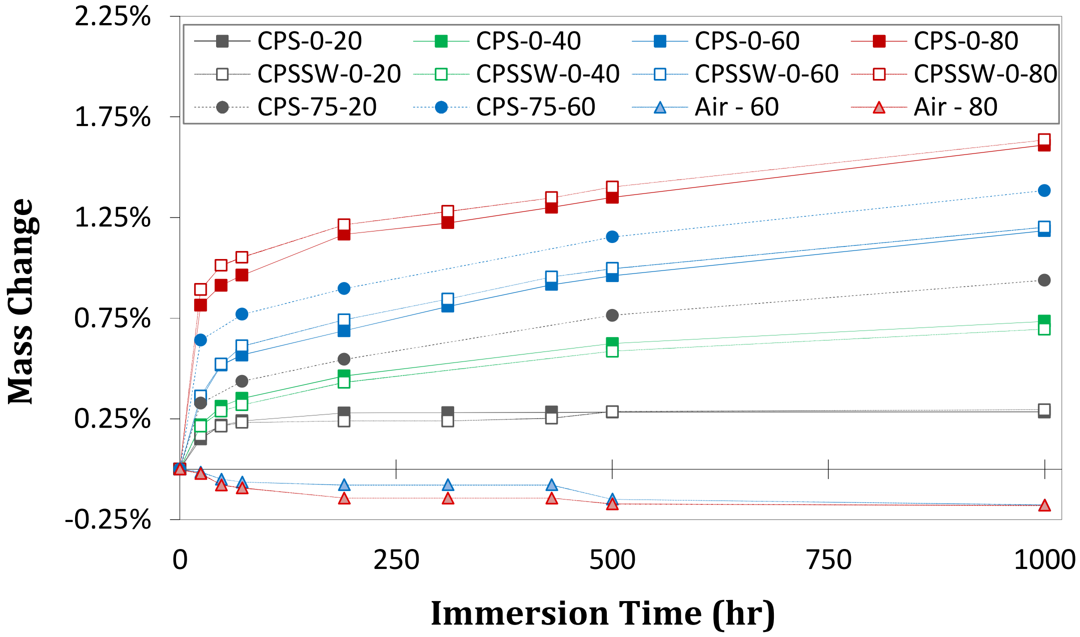

Figure 24. Moisture sorption profiles for all environmental conditions.

4.1.2 Moisture Sorption Predictions using a Two-Stage Fickian Model

To clearly view the moisture sorption profiles and to understand the connection between experimental data and theoretical predictions, the following figures will be separated into three categories: (i) specimens exposed to CPS without pre-loading (Figure 25), (ii) specimens exposed to CPS with pre-loading (Figure 26), and (iii) specimens exposed to CPSSW without pre-loading (Figure 27). The black lines are theoretical predictions using the two-stage Fickian-based model from Eq (8), with curve-fit model parameters listed in Table 7. Note that the time axis is displayed as the square-root of immersion time in sec$^{1/2}$ (instead of hour), since D is usually expressed as mm^2/s.

The thickness *h* in Eq (8) is substituted with the diameter *d* = 5 mm of a CFCC center-wire. The difference between a plate specimen with thickness *h* (for which the equation is derived) and a long rod with diameter *d* is likely to be negligible. Consider that in a wide plate like Figure 25(b), moisture can only effectively penetrate in the thickness direction due to the “restraint” provided by the vast width of the plate; an infinitesimal slice of the plate at an arbitrary location would experience the same sorption as any other slice. The long rod in Figure 25(a) can also be thought of as infinitesimal slices arranged in a circular pattern, with thickness *d* the same as *h*, and the restraint provided by adjacent slices would still restrict moisture penetration to a single direction. Thus, the two geometries can be considered nearly equivalent and this substitution in Eq (8) remains valid.

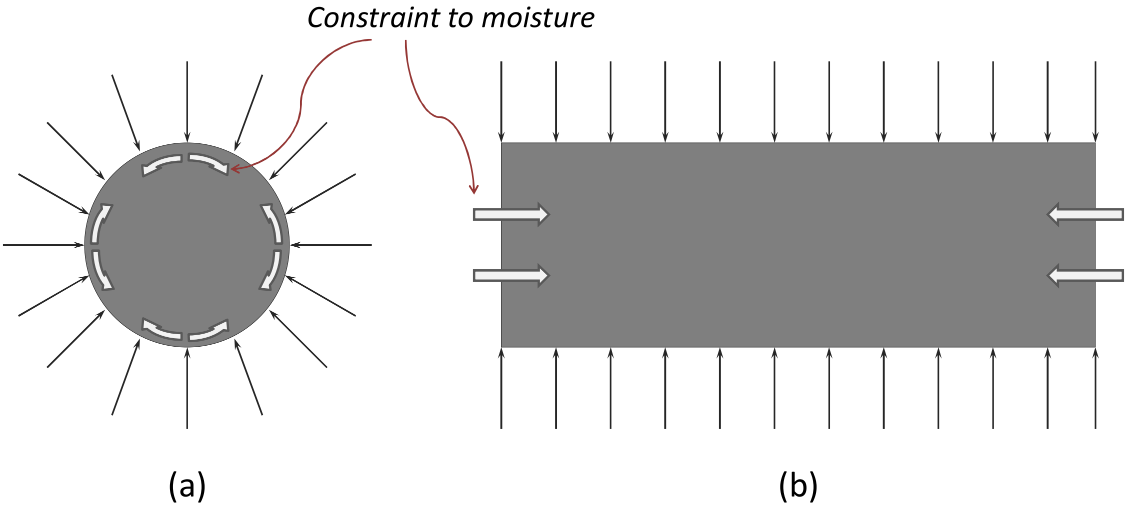

Figure 25. Moisture penetration for different geometries, considering (a) round rod used in this study, and (b) infinitely wide flat plate.

Table 7. Parameters used in the two-stage moisture sorption model in Eq (8) for all exposure conditions.

	CPS-0				**CPS-75**		**CPSSW-0**			
T (^{o}C)	20	40	60	80	20	60	20	40	60	80
M_∞ (%)	0.24	0.27	0.37	0.74	0.25	0.54	0.27	0.24	0.40	0.88
k (10^{-4} s$^{1/2}$)	1.00	9.44	11.40	6.35	15.00	8.00	0.10	9.00	11.00	4.90
D (10^{-4} mm^2/s)	1.7	2.2	3.0	5.0	5.5	7.7	1.9	2.3	2.8	4.5

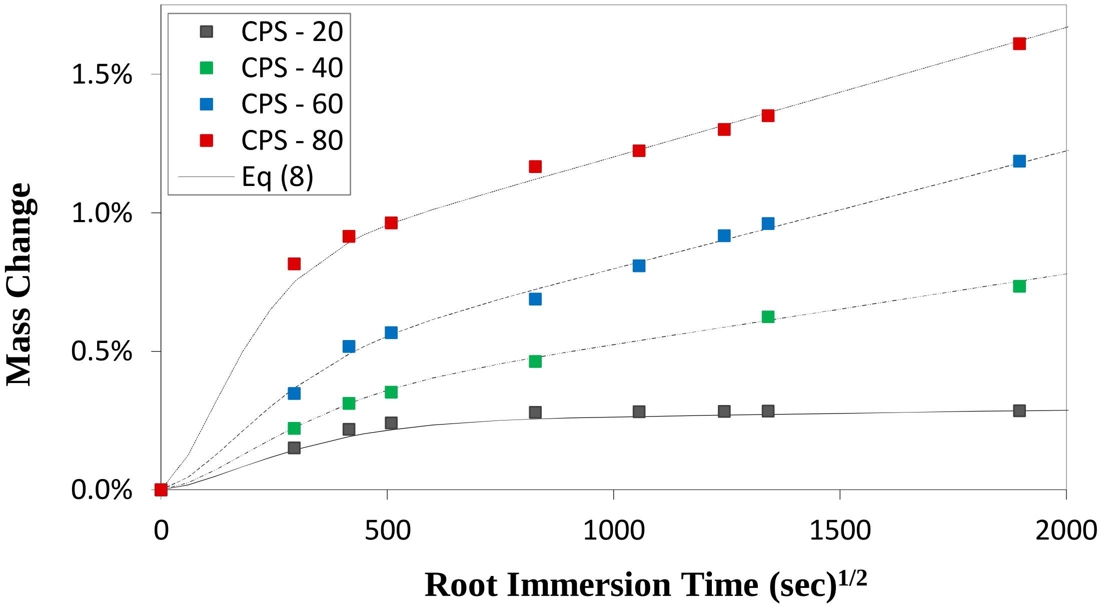

Figure 26. Moisture sorption profiles for the CPS-0 environment, compared to the two-stage model in Eq (8).

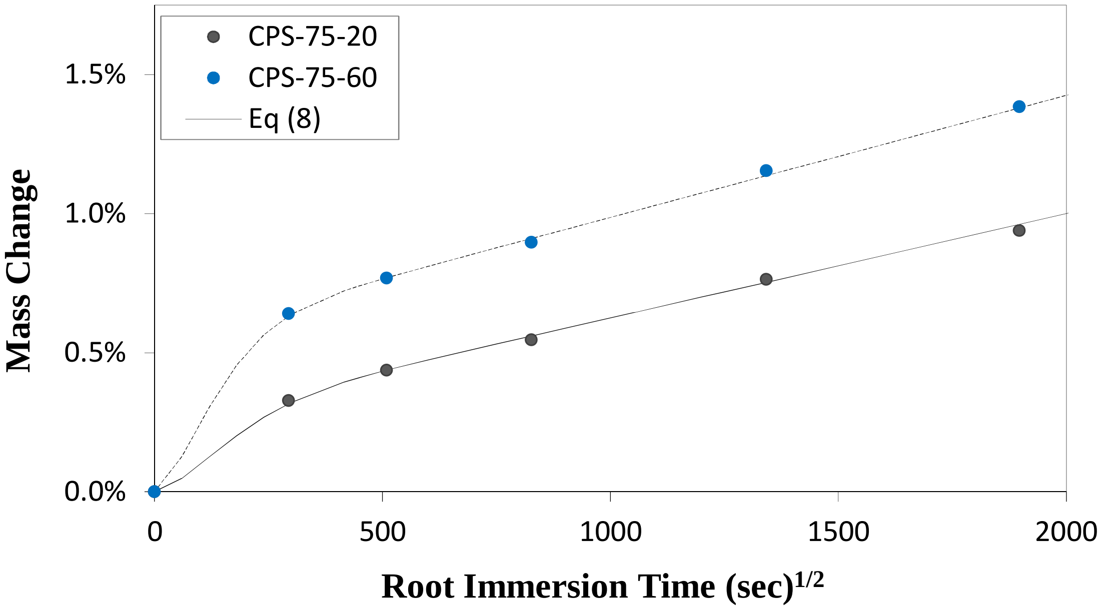

Figure 27. Moisture sorption profiles for the CPS-75 environment, with the two-stage model from Eq (8).

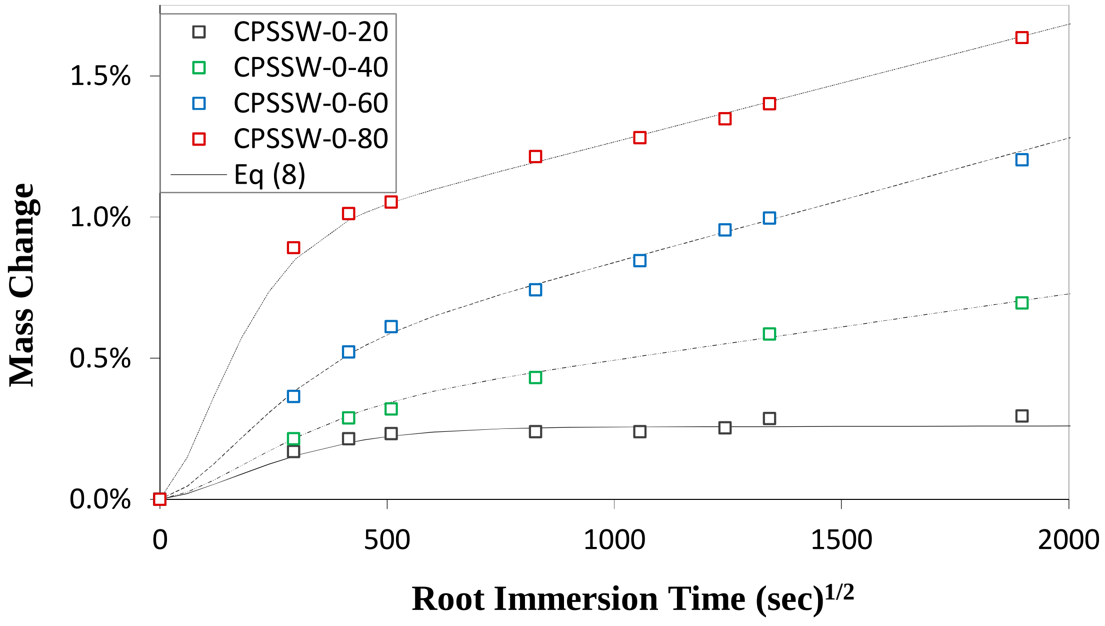

Figure 28. Moisture sorption profiles for the CPSSW-0 environment, fit with the two-stage model in Eq (8).

Temperature changes both the sorption rate and saturation level of moisture in CFCC, which is expected from diffusion theory. As temperature increases, free volume of the polymer matrix also increases, the stiffness of the polymer chains relax slightly, and the mobility of excited water molecules rises; these effects lead to the changes in sorption kinetics observed in all three specimen categories as temperature increases. Furthermore, there are significant changes between the CPS-0 and CPS-75 conditions, which can only be attributed to the morphological changes caused by pre-loading. Microcracks, interfacial debonding, change in polymer free volume, or a combination are likely responsible for these changes.

4.1.3 Thermodynamic Mechanisms for Predicting Sorption Kinetics

A quantitative method for examining these changes in sorption kinetics is based on thermodynamics, using activation energy (E_a) and heat of sorption (ΔH_{abs}). As alluded to in

Section 2.4.1, activation energy is the energy barrier than must be overcome by a mechanism in order for molecular motion to take place, such as diffusion, creep, and relaxation. When the combined energy from stress and temperature is sufficient, the barrier is overcome and motion occurs from the active mechanism. When multiple mechanisms are active, it can be much more difficult to isolate each one and quantify the activation energies involved. Likewise, according to van't Hoff's law, the saturation level of sorbed moisture in a polymer is dependent on temperature and can be calculated using Eq (7).

An example of the outcome of this calculation is given in Figure 29, for both Eq (5) and Eq (7) demonstrated with the CPS-0 condition (CPS-75 and CPSSW-0 are in Appendix A). Thus, the E_a and ΔH_{abs} values for each category (i-iii) are compared in Table 8 with the assumption that they represent similar temperature-dependent mechanisms, but are influenced by either (a) stress-induced morphological changes (pre-loading), or (b) the chemical effect of chlorides in solution.

The most noticeable difference lies in the activation energy for the pre-loaded CFRP (CPS-75), which is only 45% of the value without pre-loading. This clearly indicates that moisture moves much more freely through CFRP that has experienced tensile stress similar to concrete prestressing loads (75% UTS), even if it is released before immersion. If pre-loading simply increases the free volume of the epoxy, this decrease in E_a explains why water diffuses at a much higher rate, since less energy is needed to activate this sorption mechanism. If pre-loading causes damage like microcracking or interfacial debonding, then moisture could be transported via capillary flow (rather than diffusion) and could potentially occur in both the transverse and axial directions (see Figure 11). There is a very small decrease in activation energy in CPSSW-0 compared to CPS-0 (about 4% smaller). While this difference does not seem significant, the reason for even such a slight decrease could be that Cl^- ions change the chemical interaction between water and epoxy to create a smaller energy barrier.

Interestingly, it seems pre-loading has a marginal effect on ΔH_{abs} for moisture saturation (less than 3% increase), whereas CPSSW exhibits a greater influence (over 9% increase). This supports the assertion that the relationship between M_∞ and temperature can be described by van't Hoff's equation for dissolution, assuming ΔH_{abs} is constant over the temperature range tested. As expected from this hypothesis, heat of sorption is primarily influenced by the solution type, rather than immersion temperature or morphological features in the material.

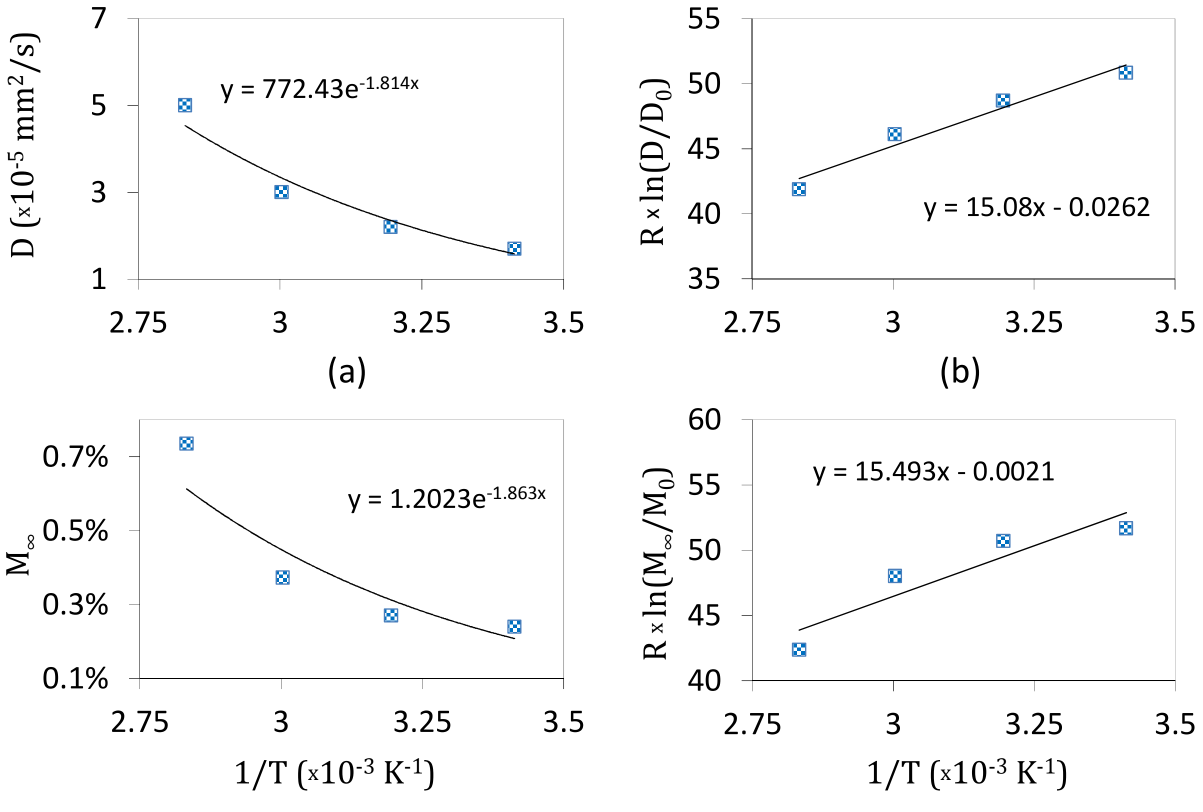

(a) (b)

(c) (d)

Figure 29. Thermodynamic parameters associated with CPS-0 environments calculated for (a,b) E_a using Arrhenius equation, and (c,d) ΔH_{abs} using van't Hoff's equation.

Table 8. Activation energy (E_a) and heat of sorption (ΔH_{abs}) calculated for CFCC.

Environment	D_0 (10^{-3} mm^2/s)	E_a (kJ/mol)	M_0 (-)	ΔH_{abs} (kJ/mol)
CPS-0	7.70	15.08	1.20	15.49
CPS-75	0.90	6.82	1.72	15.92
CPSSW-0	6.20	14.48	2.20	16.95

4.2 Tensile Properties

4.2.1 Experimental Results

In general, the tensile behavior of CFCC is typical for unidirectional CFRP, with a linear-elastic stress-strain response ending in brittle fracture. This is seen in Figure 30 for specimens with and without a pre-loading of 75% UTS. Only a slight decrease in strength (0.45%) and modulus (0.80%) was observed for pre-loaded "control" specimens, which is within the COV for specimens without pre-loading so it is considered insignificant. Results of uniaxial tensile testing (triplicate specimens) are listed in Table 9, after exposure durations of 1500 and 2000 hours.

The values in Table 9 are displayed graphically in Figure 31. In addition to changes in tensile strength and modulus over time in Figure 31(a) and (b), respectively, these changes are also shown with respect to corresponding moisture content in Figure 31(c) and (d). This offers a unique perspective for comparing the effects of various temperatures and solutions based on a common independent variable, $M(t)$. As long as moisture-induced degradation is the only—or at least, dominant—active mechanism in causing loss of strength and modulus, a consistent relationship between tensile properties and moisture content should exist. This is especially true for tensile modulus, as seen in Figure 31(d), for which all exposure conditions nearly overlap into a single profile; CPSSW deviates the most, compared to the CPS conditions. Conversely, although the data for tensile strength still overlap in Figure 31(c), this property seems most affected by pre-loading. This trend is continued from Section 4.1, where sorption kinetics were greatly influenced by pre-loading, but saturation mostly depended on solution chemistry.

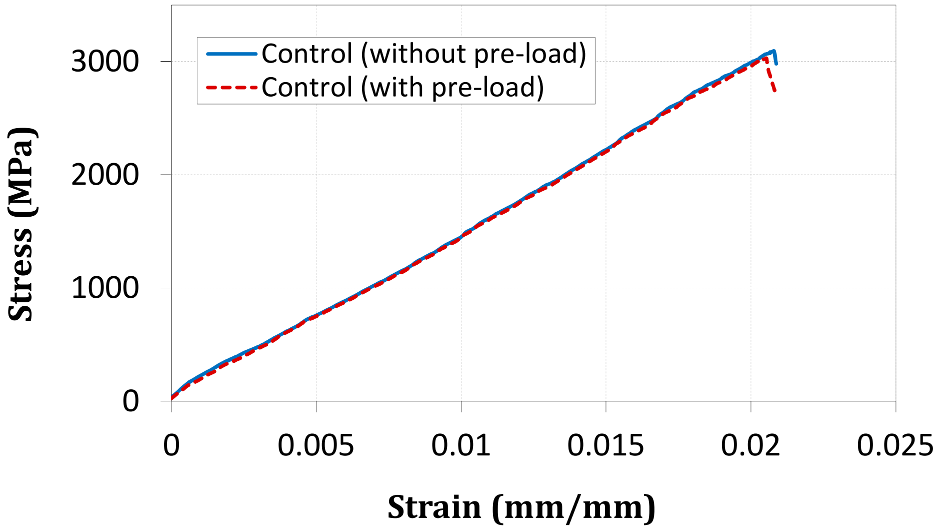

Figure 30. Tensile response of control specimens with and without 75% UTS pre-loading.

Table 9. Summary of tensile properties for control and exposed CFCC specimens.

Exposure Condition	**Exposure Duration** (hr)	**Tensile Strength** Average (MPa)	COV (%)	Residual (%)	**Tensile Modulus** Average (GPa)	COV (%)	Residual (%)
Control (0% UTS)	0	3094	2.2	100	150.3	1.3	100
Control (75% UTS)	0	3080	3.2	99.56	149.1	1.6	99.2
CPS-0-20	1500	3082	2.6	99.62	150.0	1.8	99.80
	2000	3076	3.1	99.42	149.9	1.9	99.73
CPS-0-60	1500	3030	4.3	97.95	149.7	2.7	99.60
	2000	3021	3.5	97.64	149.4	2.0	99.40
CPS-75-20	1500	3028	4.1	98.32	148.7	3.1	99.73
	2000	3019	4.7	98.01	148.6	1.9	99.66
CPS-75-60	1500	2979	4.6	96.71	148.4	2.4	99.50
	2000	2966	6.2	96.31	148.1	2.2	99.33
CPSSW-0-20	1500	3079	2.8	99.53	149.9	0.9	99.73
	2000	3072	2.2	99.29	149.7	2.0	99.63
CPSSW-0-60	1500	3025	2.7	97.77	149.6	2.8	99.55
	2000	3012	4.4	97.37	149.3	3.3	99.35

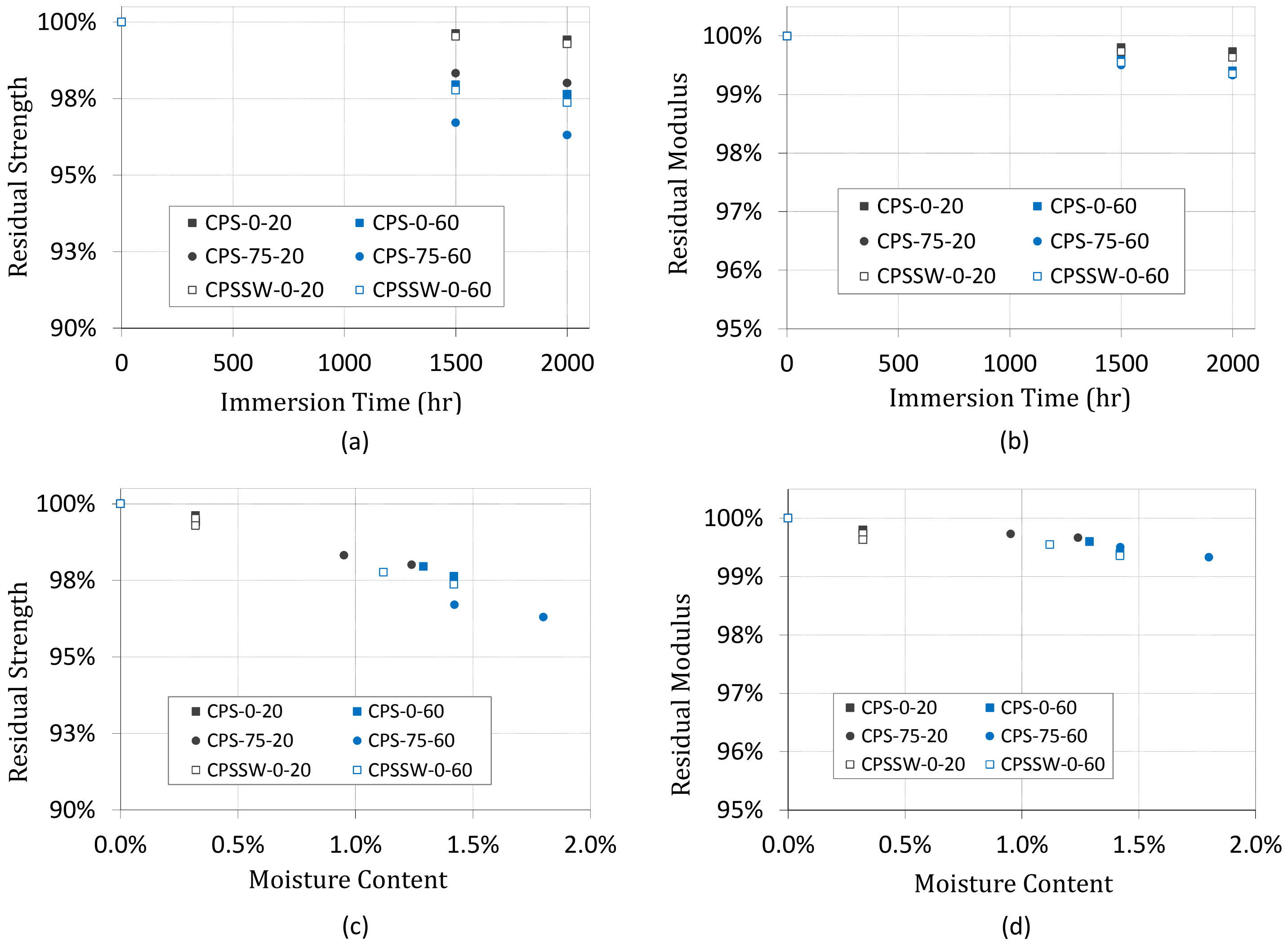

(a)

(b)

(c)

(d)

Figure 31. Residual tensile properties after 1500 and 2000 hours of exposure: (a) strength over time, (b) modulus over time, (c) strength at corresponding moisture content, and (d) modulus at corresponding moisture content.

4.3 Intralaminar Shear Strength

4.3.1 Influence of Yarn Wrapping

As described in Section 3.1, CFCC is a seven-wire cable and each wire is wrapped in synthetic yarn to protect the CFRP from abrasion and UV radiation. While the yarn does not change the axial tensile properties of the wire, it does impose transverse confinement that influences the intralaminar shear behavior measured via SBS testing in Figure 32. The actual ILSS, or the peak stress at the end of the linear portion of the force-displacement curve, is 6.8% greater for CFCC with the yarn wrapping. The apparent stiffness for wrapped CFCC is 13% lower, which is most likely because the measured deflection is a combination of actual specimen displacement and through-thickness compression of the wrapping itself. The most significant effect from the yarn wrapping is the arrested delamination observed after the ILSS peak, compared to the progressive delamination experienced by the unwrapped specimens. In fact, the wrapped CFCC continues to carry increasing applied force as the yarn begins to resist delamination through hoop stresses. Figure 33 shows the difference in delamination between wrapped and unwrapped SBS specimens.

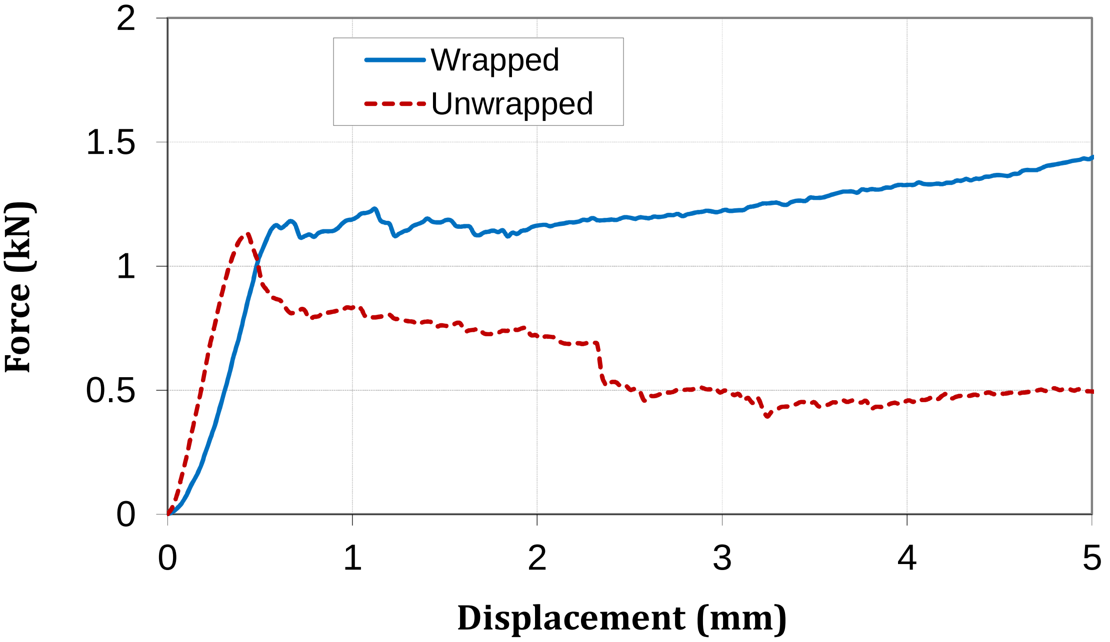

Figure 32. Intralaminar shear behavior of specimens with and without synthetic yarn wrapping.

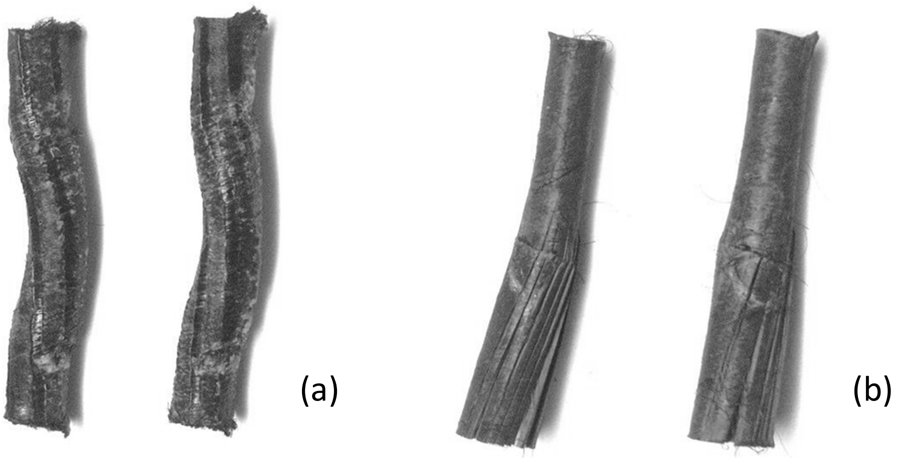

Figure 33. Failed specimens after SBS testing, showing (a) wrapped specimens with arrested delamination, and (b) unwrapped specimens with extensive delamination.

The implications of this are twofold: (1) CFCC has greater resistance to shear with the yarn wrapping, which is beneficial for in-service performance, and (2) CFCC specimens should be unwrapped for SBS testing in order to accurately reflect degradation caused by environmental exposure, which is the intended purpose of the test. Therefore, all subsequent specimens were unwrapped to measure ILSS with SBS testing.

4.3.2 Experimental Results

The overall intralaminar shear behavior and failure mode of the SBS specimens remained the same for all environmental conditions and exposure durations, shown in Figure 34 using 1500 hour exposure as an example. This denotes a similar degradation process among all the conditions in this study, since a change in failure mode and progression might suggest the presence of an environmental effect that is unseen from ILSS values alone. On a related note, the full force-displacement curves in Figures 32 and 34 provide information about the delamination-dominant failure mode evident in Figure 32. After the peak ILSS is reached, additional inelastic energy is dissipated through delamination-based fracture as resistance to applied force decays.

Upon closer inspection of the decaying portion of the curves, it was observed that the numerous sharp drops in force were the result of progressive delamination: each drop corresponds to a new delamination site. Thus, the specimen delaminates into two halves at the neutral axis upon reaching the ILSS, after which both halves behave as individual short beams and additional delamination occurs to create four sections; this continues until the midspan deflection is large enough to make further delamination difficult by changing the stress state. By comparing the general shape of the curves of exposed specimens in Figure 34 to control specimens in Figure 32, there seems to be a more gradual peak at the ILSS, rather than a sharp drop. This seems to point toward plasticization of the epoxy, resulting in less brittle behavior.

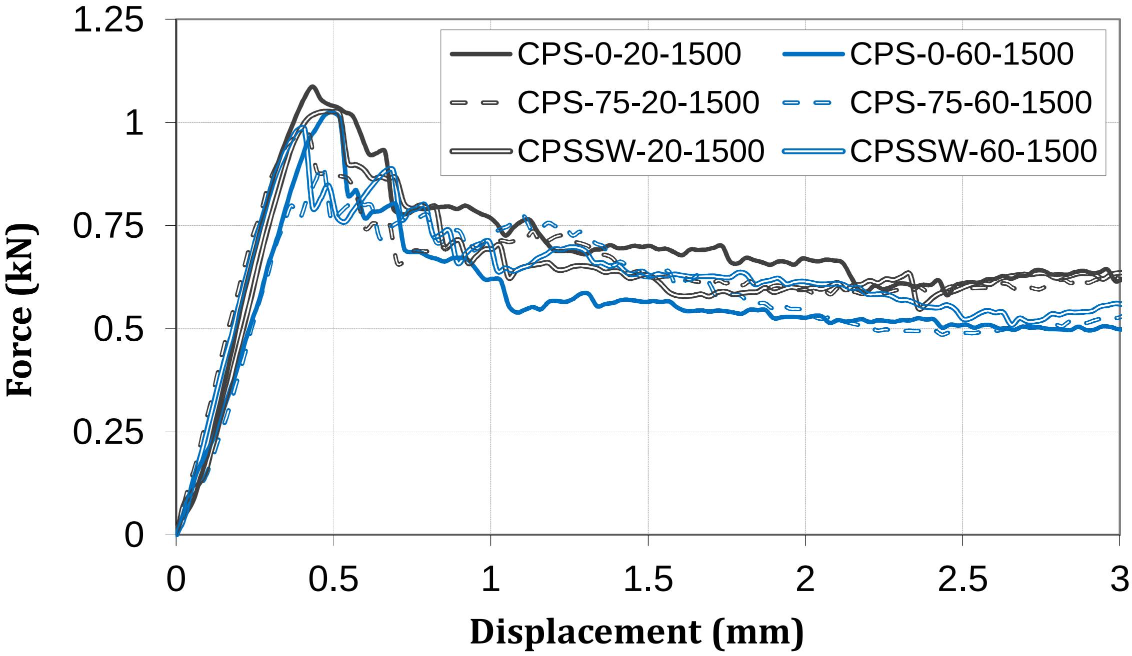

Figure 34. Intralaminar shear behavior of CFCC wires after 1500 hours of exposure.

The results of SBS testing are listed in Table 10 for all environmental conditions in this study after 500, 1500, and 2000 hours of exposure. The residual ILSS is also shown visually with respect to both time and moisture content in Figure 35(a) and (b), respectively. There is a distinct trend in ILSS for all environmental conditions, wherein a rapid loss happens sometime in the first 500 hours, after which the decrease is much more gradual. Similarly to the tensile properties, the ILSS at corresponding moisture contents for different environments overlap to some degree. Once again, the pre-loaded specimens tend overlap into a separate profile from the other specimens, showing greater losses due to the morphological changes caused by pre-loading. However, unlike the tensile properties, the ILSS suffers much more from even the mild environments and shows losses up to 18% for the severe case (CPS-75-60). Thus, the sensitivity of the ILSS to environmental effects supports the prominent use of the SBS test as a central component of durability testing programs for FRP composites.

Table 10. Summary of ILSS from SBS testing for control and exposed CFCC specimens.

Exposure Condition	**Exposure Duration** (hr)	**ILSS** Average (MPa)	COV (%)	Residual (%)
Control (0% UTS)	0	38.40	2.8	100
Control (75% UTS)	0	36.57	3.4	95.24
CPS-0-20	500	37.41	1.8	97.43
	1500	37.19	2.3	96.85
	2000	37.16	2.5	96.77
CPS-0-60	500	35.83	3.1	93.31
	1500	35.17	1.4	91.59
	2000	34.78	2.2	90.58
CPS-75-20	500	31.61	1.9	90.76
	1500	31.27	2.8	89.79
	2000	30.84	4.7	88.55
CPS-75-60	500	29.81	4.0	85.58
	1500	28.95	2.9	83.13
	2000	28.74	4.2	82.52
CPSSW-0-20	500	36.85	1.8	95.98
	1500	36.23	1.8	94.37
	2000	36.08	2.2	93.95
CPSSW-0-60	500	35.17	2.5	91.58
	1500	34.27	1.3	89.25
	2000	33.81	3.7	88.04

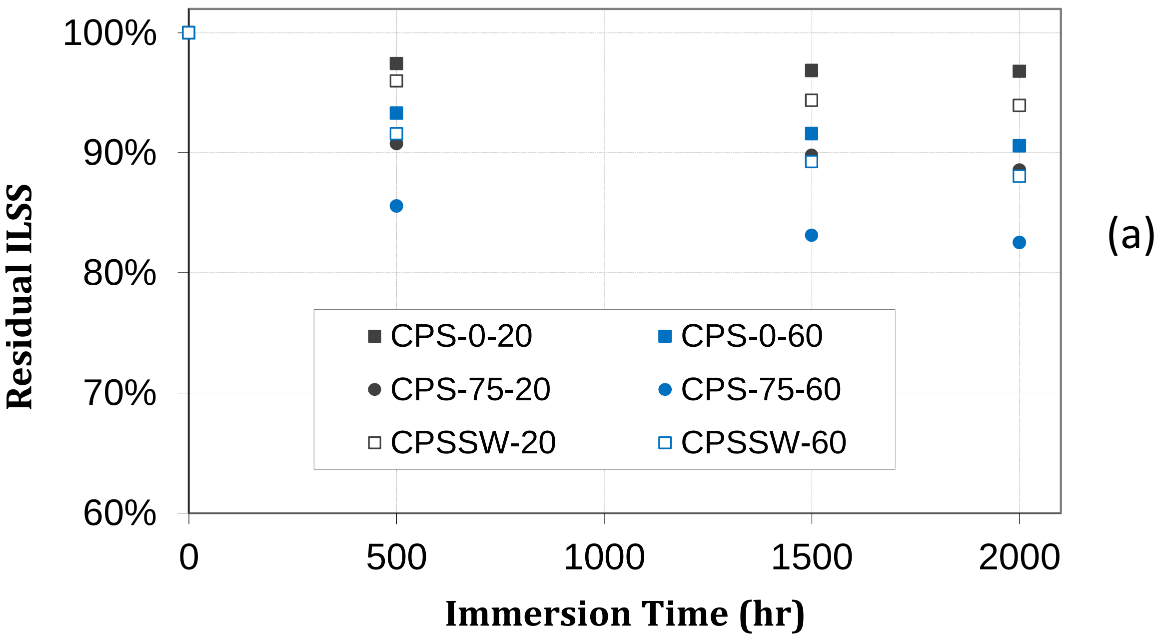

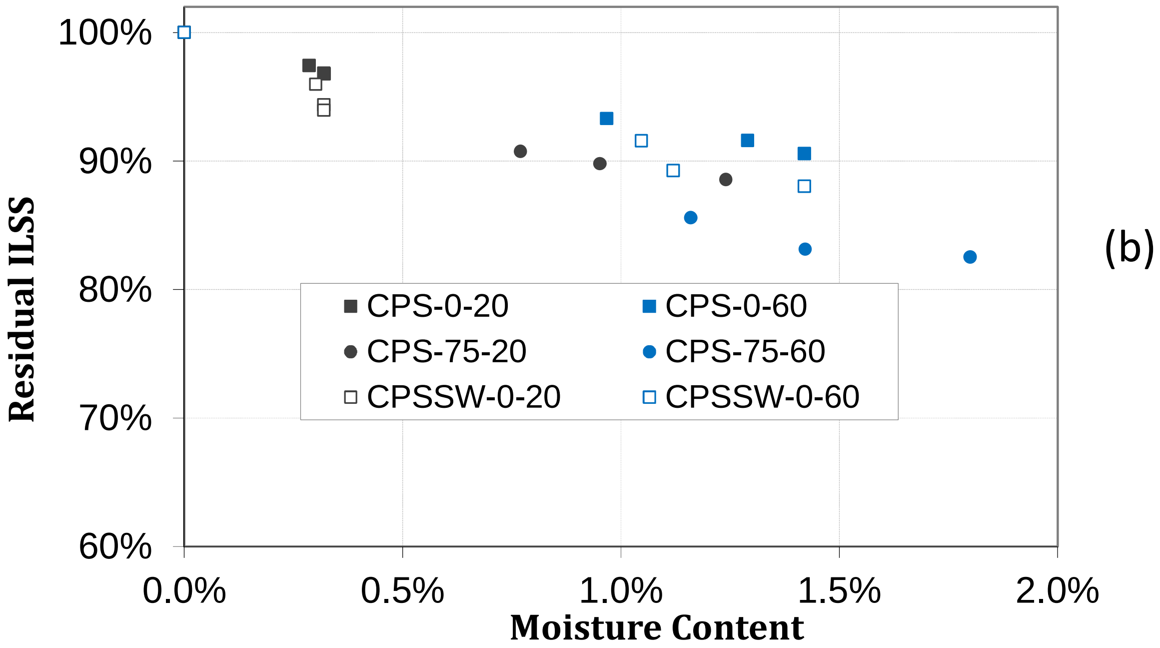

Figure 35. Residual ILSS after 500, 1500, and 2000 hours of exposure: (a) strength over time, and (b) strength at corresponding moisture content.

Intralaminar shear strength is controlled by matrix and interfacial failure, which means matrix plasticization or cracking and interfacial debonding is responsible for reduction in the ILSS. An example of a typical fracture surface after SBS testing is shown in Figure 36 as captured by SEM, with clear debonding in areas with smooth fiber surfaces and some matrix shear failure manifested by the jagged areas, called *hackles*. If the interface was less affected by the environment, matrix shear would be the principal failure mechanism in SBS testing and there would be more hackles with less fiber surface area exposed. The example in Figure 36 certainly shows a combination of interfacial and matrix failure, but it looks like interfacial debonding is more prominent.

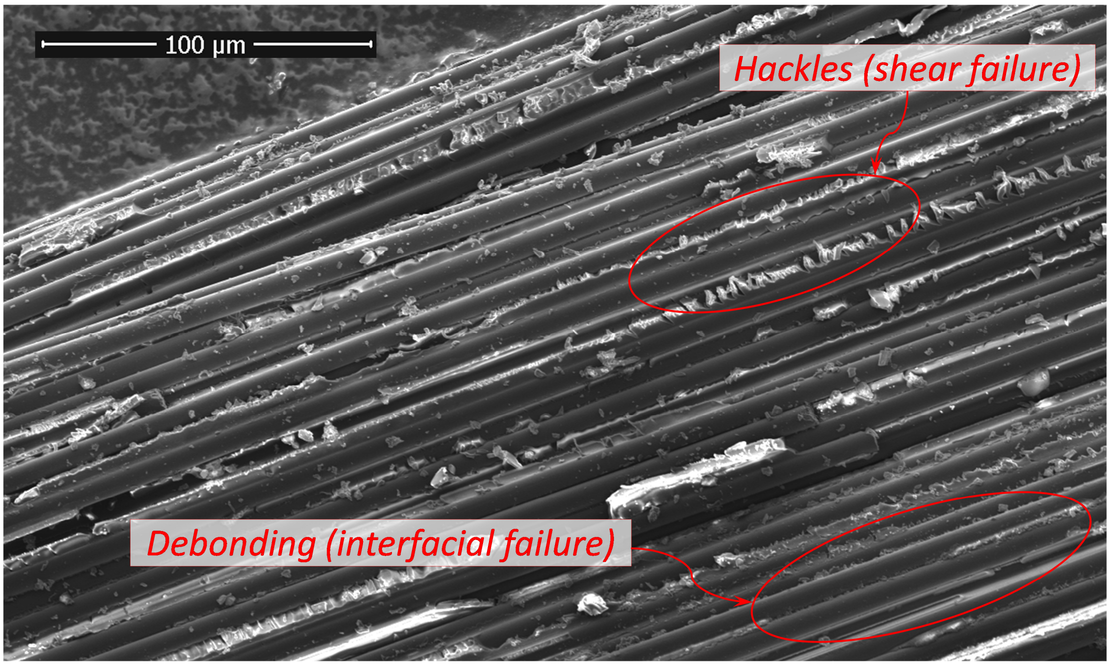

Figure 36. Fracture surface after SBS testing, showing extensive interfacial debonding and matrix failure (examples circled in red).

4.4 Charpy Impact Behavior

4.4.1 *Experimental Results*

Charpy impact strength (CIS) indicates the energy absorption behavior of CFRP under dynamic flexural loading, so it is not always directly related to quasi-static strength (tensile, flexural, or shear). This convenient method was included in the experimental program in order to assess its utility for measuring relative material degradation in a durability testing program. Table 11 contains the results of Charpy impact testing using the slotted notch configuration for all environmental conditions after 500, 1500, and 2000 hours of immersion. These results are also displayed visually with respect to both time and moisture content in Figure 37(a) and (b), respectively. As anticipated, the CIS data for pre-loaded specimens seem to overlap into a distinguishable profile with respect to $M(t)$, while the rest form a separate profile.

The data follows the same overall trend as ILSS, decreasing sharply until 500 hours and then transitioning to a very gradual state of decay. Another similarity is the notable influence of higher temperature and pre-loading on residual impact behavior, which supports the findings from SBS testing. In fact, the observed losses between the two test methods were of comparable magnitude and it can be assumed that they provide nearly equivalent information in terms of environmental effects. This close agreement shows that Charpy impact testing can be a simple, yet useful method for evaluating environmental durability of FRP composites.

Table 11. Summary of CIS results for control and exposed CFCC specimens.

Exposure Condition	**Exposure Duration** (hr)	**Charpy Impact Strength** Average (kJ/m^2)	COV (%)	Residual (%)
Control (0% UTS)	0	661.1	5.5	100
Control (75% UTS)	0	628.0	7.4	95.80
CPS-0-20	500	614.8	4.3	93.08
	1500	606.2	3.8	91.69
	2000	602.9	6.5	91.20
CPS-0-60	500	595.0	5.1	90.11
	1500	577.2	2.4	87.31
	2000	568.5	5.3	86.02
CPS-75-20	500	556.1	7.7	88.55
	1500	534.9	4.8	85.16
	2000	524.4	8.7	83.53
CPS-75-60	500	527.3	6.3	83.96
	1500	504.5	8.9	80.34
	2000	506.2	7.0	80.60
CPSSW-0-20	500	612.8	2.8	92.70
	1500	610.6	5.8	92.37
	2000	588.4	3.9	89.05
CPSSW-0-60	500	578.4	8.1	87.50
	1500	566.1	5.3	85.63
	2000	555.3	5.6	84.00

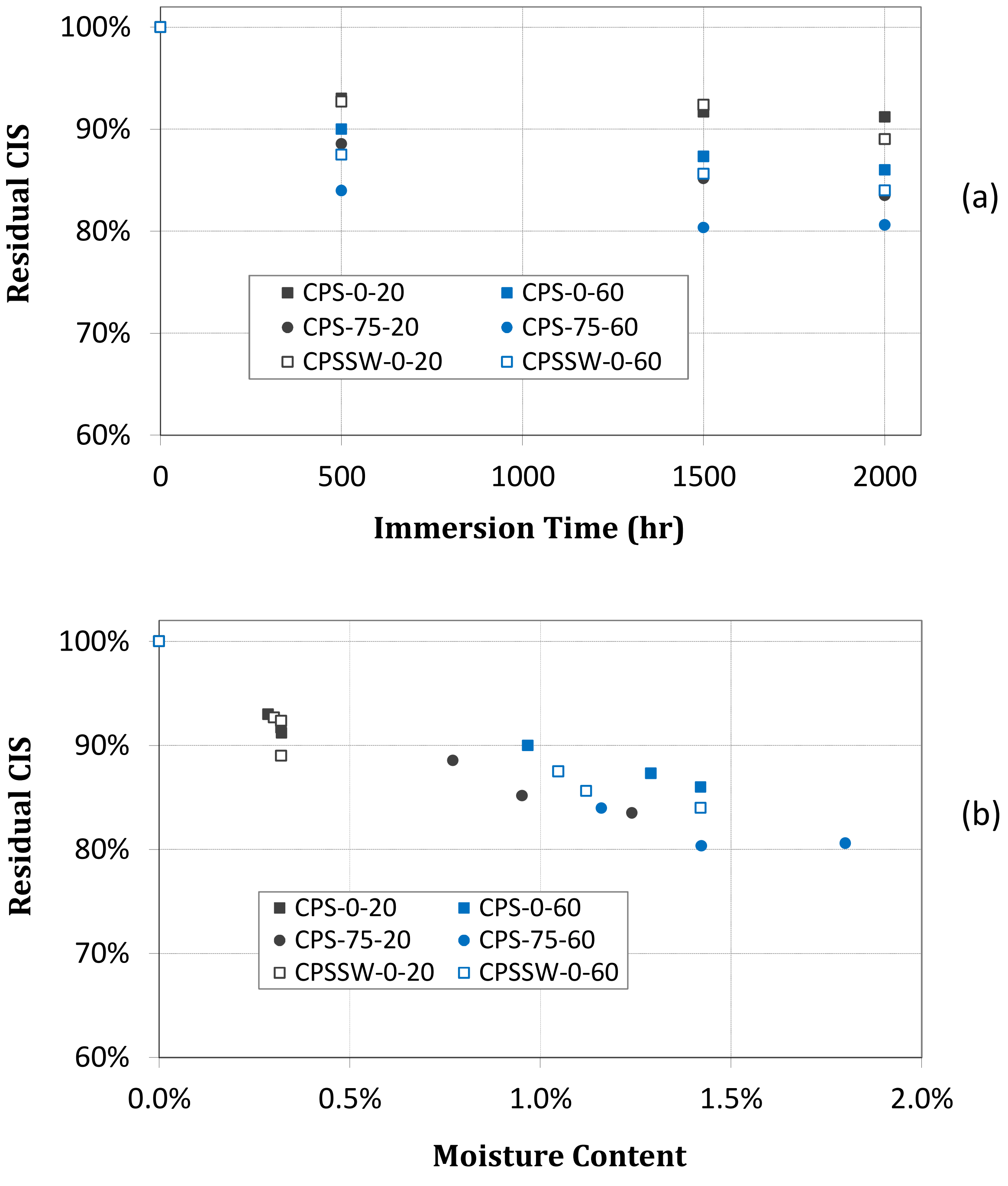

Figure 37. Residual CIS after 500, 1500, and 2000 hours of exposure: (a) strength over time, and (b) strength at corresponding moisture content.

The similar trends between CIS and ILSS warranted further analysis to find a meaningful relationship. Three cases were considered regarding the dominant parameter that governs the correlation between CIS and ILSS: (1) temperature is dominant, regardless of pre-loading or solution-type, (2) pre-loading is dominant, regardless of temperature or solution-type, and (3) solution-type is dominant, regardless of temperature or pre-loading. These three cases are shown in Figure 38(a), (b), and (c) respectively. Interestingly, the relationship between CIS and ILSS has the strongest correlation for data grouped by solution-type, followed by temperature and pre-loading. Therefore, inferring losses in ILSS due to environmental degradation based on CIS data from the same solution-type is a valid approach.

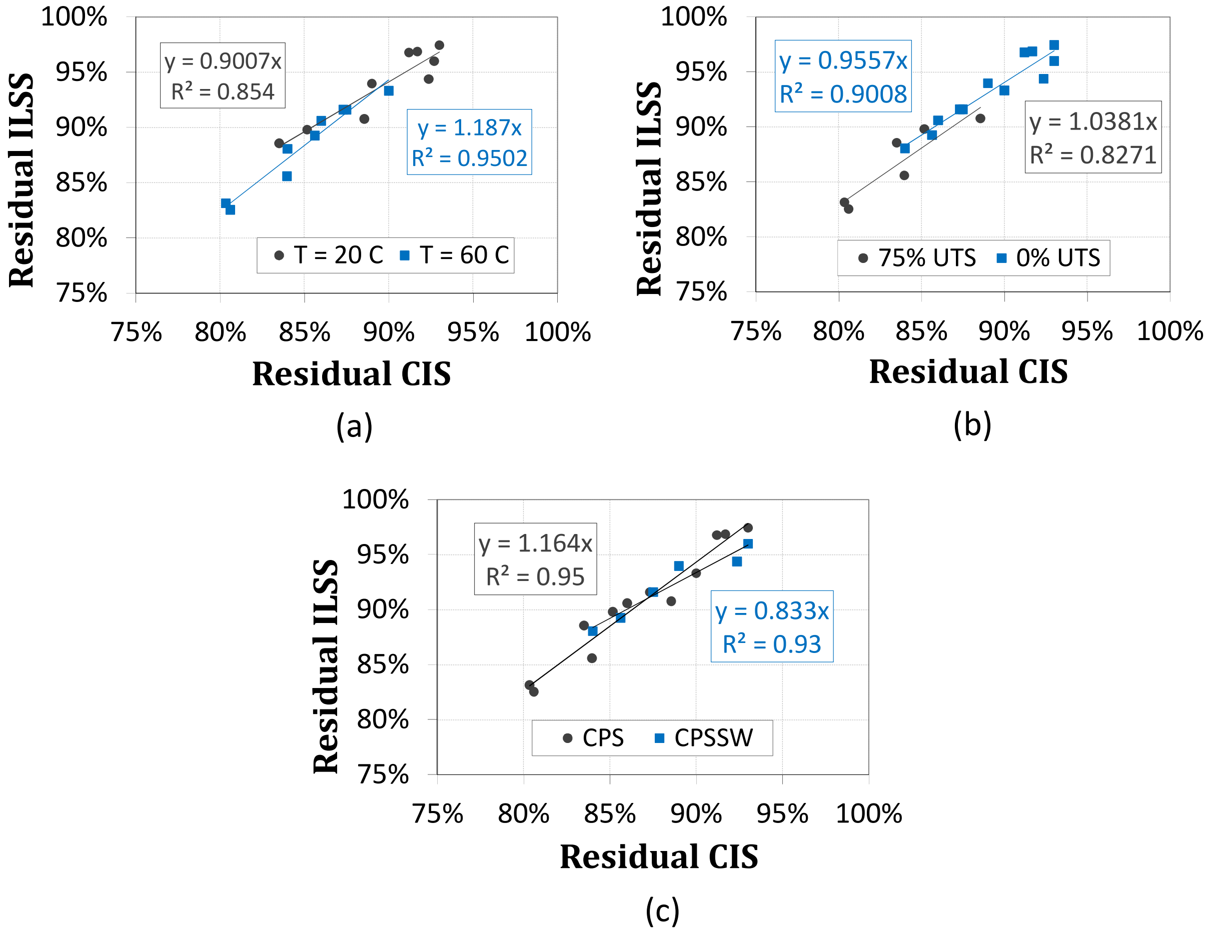

(a)

(b)

(c)

Figure 38. Relationship between residual CIS and residual ILSS for three environmental exposure parameters: (a) temperature, (b) pre-loading, and (c) solution.

4.4.2 Failure Mode and Fractographic Analysis

Specimens from all environmental conditions exhibited identical failure modes from Charpy impact testing; flexural failure was caused primarily by fiber pull-out in the tension zone, with the secondary failure mechanism of kink-banding in the compression zone. A typical failed specimen is shown in Figure 39.

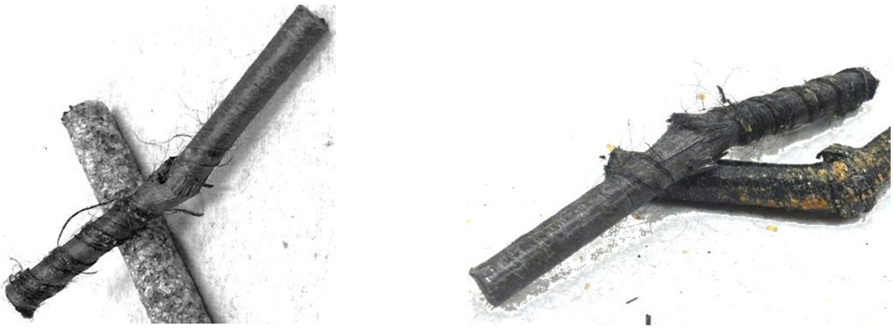

Figure 39. Failed specimen showing the compression/impact side (*left*) and tension/notched side (*right*).

In addition to exhibiting identical failure modes, specimens from all environments also displayed the same microscopic failure mechanisms when viewed with SEM. The degree of fiber pull-out in the tension zone of the fracture surface was so extensive, there is no doubt this was the governing failure mechanism. Fiber pull-out failure is depicted in Figure 40 for a specimen exposed to the CPSSW-0-60 environment. Figure 41 contains images starting from the cross-section and magnifying to the fiber level, showing details of the fracture surface at the tip of the notch; i.e., the extreme tensile surface at the moment of impact. Some small areas of matrix failure are signs that the bond remains intact in localized regions. As the fiber-matrix interface continued to lose integrity over time, the material system’s ability to absorb impact energy, and to effectively transfer stresses between fibers on a very short time-scale, was significantly affected. Fractographic analysis using SEM proved effective for visually identifying the failure mechanisms behind the macroscopic failure mode and data that were observed.

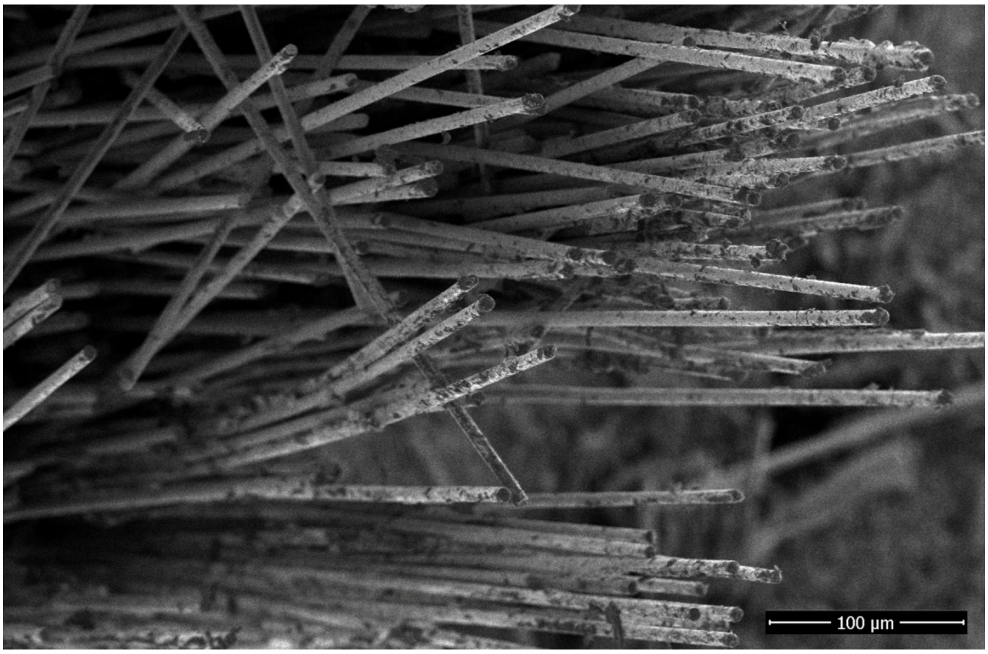

Figure 40. Fracture surface in the tension zone, showing extensive fiber pull-out with trace amounts of epoxy on the fiber surfaces.

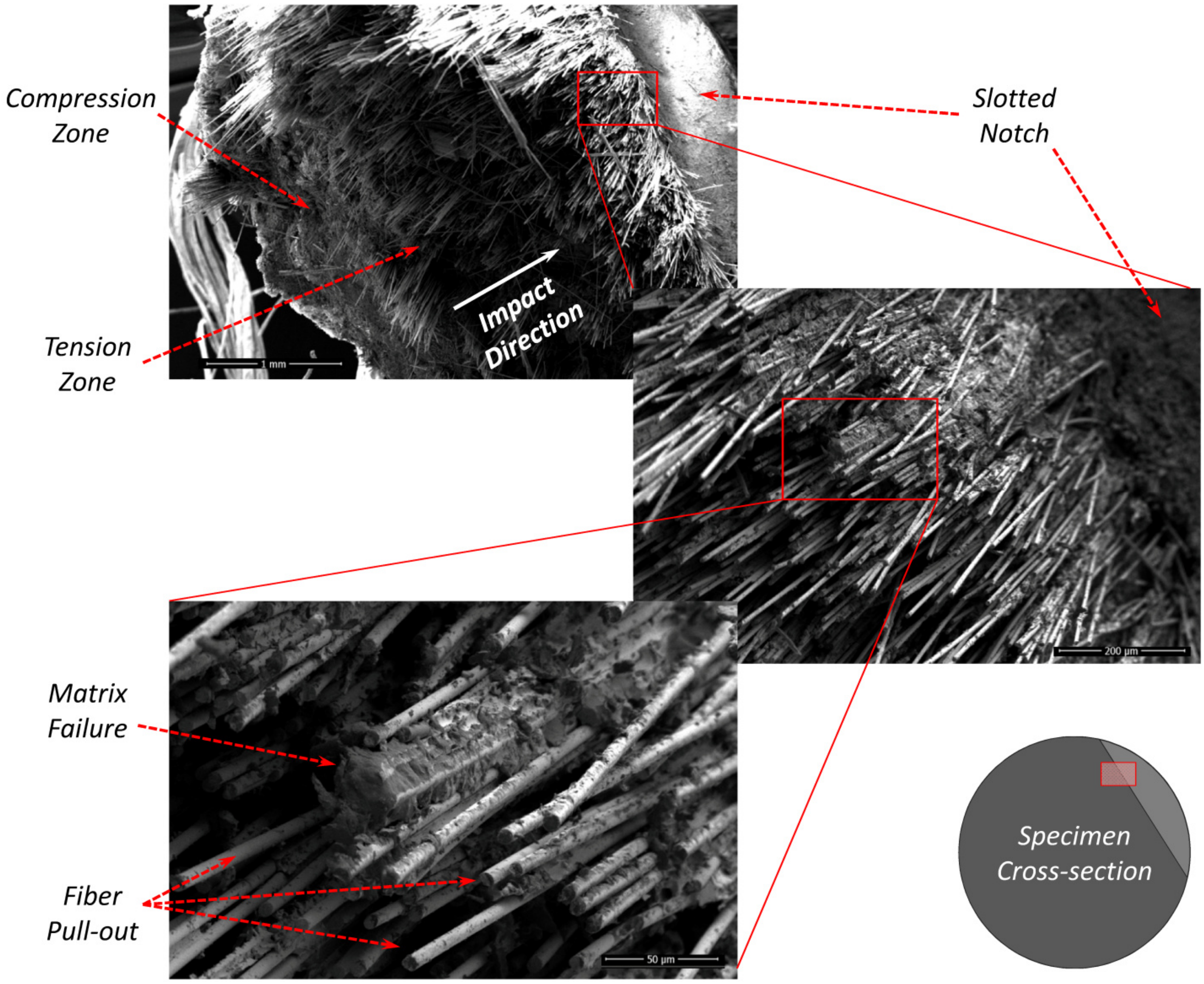

Figure 41. Progressively microscopic view of failure surface in the tension zone at the notch, showing some matrix failure interspersed in fiber pull-out.

4.5 Thermal Analysis

The glass transition temperature (T_g) for control specimens was measured as 109.6 ^{o}C based on the second run. The first run contains a large endothermic peak that starts around 75 ^{o}C before a faint transition; this peak represents some enthalpy recovery from physical aging that occurred from being stored at room-temperature between manufacturing and testing. The second run reveals the true T_g and these features are illustrated in Figure 42.

Results from DSC for all environmental conditions are listed in Table 12, and plotted in Figure 43 with respect to both immersion time and moisture content. It is clear from Figure 43(a) that higher temperature causes greater rate of depression in T_g for both solutions, yet the influence of pre-loading is quite unclear—reduction for CPS-75-20 is much greater compared to CPS-0-20, while results for CPS-75-60 are much closer to CPS-0-60. However, by examining the data in terms of moisture-induced changes in Figure 43(b), a distinct linear relationship becomes clear between T_g and $M(t)$ regardless of temperature, pre-loading, or solution-type.

Recalling that the depression mechanism for T_g in thermosetting polymers is the increase in free volume caused by plasticization and relaxation of molecular chains, which are activated by sorbed moisture [36, 37], the validity of the empirical relationship in Figure 43(b) is supported by physical principles. Furthermore, this correlation substantiates the approach of analyzing residual mechanical properties (Sections 4.2-4.4) with respect to moisture content, since T_g is the intermediate property that indirectly relates them.

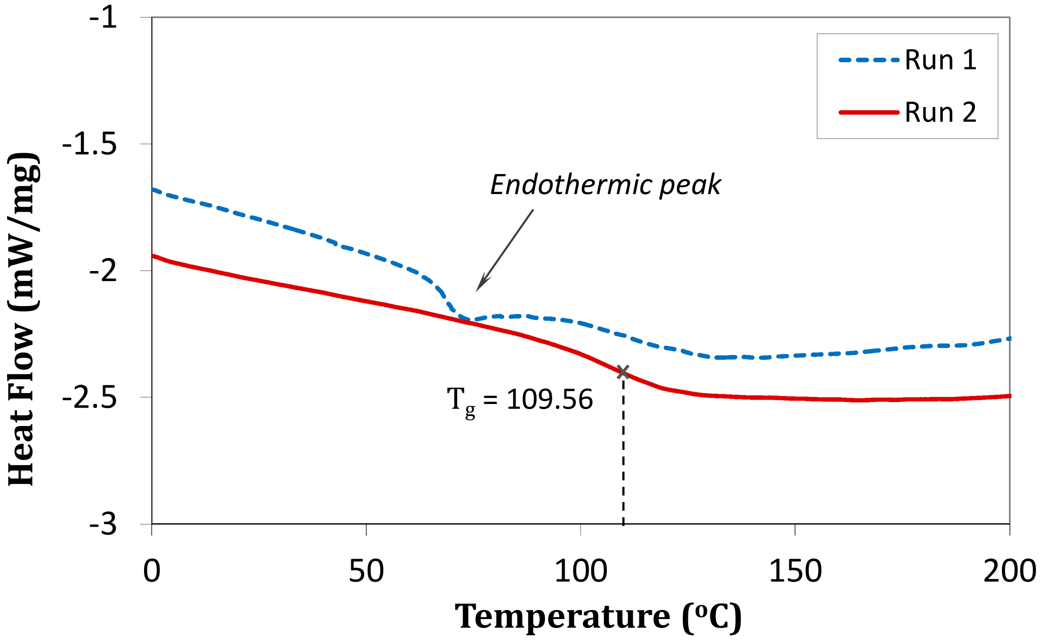

Figure 42. Thermogram from DSC analysis for CFCC control specimens (using two runs).

Table 12. Summary of T_g measured by DSC for control and exposed CFCC specimens.

Exposure Duration (hr)	**Exposure Condition**	T_g (°C)	**Exposure Condition**	T_g (°C)
0	Control	109.6		
500 1500 2000	CPS-0-20	103.7 102.1 100.9	CPS-0-60	92.0 84.3 80.1
500 1500 2000	CPS-75-20	94.6 89.6 83.2	CPS-75-60	89.0 82.2 76.9
500 1500 2000	CPSSW-0-20	104.3 101.3 100.5	CPSSW-0-60	92.7 85.8 79.1

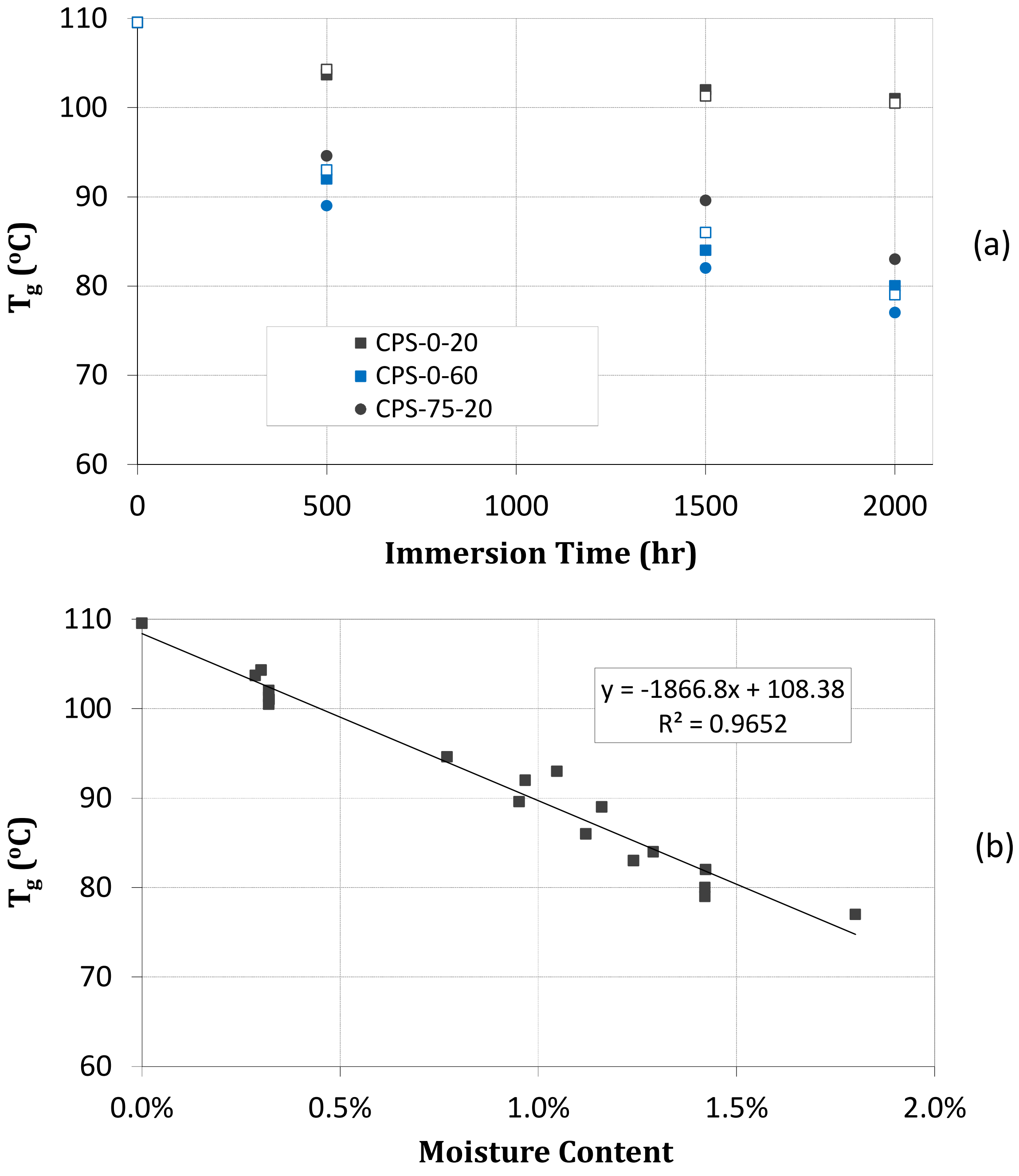

Figure 43. Glass transition temperature (T_g) of CFCC after 500, 1500, and 2000 hours of exposure: (a) T_g over time, and (b) T_g at corresponding moisture content.

4.6 Microscopic Analysis

Control and exposed specimens were examined visually using SEM to understand material microstructure and to search for microscopic effects from environmental exposure. Figure 44(a) shows one quarter of the cross-section for a control specimen, spanning 2.5 mm across (equal to the radius). There are some light scratches that were not removed during polishing, but otherwise the most notable detail is the widespread void network. Using digital measuring tools provided in the SEM controller software, the typical size of these voids was found to be 615 μm^2 and the total void content was calculated as 0.62% from a representative area. The general arrangement and condition of the microstructure for control specimens are seen in Figure 44(b). From these micrographs, the fiber content was calculated as 62.9% by volume—less than the nominal value. The small gouges in certain fibers are characteristic damage from cutting and polishing—this is very distinct from any environmental or mechanical damage.

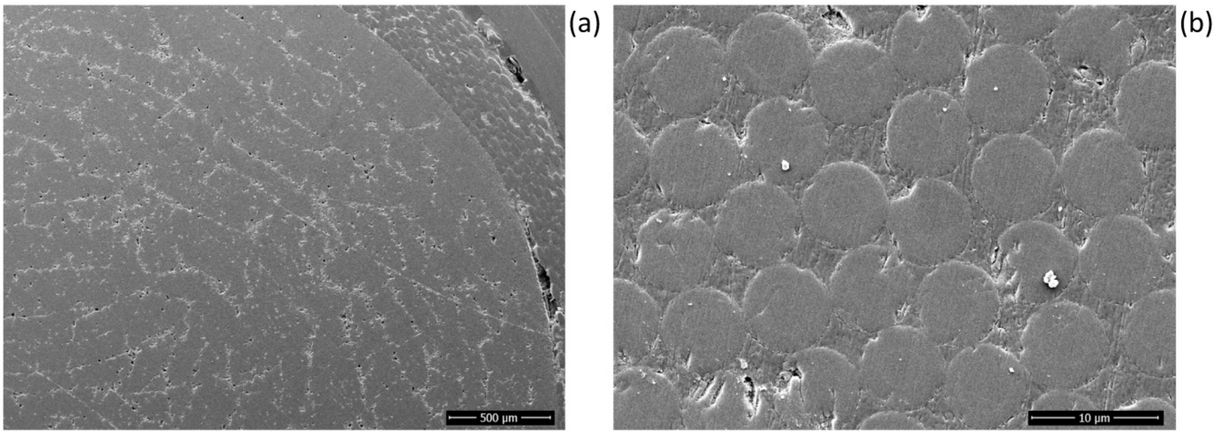

Figure 44. Micrographs of CFCC control specimens, showing (a) void network at small magnification (40X), and (b) microstructure at higher magnification (2,500X).

A valuable application for SEM is visually examining damage in materials at high resolutions, which can corroborate results from other data, such as mechanical testing and thermal analysis. Figure 45 contains representative damage for specimens exposed to all environmental conditions in this study. There are two primary forms of damage caused by these conditions: matrix microcracking, and fiber-matrix interfacial debonding. While debonding was observed in all specimens, the density and severity noticeably increased at higher temperature conditions, with very small amounts at lower temperatures. Based on the resolution achieved in these images, microcracks only seemed to develop in the higher temperature conditions and the extent of cracking was far greater for pre-loaded specimens compared to others.

It is interesting to note that most of the microcracking and interfacial debonding were observed in resin-rich areas. A likely explanation for this phenomenon is that localized moisture gradients develop in these areas due to larger relative volumes of resin, which creates moisture-induced swelling stresses until relieved by molecular relaxation. These could lead to the initiation of cracks, and the Poisson’s effect at the fiber-matrix interface—where fibers are very stiff relative to the resin—causes the matrix to pull away from the fibers.

The visual evidence found using SEM tends to strongly support the macroscopic data analyzed in Sections 4.1-4.5 at the microscale. Other techniques—like transmission electron microscopy (TEM)—could potentially yield additional information, such as the nanoscale condition of the polymer network; however, sample preparation can be very challenging for composites due to the extremely thin (< 800 nm) wafers needed to use these techniques—thus, they were beyond the study scope. The information collected in this study shows that SEM is valuable for verifying hypotheses about material degradation based on residual mechanical properties, by visually examining features indicative of macroscopic behavior.

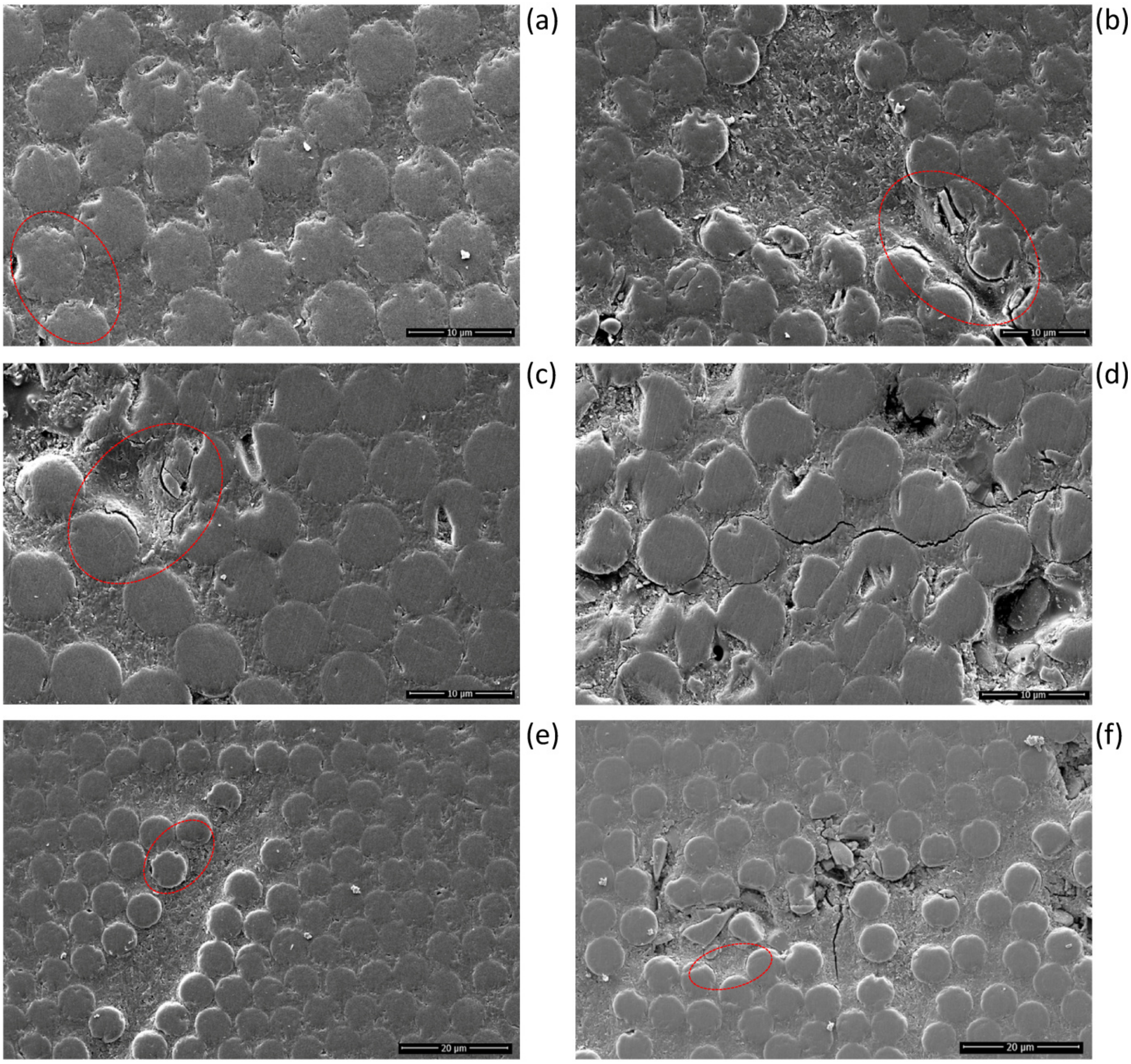

Figure 45. Various levels of damage in CFCC after exposure to different environmental conditions for 2000 hours: (a) CPS-0-20, (b) CPS-0-60, (c) CPS-75-20, (d) CPS-75-60, (e) CPSSW-0-20, and (f) CPSSW-0-60. Cracks are easily visible, and small areas of interfacial debonding are cirlced in red.

4.7 Chemical Analysis

Using the EDS technique in conjunction with SEM was a simple way to investigate the penetration of ions from the CPS and CPSSW solutions based on chemical mapping. This technique is very common and useful for analyzing metallic alloys both qualitatively and quantitatively. In this case, the chemical composition of the actual CFRP is essentially carbon, oxygen, and hydrogen so EDS can only effectively detect calcium, chlorine, and sodium ions in a more qualitative way rather than quantitative—i.e., measuring the quantitative composition of a chemical map for exposed CFRP would have little meaning since the ions are not part of the chemical structure of the CFRP. Since Ca^{2+} and Cl^- are the heaviest of the three ions, they were selected as the primary indicators of solution penetration.

Figure 46 demonstrates how 2D linescans can be combined with 3D mapping scans to understand the relative concentration of ions at various locations in the specimen. CPSSW-0-60 was selected as an example for this figure; CPS specimens simply lack Cl^- but contain similar amounts of Ca^{2+} across the surface. A faint color-coded chemical map is overlaid on the SEM micrograph in Figure 46 (left side), showing the relatively high concentrations of Cl^- (blue speckles) in resin-rich areas that are circled in red. This supports the moisture sorption results from Section 4.1, and the presence of ions in the CPS/CPSSW solutions actually makes EDS possible—pure water would only be detected by oxygen, which is already present in the CFRP so the signals would be inconclusive. Finally, results from EDS showed that the ions had penetrated completely through the specimen, which indicates that regardless of whether the material had reached moisture saturation, no discernable moisture gradients existed.

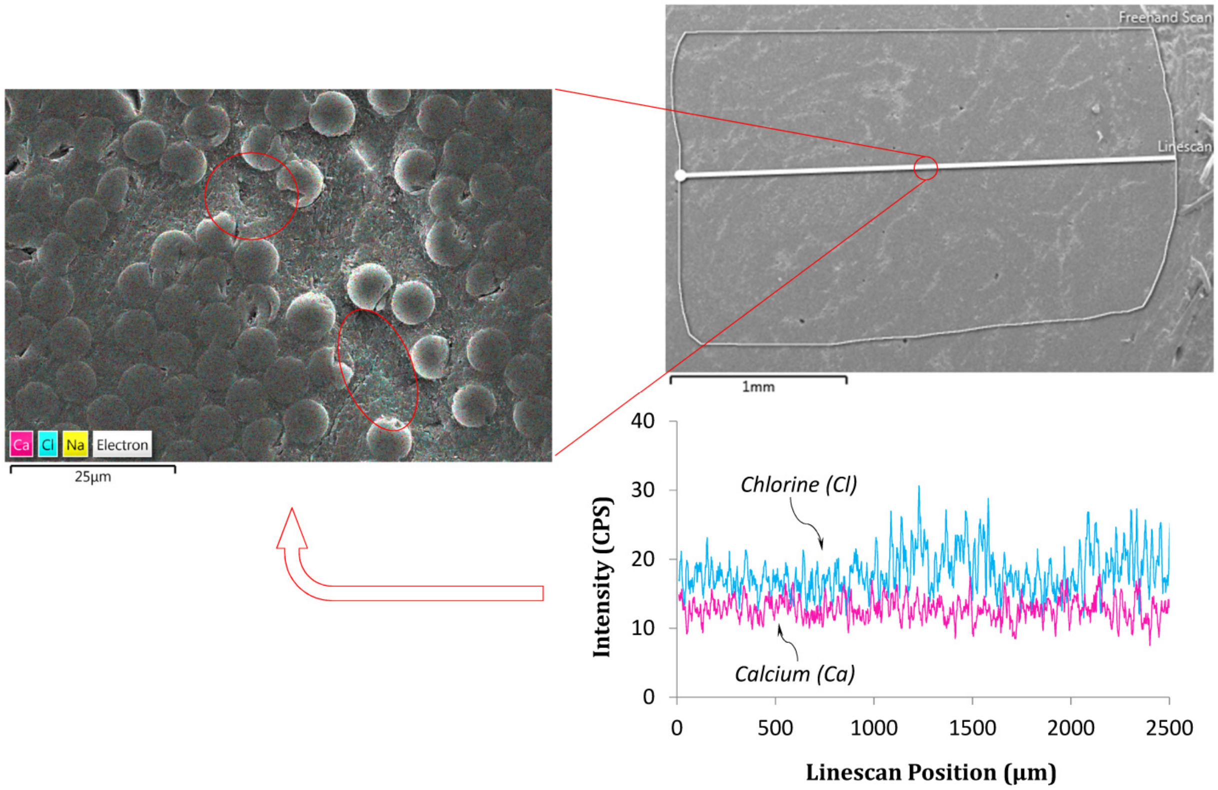

Figure 46. EDS data from CPSSW-0-60 specimens after 2000 hours of exposure, showing the combination of 2D and 3D scans: higher concentrations of Cl^- are circled in red (left).

4.8 Models for Predicting Residual Strength

Two models were implemented to describe the observed changes in mechanical properties after exposure to various environmental conditions. Their respective strengths and weaknesses are compared below, in terms of simplicity and accuracy.

4.8.1 Relaxation-Based Degradation Model

As explained in Section 2.8, the Phani-Bose model [59, 81] has been successfully applied to several FRP systems in various environments, so it was tested in this study. Since the details of the modeling theory and formulation have been described previously, the following sections only contain the procedure for obtaining model parameters and the results.

4.8.1.1 Determining Model Parameters

The procedure for obtaining model parameters is simple, with only two values needed for each environmental condition, $R_{p\infty}$ and τ. Using an error criterion—in this case, residual sum of squares (RSS)—to find the best-fit, these two parameters were selected and are listed in Tables 13-15 for all three residual strength properties—UTS, ILSS, and CIS, respectively. Similar to moisture sorption kinetics, Eq (21) can be used to understand the temperature-dependence of τ through activation energy (E_a) for CPS-0, CPS-75, and CPSSW-0 exposure conditions. Figure 47 illustrates this process by showing the exponential relationship between τ and $1/T$ to find τ_0 for $1/T = 0$, and E_a is the slope of the line from the linear relationship between $R\cdot\ln(\tau/\tau_0)$ and $1/T$; the values for τ_0 and E_a are also given in Tables 13-15.

Table 13. Summary of parameters for predicting residual UTS with the Phani-Bose model.

	CPS-0		**CPS-75**		**CPSSW-0**	
T (^{o}C)	20	60	20	60	20	60
$R_{p\infty}$ (%)	97.0	94.1	92.9	93.0	96.1	93.0
τ (10^3 hr)	10.0	3.8	6.0	2.5	9.5	4.0
τ_0 (10^3 hr)	3.175		4.101		5.642	
E_a (MJ/mol)	39.61		17.31		20.85	

Table 14. Summary of parameters for predicting residual ILSS with the Phani-Bose model.

	CPS-0		**CPS-75**		**CPSSW-0**	
T (^{o}C)	20	60	20	60	20	60
$R_{p\infty}$ (%)	96.4	90.8	89.0	82.5	94.1	88.2
τ (hr)	400	375	280	265	420	397
τ_0 (hr)	233.7		177.0		262.8	
E_a (kJ/mol)	2.169		1.718		1.775	

Table 15. Summary of parameters for predicting residual CIS with the Phani-Bose model.

	CPS-0		**CPS-75**		**CPSSW-0**	
T (^{o}C)	20	60	20	60	20	60
$R_{p\infty}$ (%)	90.8	86.5	84.4	79.8	90.2	84.7
τ (hr)	365	330	355	322	320	290
τ_0 (hr)	157.7		157.6		141.0	
E_a (kJ/mol)	4.501		4.247		4.315	

Two trends from Tables 13-15 are immediately apparent: (1) degradation of UTS requires vastly higher activation energies compared to ILSS or CIS, and (2) the influence of pre-loading and NaCl is similar to the moisture sorption kinetics, in that lower activation energy is needed for reduction in strength (UTS, ILSS, CIS). The fact that higher activation energies were required for material degradation as measured by CIS compared to ILSS, is likely due to the failure modes inherent to the Charpy impact and SBS tests—predominantly fiber pullout (interfacial debonding) with some fiber tensile failure, as opposed to predominantly delamination (interfacial debonding) with some matrix shear failure, respectively. Since higher E_a is needed to reduce UTS, which is a fiber-dominant property, it is reasonable that the minor contribution of the fibers to the failure mode of Charpy impact specimens would yield slightly higher E_a than SBS specimens, which experience only interfacial and matrix failures.

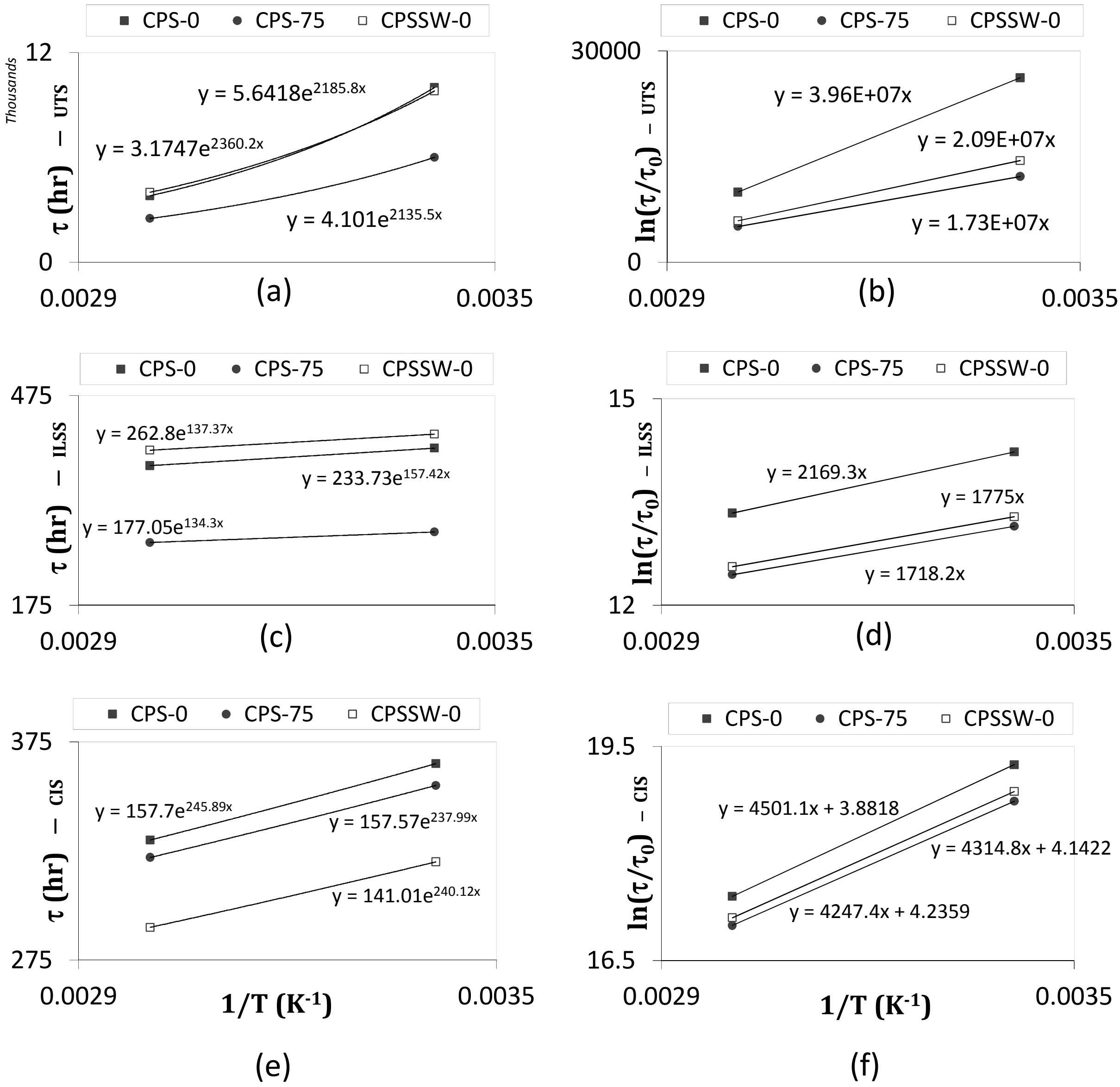

Figure 47. Arrhenius plots to determine τ_0 and E_a for (a,b) UTS, (c,d) ILSS, and (e,f) CIS.

4.8.2 Moisture-Based Degradation Model

Given the correlation observed between residual mechanical properties and moisture content, a new mechanistic model was developed here to describe moisture-induced degradation based on free volume theory and polymer physics, and calibrated with experimental data.

4.8.2.1 Framework and General Formulation

If moisture-induced degradation is the governing mechanism behind strength reductions in FRP, with negligible chemical reaction kinetics, residual strength can be predicted through a logical progression from moisture sorption to plasticization, from plasticization to softening, and from softening to weakening. The term *softening* is used to describe the thermomechanical behavior when a polymeric material loses stiffness from temperature effects, and *weakening* simply refers to the loss in strength associated with softening. Figure 48 illustrates this progression with a list of key variables that ultimately lead to deteriorated residual strength, and a diagram from Figure 8 shows the plasticization and softening processes in Figure 49. This new model has been named the **S**orption-**P**lasticization-**S**oftening-**W**eakening (SPSW) Model.

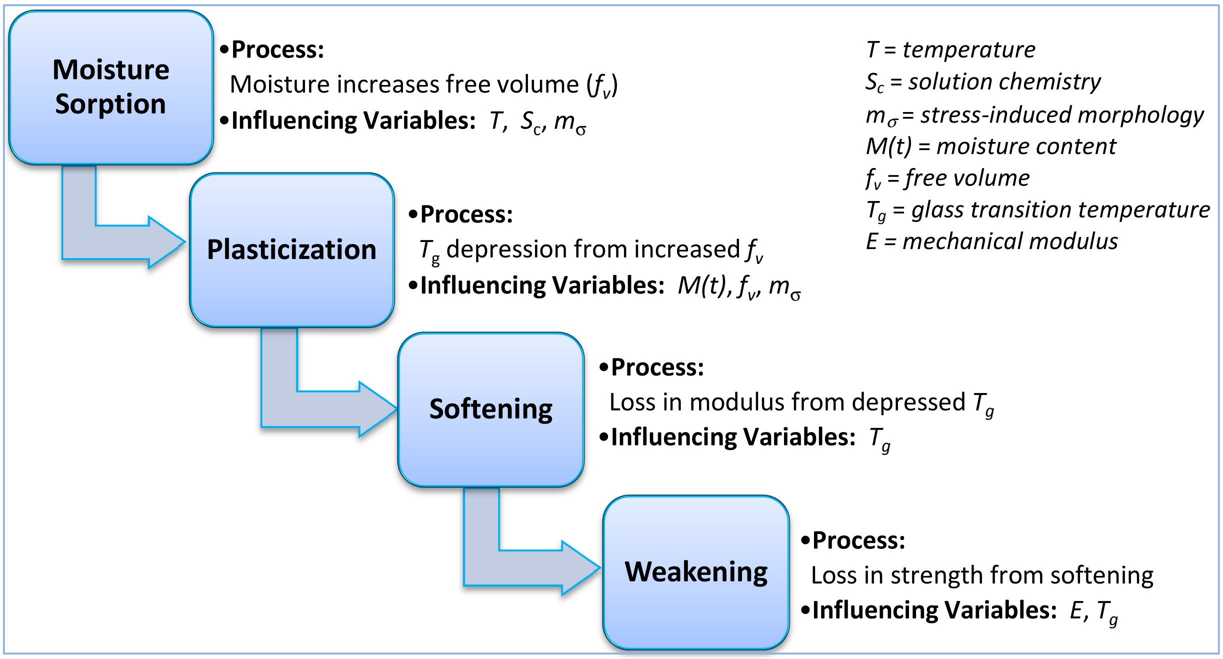

Figure 48. Framework for the moisture-based SPSW model, showing the progression from moisture sorption to strength loss.

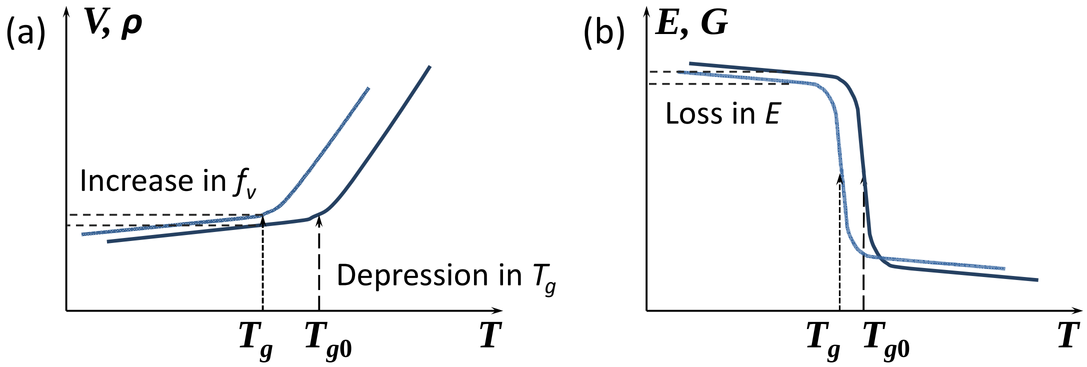

Figure 49. Schematic representation of two critical processes of the SPSW model framework in Fig. 48, showing (a) *plasticization* (T_g depression from increase in f_v), and (b) *softening* (loss in stiffness from T_g depression).

Thus, through free volume theory, the depression of T_g from plasticization can be expressed as some function of moisture content:

$$T_g = f(M) \tag{24}$$

and softening can be used to express the weakening of residual property R_p as a function of T_g:

$$R_p = g(T_g) \tag{25}$$

where both of these functions are assumed to be lower-degree polynomials. This assumption is based on the fact that an upper bound is imposed on moisture content through finite free volume in the polymer, so first- or second-degree polynomials could accurately fit these functions without the issues of extrapolating into unrealistic values—i.e., negative residual strength. The influence of parameters such as temperature, pre-loading (stress-induced morphology), and solution chemistry are accounted for in the moisture sorption kinetics (Section 4.1).

4.8.2.2 Determining Model Parameters

If T_g is best matched by a linear function of $M(t)$, then Eq (24) becomes:

$$T_g = aM + T_{g0} \tag{26}$$

and the closest fit for relating R_p to T_g is a quadratic function, so Eq (25) becomes:

$$R_p = b{T_g}^2 + cT_g + R_{p0} \tag{27}$$

where T_{g0} and R_{p0} are initial values of T_g and R_p when $M(0) = 0$, a is a constant specific to the CFCC material, and b and c are temperature-independent constants that depend on pre-loading and solution chemistry. Thus, substituting Eq (26) into Eq (27) yields the expression:

$$R_p = b(aM + T_{g0})^2 + c\left(aM + T_{g0}\right) + R_{p0} \tag{28}$$

which can be solved after substituting Eq (8), but it is too cumbersome to display here. Using linear regression to find the constants a, b, and c was a simple task, and these values are listed in Tables 16-18 for UTS, ILSS, and CIS, respectively.

Table 16. Model parameters for predicting residual UTS using the SPSW model.

	CPS-0	**CPS-75**	**CPSSW-0**
a	-1963.2	-1963.2	-1963.2
b (10^{-5} $^{o}C^{-2}$)	-0.81	-3.02	-0.20
c (10^{-3} $^{o}C^{-1}$)	2.40	6.22	1.39

Table 17. Model parameters for predicting residual ILSS using the SPSW model.

	CPS-0	**CPS-75**	**CPSSW-0**
a	-1963.2	-1963.2	-1963.2
b (10^{-4} $^{o}C^{-2}$)	0.40	0.51	1.03
c (10^{-2} $^{o}C^{-1}$)	-0.52	-0.36	-1.58

Table 18. Model parameters for predicting residual CIS using the SPSW model.

	CPS-0	CPS-75	CPSSW-0
a	-1963.2	-1963.2	-1963.2
b (10^{-4} $^{o}C^{-2}$)	2.00	1.01	2.04
c (10^{-2} $^{o}C^{-1}$)	-2.92	-1.54	-3.27

4.8.3 Prediction Results and Comparisons

The resulting predictions using the relaxation-based Phani-Bose model (Section 4.8.1) and the moisture-based SPSW model (Section 4.8.2) are shown in Figures 50-52 for the CPS-0, CPS-75, and CPSSW-0 conditions, respectively. Predictions for residual ILSS are displayed in this section; the predictions for UTS and CIS can be found in Appendix B.

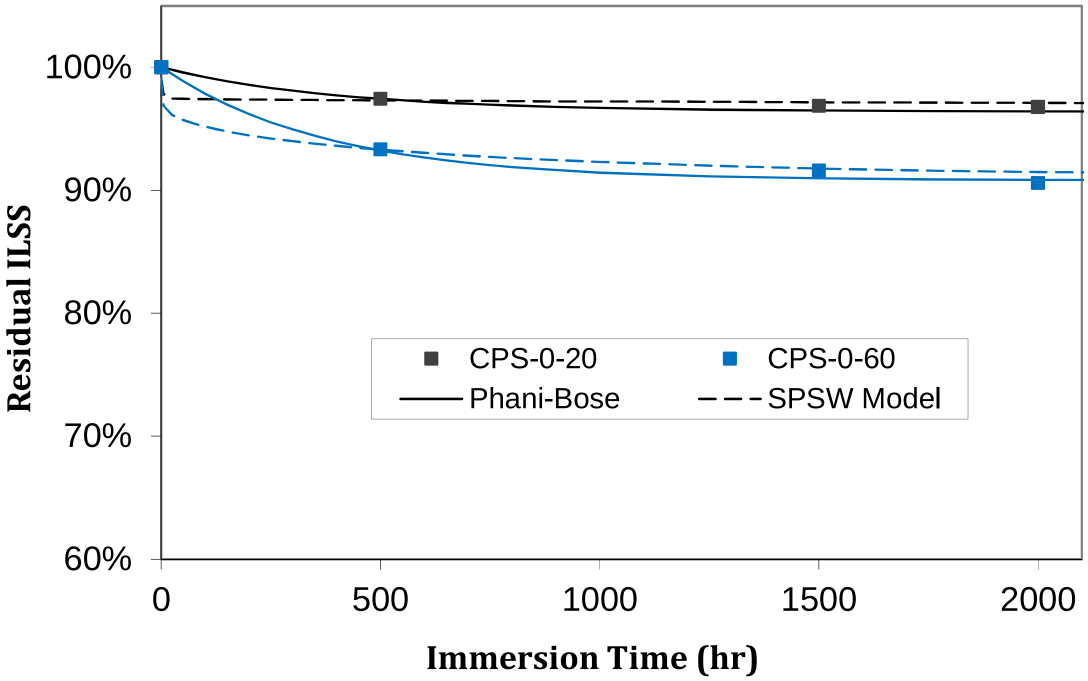

Figure 50. Model results for predicting residual ILSS for CPS-0 conditions.

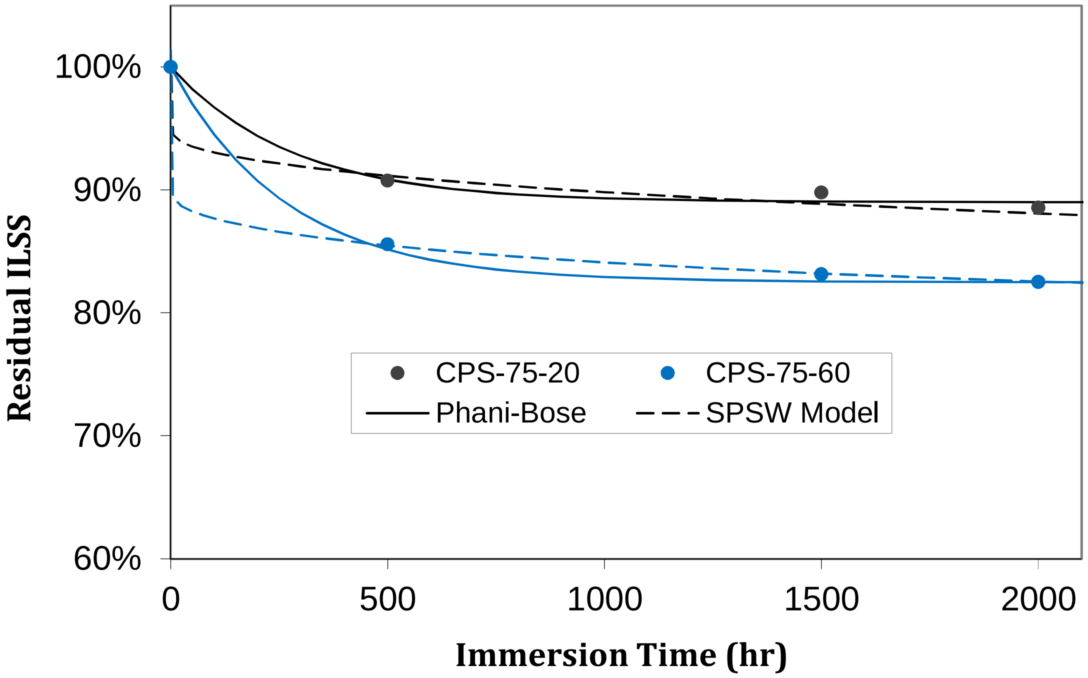

Figure 51. Model results for predicting residual ILSS for CPS-75 conditions.

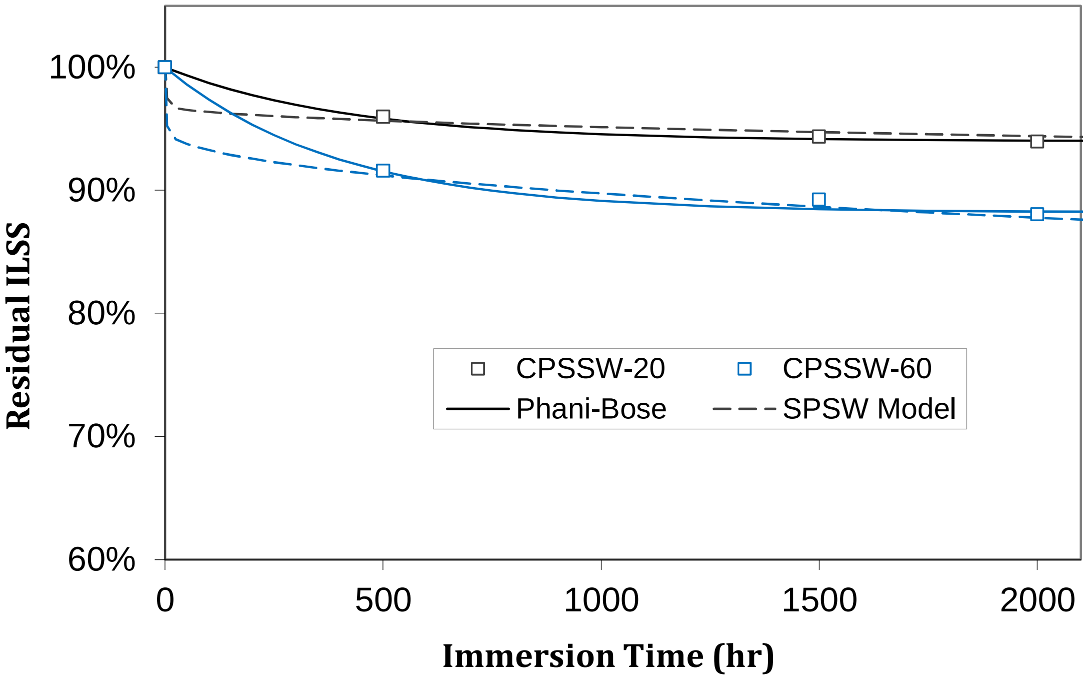

Figure 52. Model results for predicting residual ILSS for CPSSW-0 conditions.

It is obvious that both models agree with the experimental data very closely. However, there is a major difference in the shape of the decaying portion of the curves at t < 500 hours. This is because the Phani-Bose model consists of a purely exponential decay dependent on time alone, but the present SPSW model is derived from a combination of exponential and square-root decay dependent on time—originating from Eq (8). More experimental data is needed in the earlier region, for immersion times less than 500 hours. This would provide a more refined determination of the SPSW parameters that could improve the model fit at shorter durations.

In terms of mathematical simplicity, the Phani-Bose model has an advantage over the present model because only two parameters are needed (τ and $R_{p\infty}$), and they are easy to determine. The SPSW model essentially requires seven parameters (D, k, M_∞, T_{g0}, a, b, and c). However, it has an advantage over the Phani-Bose model in terms of experimental simplicity, since the process of obtaining these parameters requires fewer types of tests and specimens, relying mostly on thorough characterization of moisture sorption kinetics. For instance, τ and $R_{p\infty}$ for a given property (UTS, ILSS, CIS) must be determined for each temperature and solution of interest after several immersion durations. On the other hand, moisture parameters (D, k, M_∞) can be obtained for a range of temperatures and solutions of interest at much shorter immersion durations, and T_{g0} can be measured using DSC; lastly, the specimens from the moisture sorption tests can be used in mechanical testing to find residual properties and determine a, b, and c.

Finally, aside from simplicity and apparent accuracy, the two models differ in their fundamental basis and formulation. The phenomenological nature of the Phani-Bose model, which is based on damage caused by moisture-induced polymer relaxation, simply assumes a mathematical relationship between two phenomena and the exponential function describes that well; many processes in polymer materials can be described by exponential functions [81, 82, 88]. Also, the assumption that $R_{p\infty}$ exists, below which the strength will not drop for an indefinite amount of time, is reasonable yet very approximate. By comparison, the SPSW model essentially imposes the same restriction, but in the form of moisture saturation (M_∞). Unless conditions change, the moisture content will reach saturation after some time, and since R_p is controlled by T_g, which is controlled by $M(t)$, it logically follows that R_p will remain at a certain value for an indefinite amount of time. Thus, the SPSW model directly incorporates physical and thermomechanical mechanisms to impose a realistic restriction that the Phani-Bose model lacks.

4.8.3 Empirical Models: Comments and Shortcomings

The most basic method for closely modeling the change in mechanical properties over time for a specific environmental condition is to use best-fit linear regression to produce a matching function. Using residual UTS and modulus as an example, data is fit by linear functions of the square-root of immersion time and immersion time, respectively:

$$R_{UTS}(t) = a_{UTS}\sqrt{t} + 1 \tag{29}$$

$$R_{Mod}(t) = a_{Mod}t + 1 \tag{30}$$

where $R_{UTS}(t)$ and $R_{Mod}(t)$ are the time-dependent residual tensile strength and tensile modulus, respectively, a_{UTS} and a_{Mod} are constants, and t is immersion time. The empirical constant a is essentially the property-loss rate, which depends on environmental conditions and can vary widely. As seen in Figure 53, the results from this model agree very well with this data set; however, it lacks physical basis for describing degradation and its utility for characterization or prediction is limited to the data set for which it was constructed. Comparison between environmental conditions requires further analysis of the constant a, which has little real meaning without understanding how it influenced. It is impossible for the residual of a material property to be negative, since the limit is zero, yet Eqs (29) an (30) can yield negative values when *t* is very large. Thus, the inescapable question is how to determine the valid range of *t* for such simple linear regression models. Rather than extrapolating outside the measured data to make long-term predictions, these empirical models can be useful for accurate interpolation within the appropriate data set.

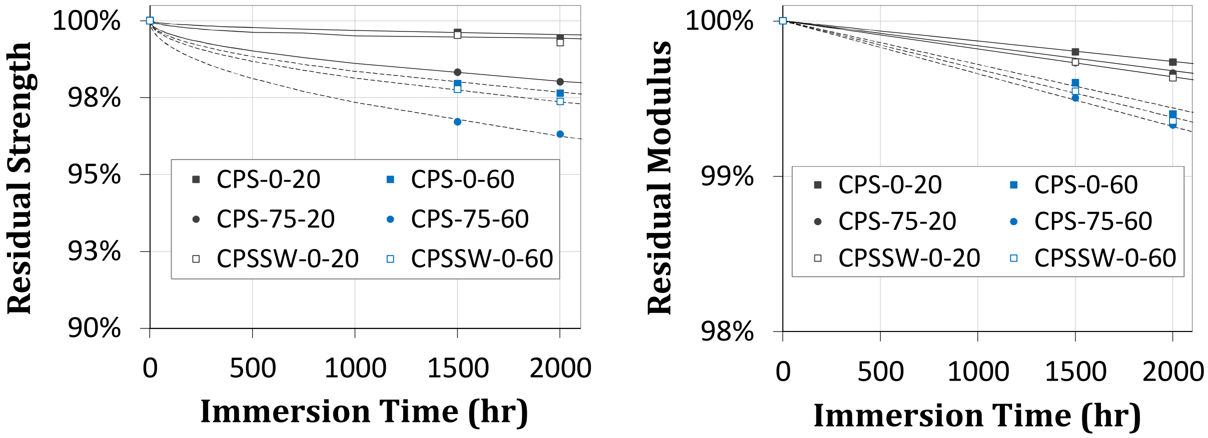

(a) (b)

Figure 53. Empirical best-fit models for (a) residual tensile strength, and (b) residual tensile modulus.

CHAPTER 5: CONCLUSIONS

The experimental program in this study was designed to provide information on two aspects of CFRP durability in a concrete environment: (1) the effects of temperature, alkaline and alkaline/salt solutions, and pre-loading on the mechanical properties of CFCC, and (2) effective techniques and analysis methods for measuring, understanding, and predicting degradation in CFRP. The results indicated that the experimental approach was executed properly, without any major outliers or anomalies, and can be considered a valid methodology for durability testing. Furthermore, a mechanistic model was developed to predict environmental degradation and it showed excellent agreement with the experimental data.

After an in-depth analysis and discussion of the findings in this study, the following conclusions were made with respect to the thesis objectives:

- Gravimetric measurements were successfully used as a simple method for characterizing moisture sorption kinetics for various environmental conditions. A two-stage Fickian model showed good agreement with the experimental data, and moisture sorption kinetics were thermodynamically described using the Arrhenius and van’t Hoff equations.
    - The rate of uptake and saturation values increased with higher temperature, and this effect was identical between the conditions without pre-loading (CPS-0 and CPSSW-0). For specimens pre-loaded to 75% UTS (CPS-75), temperature still influenced the sorption kinetics, but the stress-induced morphological changes showed greater control.

- The epoxy matrix showed no signs of chemical degradation via hydrolysis or alkali digestion. Since epoxy lacks ester groups, which are largely responsible for hydrolytic reactions in vinylesters and polyesters, this was expected.
    - The penetration of alkalis and chlorides was even confirmed by chemical analysis using EDS, yet chemical attack did not take place.

- Plasticization occurred in the epoxy as a consequence of moisture penetration, and was identified through both mechanical testing and thermal analysis. Depression of the glass transition temperature (T_g) was the most obvious sign of plasticization.
    - Differential scanning calorimetry (DSC) was a simple, convenient tool for measuring T_g and required very little training or sample preparation.

- Uniaxial tensile properties were barely affected after 2000 hours of immersion, even in the most aggressive environment (CPS-75-60). This makes sense, since these properties are fiber-dominant and the chemically-stable carbon fibers do not easily degrade from most environments. Significant losses are not expected without much longer exposure durations, or much more severe environmental conditions.
    - However, tensile properties are essential for prestressed concrete design and serviceability, warranting evaluation in this durability testing program.

- The epoxy matrix and fiber-matrix interface were more susceptible to degradation—for both accelerated and real-time conditions—and the short-beam shear (SBS) and Charpy impact (CI) tests proved to be more effective methods of comparing the effects of environmental conditions.

    - The correlation between SBS and CI test results demonstrated that they both capture similar information about the deteriorated condition of CFRP, with similar sensitivities to environmental effects. If the ILSS is not specifically required, CIS can be measured instead using the much more convenient CI test.

- Microscopic examination of the CFRP using SEM provided a wealth of qualitative data on the material microstructure, condition after exposure, and failure mechanisms after testing. This technique helped explain and support macroscopic observations made through mechanical testing and thermal analysis.
    - Interfacial debonding was found in growing amounts for the six conditions tested, in the following order (lowest to highest): CPS-0-20, CPSSW-0-20, CPS-75-20, CPS-0-60, CPSSW-0-60, and CPS-75-60. Additionally, matrix cracking was present in all except CPS-0-20 and CPSSW-0-20, and was most severe in CPS-75-60. Plasticization was responsible for these forms of damage in all specimens, and stress effects were a major cause for pre-loaded CFRP.

- Two models were compared for predicting residual strength in CFRP: the relaxation-based phenomenological Phani-Bose model, and a moisture-based mechanistic SPSW model developed in this study. Both models showed excellent agreement with the experimental data available at this time, but thorough validation was not possible without residual strength data from immersion durations less than 500 hours.
    - While the Phani-Bose model is simpler to implement and requires only two parameters, the SPSW model has the advantage of relying on moisture content alone, without the need to doubly account for various temperatures or other

environmental effects in the mechanical testing. Moisture sorption is the backbone of the model and specific, observable physical and thermomechanical mechanisms are represented in the formulation.

The influence of temperature, alkaline and alkaline/chloride solutions, and temporary tensile stress were investigated and their individual and combined effects were understood through a methodical experimental program. Furthermore, the experimental findings were supported by theories and observations from thermodynamics and physical chemistry. Finally, a new model was developed to predict degradation of mechanical properties for CFRP based on the effects of moisture, which reduces the variables needed for accurate predictions.

CHAPTER 6: FUTURE WORK

There are two key limitations in this study that should be addressed in future work:

1. Longer exposure durations are needed to verify findings from short-term exposure results, which will improve accelerated durability testing programs;
2. The effects of sustained tensile stress should be included in the environmental conditions from this thesis, in order to extend the current understanding about temporary tensile stress (pre-loading) effects.

In the case of durability testing programs employed by transportation agencies for evaluating or accepting certain CFRP prestressing materials, longer exposure durations are impractical. In fact, reliable short-term exposure methodologies are essential for these organizations, since they must feel comfortable with the material's behavior and the laboratory testing associated with it. On the other hand, academic and industrial research efforts are very suitable for long-term studies that could produce crucial real-time durability data for validating and improving accelerated durability testing methods and predictive models.

As noted in Chapter 2, most of the research found in the literature about the influence of sustained stress on environmental durability of FRP is focused on one of the following: materials other than carbon fiber (e.g., GFRP), flexural stress rather than tensile stress, or very low stress levels (< 50% UTS). These results are not closely related to CFRP for prestressed concrete bridge applications, wherein sustained tensile stresses of 65-75% UTS are involved. Therefore, future studies should examine the influence of higher sustained tensile stresses in CFRP to simulate a prestressed concrete environment more realistically.

REFERENCES

[1] W. H. Hartt and M. Rapa, "Condition Assessment of Jackets Upon Pilings for Florida Bridge Substructures," Florida Department of Transportation, Tallahassee, 1998.

[2] E. J. C. E. X. S. N.F. Grace, "Life-Cycle Cost Analysis of Carbon Fiber-Reinforced Polymer Reinforced Concrete Bridges," *ACI Structural Journal*, 2012.

[3] FHWA, "Innovative Bridge Research and Construction Project Database," Washington, 2012.

[4] V. Karbhari, "Use of Composite Materials in Civil Infrastructure in Japan," International Technology Research Institute, 1998.

[5] L. Hollaway, "A review of the present and future utilisation of FRP composites in the civil infrastructure with reference to their important in-service properties," *Construction and Building Materials*, vol. 24, pp. 2419-2445, 2010.

[6] V. M. Karbhari, J. W. Chin, D. Huston, B. Benmokrane, T. Justka, R. Morgan, J. J. Lesko, U. Sorathia and D. Reynaud, "Durability gap analysis for fiber-reinforced polymer composites in civil infrastructure," *Journal of Composites for Construction,* vol. 7, no. 3, pp. 238-247, 2003.

[7] M. A. L. L. V. K. C Helbling, "Issues of variability and durability under synergistic exposure conditions related to advanced polymer composites in the civil infrastructure," *Composites Part A*, vol. 37, pp. 1102-1110, 2006.

[8] C. T. Herakovich, Mechanics of Fibrous Composites, New York: John Wiley & Sons, Inc., 1998.

[9] X. Huang, "Fabrication and properties of carbon fibers," *Materials*, vol. 2, pp. 2369-2403, 2009.

[10] T. Roberts, "The carbon fiber industry: Global strategic market evaluation 2006-2010," Materials Technology Publications, Watford, UK, 2006.

[11] P. J. Walsh, "Carbon Fibers," in *ASM Handbook*, ASM International, 2001, pp. 35-40.

[12] D. D. Edie, "The effect of processing on the structure and properties of carbon fibers," *Carbon*, vol. 36, pp. 345-362, 1998.

[13] D. Ratna, Handbook of Thermoset Resins, Shawbury: Smithers, 2009.

[14] C. Hall, "Polymer Engineering," in *ICE Manual of Construction Materials*, Institute of Civil Engineers, 2009, pp. 579-584.

[15] A. J. Oshinski, H. Keskkula and D. R. Paul, "Rubber toughening of polyamides with functionalized block copolymers: 1. Nylon-6," *Polymer*, vol. 33, no. 2, pp. 268-283, 1992.

[16] I. K. Varma, B. S. Rao, M. S. Choudhary, V. Choudhary and D. S. Varma, "Effect of styrene on properties of vinyl ester resins," *Die Angewandte Makromolekulare Chemie,* vol. 130, no. 1, pp. 191-199, 1985.

[17] J. Koyanagi, S. Ogihara, H. Nakatani, T. Okabe and S. Yoneyama, "Mechanical properties of fiber/matrix interface in polymer matrix composites," *Advanced Composite Materials,* vol. 23, no. 5-6, pp. 551-570, 2014.

[18] C. Kuttner, A. Hanisch, H. Schmalz, M. Eder, H. Schlaad, I. Burgert and A. Fery, "Influence of the polymeric interphase design on the interfacial properties of (fiber-reinforced) composites," *(ACS) Applied Materials & Interfaces,* vol. 5, pp. 2469-2478, 2013.

[19] J. Koyanagi, H. Nakatani and S. Ogihara, "Comparison of glass-epoxy interface strengths examined by cruciform specimen and single-fiber pull-out tests under combined stress state," *Composites Part A,* vol. 43, no. 11, pp. 1819-1827, 2012.

[20] R. E. Swain, K. L. Reifsnider, K. Jayaraman and M. El-Zein, "Interface/interphase concepts in composite material systems," *Journal of Thermoplastic Composite Materials,* vol. 3, pp. 13-23, 1990.

[21] Strongwell, Inc., "The Pultrusion Process," Strongwell, Inc., 2015. [Online]. Available: www.strongwell.com/about/the-pultrusion-process/. [Accessed 2015].

[22] S. Montserrat, "Effect of crosslinking density on ΔCp(Tg) in an epoxy network," *Polymer,* vol. 36, no. 2, pp. 435-436, 1995.

[23] D. Leveque, A. Schieffer, A. Mavel and J.-F. Maire, "Analysis of how thermal aging affects the long-term mechanical behavior and strength of polymer-matrix composites," *Composites Science and Technology,* vol. 65, pp. 395-401, 2005.

[24] G. M. Odegard and A. Bandyopadhyay, "Physical aging of epoxy polymers and their composites," *Journal of Polymer Science Part B,* vol. 49, no. 24, pp. 1695-1716, 2011.

[25] T. S. Gates and M. A. Grayson, "On the use of accelerated aging methods for screening high temperature polymeric composite materials," *AIAA,* vol. 2, pp. 925-935, 1999.

[26] J. W. Chin, K. Aouadi and T. Nguyen, "Sorption and diffusion of water, salt water, and concrete pore solution in composite materials," *Journal of Applied Polymer Science,* vol. 1, pp. 483-492, 1999.

[27] J. W. Chin, K. Aouadi, M. R. Haight, W. L. Hughes and T. Nguyen, "Effects of water, salt solution and simulated concrete pore solution on the properties of composite matrix resins used in civil engineering applications," *Polymer Composites,* vol. 22, no. 22, pp. 282-298, 2001.

[28] P. Scott and J. M. Lees, "Uptake swelling and thermal expansion of CFRP tendons," *Structures and Buildings,* vol. 162, pp. 263-273, 2009.

[29] P. Scott and J. M. Lees, "Effects of solution exposure on the combined axial-shear

behaviour of unidirectional CFRP rods," *Composites Part A,* vol. 43, pp. 1599-1611, 2012.

[30] F. Micelli and A. Nanni, "Durability of FRP rods for concrete structures," *Construction and Building Materials,* vol. 18, pp. 491-503, 2004.

[31] S. P. Pilli and L. V. Smith, "Measuring time-dependent diffusion in polymer matrix composites," *Mechanics of Time-Dependent Materials,* 2012.

[32] S. Roy, W. Xu, S. Park and K. Liechti, "Anomalous moisture diffusion in viscoelastic polymers: Modeling and testing," *Journal of Applied Mechanics,* vol. 67, pp. 391-396, 2000.

[33] L.-R. Bao and A. Yee, "Effect of temperature on moisture absorption in a bismaleimide resin and its carbon fiber composites," *Polymer,* vol. 43, pp. 3987-3997, 2002.

[34] L. Li, S.-Y. Zhang, Y.-H. Chen, M.-J. Liu, Y.-F. Ding, X.-W. Luo, Z. Pu, W.-F. Zhou and S. Li, "Water transport in epoxy resin," *Chemistry of Materials,* vol. 17, pp. 839-845, 2005.

[35] L.-R. Bao and A. Yee, "Moisture diffusion and hygrothermal aging in bismaleimide matrix carbon fiber composites--part I: Uni-weave composites," *Composites Science and Technology,* vol. 62, pp. 2099-2110, 2002.

[36] Z. Lu, G. Xian and H. Li, "Effects of thermal aging on the water uptake behavior of pultruded BFRP plates," *Polymer Degradation and Stability,* vol. 110, pp. 216-224, 2014.

[37] D.-W. Suh, M.-K. Ku, J.-D. Nam, B.-S. Kim and S.-C. Yoon, "Equilibrium water uptake of epoxy/carbon fiber composites in hygrothermal environmental conditions," *Journal of Composite Materials,* vol. 35, no. 3, pp. 264-278, 2001.

[38] M. Autran, R. Pauliard, L. Gautier, B. Mortaigne, F. Mazeas and P. Davies, "Influence of mechanical stresses on the hydrolytic aging of standard and low styrene unsaturated polyester composites," *Journal of Applied Polymer Science,* vol. 84, pp. 2185-2195, 2002.

[39] A. Aniskevich, A. Mintzas and R. Guedes, "Stress-strain analysis of specimens subjected to tensile loading during moisture uptake," in *16th European Conference on Composite Materials (ECCM16),* Seville, 2014.

[40] D. Klepach and T. I. Zohdi, "Strain assisted diffusion: Modeling and simulation of deformation-dependent diffusion in composite media," *Composites Part B,* vol. 56, pp. 413-423, 2014.

[41] Y. J. Weitsman and M. Elahi, "Effects of fluids on the deformation, strength and durability of polymeric composites -- An overview," *Mechanics of Time-Dependent Materials,* vol. 4, pp. 107-126, 2000.

[42] D. A. Bond and P. A. Smith, "Modeling the transport of low-molecular-weight penetrants within polymer matrix composites," *Applied Mechanics Reviews,* vol. 59, no. 5, pp. 249-268, 2006.

[43] G. Marom and L. J. Broutman, "Moisture penetration into composites under external stress," *Polymer Composites,* vol. 2, no. 3, pp. 132-136, 1981.

[44] P. Scott and J. M. Lees, "Water, salt water and alkaline solution uptake in epoxy thin films," *Journal of Applied Polymer Science,* vol. 130, no. 3, pp. 1898-1908, 2013.

[45] H. G. Carter and K. G. Kibler, "Langmuir-type model for anomalous moisture diffusion in composite resins," *Journal of Composite Materials,* vol. 12, pp. 118-131, 1978.

[46] A. A. Fahmy and J. C. Hurt, "Stress dependence of water diffusion in epoxy resin," *Polymer Composites,* vol. 1, no. 3, pp. 77-80, 1980.

[47] B. C. Ray, "Temperature effect during humid ageing on interfaces of glass and carbon fibers reinforced epoxy composites," *Journal of Colloid and Interface Science,* vol. 298, pp. 111-117, 2006.

[48] S. Ito, M. Hashimoto, B. Wadgaonkar, N. Svizero, R. Carvalho, C. Yiu, F. Rueggeberg, S. Foulger, T. Saito, N. Yoshihiro, M. Yoshiyama, F. Tay and D. Pashley, "Effects of resin hydrophilicity on water sorption and changes in modulus of elasticity," *Biomaterials,* vol. 26, pp. 6449-6459, 2005.

[49] J. Yagoubi, G. Lubineau, A. Traidia and J. Verdu, "Monitoring and simulations of hydrolusis in epoxy matrix composites during hygrothermal aging," *Composites Par A,* vol. 68, pp. 184-192, 2014.

[50] D. Powers, "Interaction of Water with Epoxy," Sandia National Laboratories, Albuquerque, 2009.

[51] S. Pimenta and S. Pinho, "Recycling carbon fibre reinforced polymers for structural applications: Technology review and market outlook," *Waste Management,* vol. 31, pp. 378-392, 2011.

[52] H. Sembokuya, Y. Negishi, M. Kubouchi and K. Tsuda, "Corrosion behavior of epoxy resin cured with different amount of hardener in corrosive solutions," *Materials Science Research International,* vol. 9, no. 3, pp. 230-234, 2003.

[53] J. A. Nairn, "Matrix Microcracking in Composites," in *Polymer Matrix Composites,* vol. 2, London, Elsevier Science, 2000, pp. 403-432.

[54] E. Totry, C. Gonzalez and J. LLorca, "Prediction of the failure locus of C/PEEK composites under transverse compression and longitudinal shear through computational micromechanics," *Composites Science and Technology,* vol. 68, no. 15-16, pp. 3128-3136, 2008.

[55] E. Totry, C. Gonzalez and J. LLorca, "Failure locus of fiber-reinforced composites under transverse compression and out-of-plane shear," *Composites Science and Technology,* vol. 68, no. 3-4, pp. 829-839, 2008.

[56] D. Arencon and J. I. Velasco, "Fracture toughness of polypropylene-based particulate composites," *Materials,* vol. 2, pp. 2046-2094, 2009.

[57] J. Koyanagi, M. Nakada and Y. Miyano, "Prediction of long-term durability of unidirectional CFRP," *Journal of Reinforced Plastics and Composites,* vol. 30, no. 15, pp.

1305-1313, 2011.

[58] J. Koyanagi, S. Yoneyama, A. Nemoto and J. Melo, "Time and temperature dependence of carbon/epoxy interface strength," *Composites Science and Technology,* vol. 70, pp. 1395-1400, 2010.

[59] Y. Chen, "Accelerated Ageing Tests and Long-term Prediction Models for Durability of FRP Bars in Concrete," West Virginia University, Morgantown, 2007.

[60] C. Helbling, M. Abanilla, L. Lee and V. Karbhari, "Issues of variability and durability under synergistic exposure conditions related to advanced polymer composites in the civil infrastructure," *Composites Part A,* vol. 37, pp. 1102-1110, 2006.

[61] ASTM Standard D7502-11, "Standard Test Method for Tensile Properties of Fiber Reinforced Polymer Matrix Composite Bars," ASTM International, West Conshohocken, 2011.

[62] ASTM Standard D7617-11, "Standard Test Method for Transverse Shear Strength of Fiber-reinforced Polymer Matrix Composite Bars," ASTM International, West Conshohocken, 2011.

[63] ASTM Standard D4475-02, "Standard Test Method for Apparent Horizontal Shear Strength of Pultruded Reinforced Plastic Roads By the Short-Beam Method," ASTM International, West Conshohocken, 2008.

[64] ASTM Standard D7264-07, "Standard Test Method for Flexural Properties of Polymer Matrix Composite Materials," ASTM International, West Conshohocken, 2007.

[65] M. S. Vinod, B. J. Sunil, V. Nayaka, R. Shenoy, M. S. Murali and A. Nafidi, "Fractography of compression failed carbon fiber reinforced plastic composite laminates," *Journal of Mechanical Engineering Research,* vol. 2, no. 1, pp. 1-9, 2010.

[66] K. Kellogg, A. Kallmeyer, R. Chinnam and P. Dutta, "Influence of moisture and low temperature on notched Izod impact toughness in a pultruded reinforced composite," in *9th International Offshore and Polar Engineering Conference (ISOPE-9),* Brest, 1999.

[67] E. Sideridis and G. Papadopoulos, "Short-beam and three-point-bending tests for the study of shear and flexural properties in unidirectional-fiber-reinforced epoxy composites," *Journal of Applied Polymer Science,* vol. 93, pp. 63-74, 2004.

[68] F. Abali, A. Pora and K. Shivakumar, "Modified short beam shear test for measurement of interlaminar shear strength of composites," *Journal of Composite Materials,* vol. 37, pp. 453-464, 2003.

[69] P. Yeung and L. Broutman, "The effect of glass-resin interface strength on the impact strength of fibre reinforced plastics," *Polymer Engineering and Science,* vol. 18, no. 2, pp. 62-72, 1978.

[70] M. Bader, J. Bailey and I. Bell, "The effect of fibre-matrix interface strength on the impact and fracture properties of carbon-fibre-reinforced epoxy resin composites," *Journal of*

Physics D, vol. 6, pp. 572-590, 1973.

[71] M. Bader and R. Ellis, "The effect of notches and specimen geometry on the pendulum impact strength of uniaxial CFRP," *Composites,* vol. Nov, pp. 253-258, 1974.

[72] A. Fernandez-Canteli, A. Aguelles, J. Vina, M. Ramulu and A. Kobayashi, "Dynamic fracture toughness measurements in composites by instrumented Charpy testing: Influence of aging," *Composites Science and Technology,* vol. 62, pp. 1315-1325, 2002.

[73] Z. Jin and C.-T. Sun, Fracture Mechanics, London: Elsevier, 2011.

[74] M. Robert and B. Benmokrane, "Physical, mechanical, and durability characterization of preloaded GFRP reinforcing bars," *Journal of Composites for Construction,* vol. 14, pp. 368-375, 2010.

[75] V. Karbhari and G. Xian, "Hygrothermal effects on high Vf pultruded unidirectional carbon/epoxy composites: Moisture uptake," *Composites Part B,* vol. 40, pp. 41-49, 2009.

[76] Agilent Technologies, "Agilent 4100 ExoScan FTIR - Operations Manual," Agilent Technologies, Inc., Malaysia, 2013.

[77] W. Dang, M. Kubouchi, H. Sembokuya and K. Tsuda, "Chemical recycling of glass fiber reinforced epoxy resin cured with amine using nitric acid," *Polymer,* vol. 46, pp. 1905-1912, 2005.

[78] S. Cotugno, D. Larobina, G. Mensitieri, P. Musto and G. Ragosta, "A novel spectroscopic approach to investigate transport processes in polymers: The case of water-epoxy system," *Polymer,* vol. 42, pp. 6431-6438, 2001.

[79] M. Liu, P. Wu, Y. Ding, G. Chen and S. Li, "Two-dimensional (2D) ATR-FTIR spectroscopic study on water diffusion in cured epoxy resins," *Macromolecules,* vol. 35, pp. 5500-5507, 2002.

[80] Oxford Instruments, "AZtec User Manual," Oxford Instruments, London, 2013.

[81] K. Phani and N. Bose, "Hydrothermal ageing of CSM-laminate during water immersion - an acousto-ultrasonic study," *Journal of Materials Science,* vol. 21, pp. 3633-3637, 1986.

[82] C. Roland, "Characteristic relaxation times and their invariance to thermodynamic conditions," *Soft Materials,* vol. 4, pp. 2316-2322, 2008.

[83] G. Pritchard and S. Speake, "The use of water absorption kinetic data to predict laminate property changes," *Composites,* vol. 14, pp. 227-232, 1987.

[84] I. Nishizaki and I. Sasaki, "Long-term durability of FRP cables under maritime conditions," in *5th International Conference on FRP Composites in Civil Engineering (CICE 2010),* Beijing, 2010.

[85] ACI Committee 440, "Accelerated Conditioning Protocols for Durability Assessment of Internal and External Fiber Reinforced Polymer (FRP) Reinforcement for Concrete,"

American Concrete Institute, Farmington Hills, 2014.

[86] B. Hayden and P. Michaels, "Virginia's Climate," University of Virginia, Charlottesville, 2014.

[87] J. Tanks, C. Tan and S. Sharp, "Micro-scale characterization of carbon fiber reinforced polymer composites: Observations, challenges, and practical guidelines," in *Composites and Advanced Materials Expo (CAMX 2014)*, Orlando, 2014.

[88] A. S. Maxwell, W. R. Broughton, G. Dean and G. D. Sims, "Review of accelerated ageing methods and lifetime prediction techniques for polymeric materials," National Physical Laboratory, Teddington, 2005.

APPENDIX A: ADDITIONAL TEST RESULTS

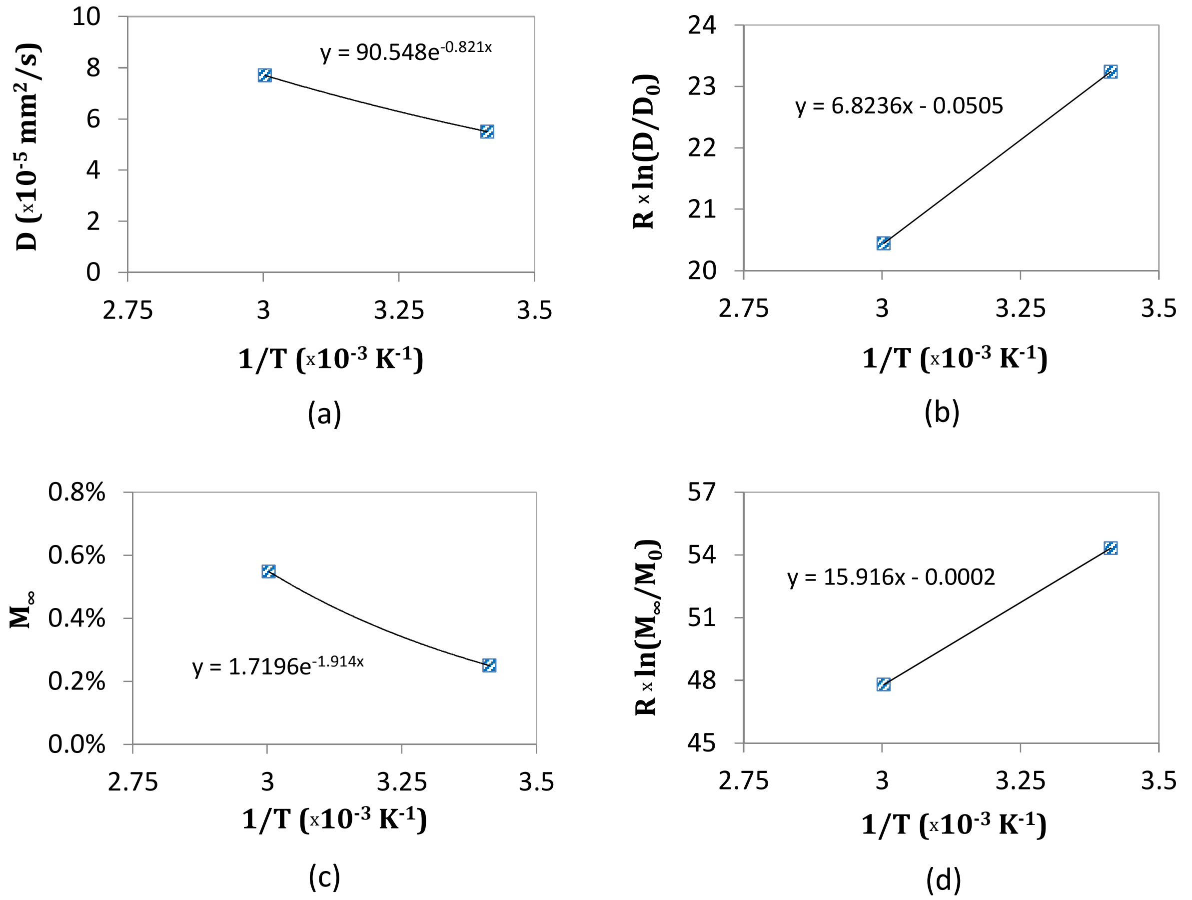

(a) (b)

(c) (d)

Figure 54. Two-stage model parameters for CPS-75 environments calculated for (a,b) E_a using Arrhenius equation, and (c,d) ΔH_{abs} using van't Hoff's equation.

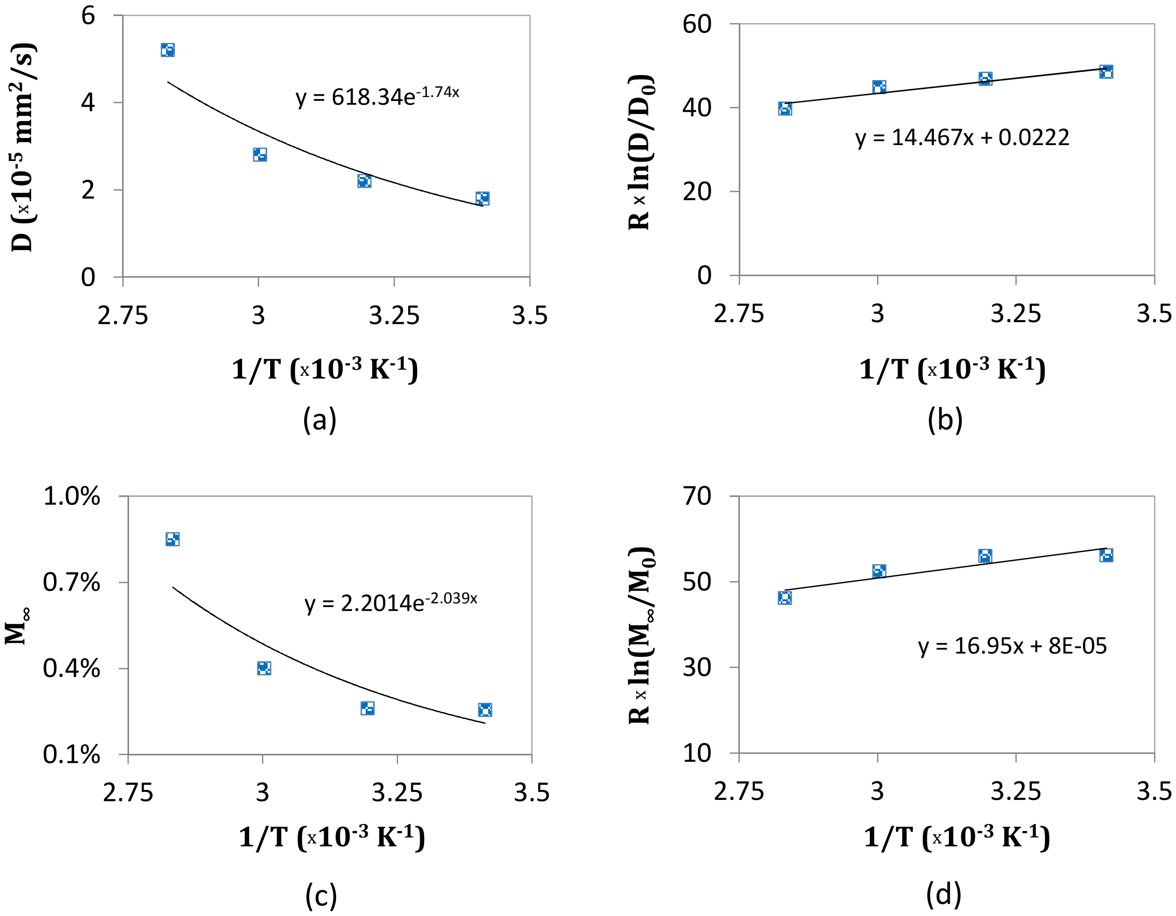

(a)

(b)

(c)

(d)

Figure 55. Two-stage model parameters for CPSSW-0 environments calculated for (a,b) E_a using Arrhenius equation, and (c,d) ΔH_{abs} using van't Hoff's equation.

APPENDIX B: ADDITIONAL MODEL RESULTS

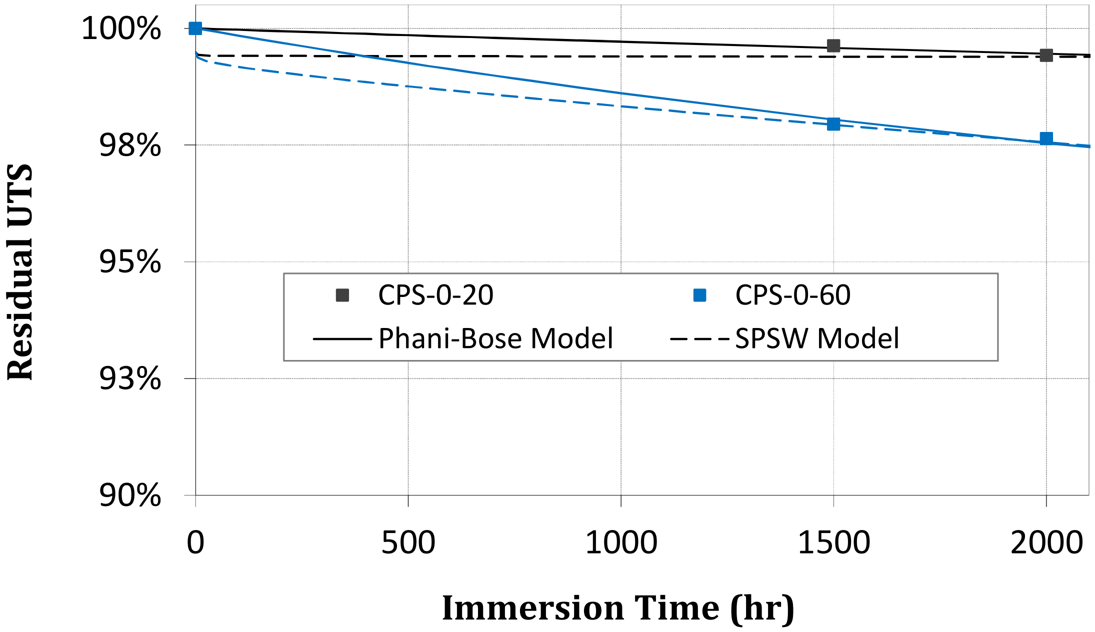

Figure 56. Model results for predicting residual UTS for CPS-0 conditions.

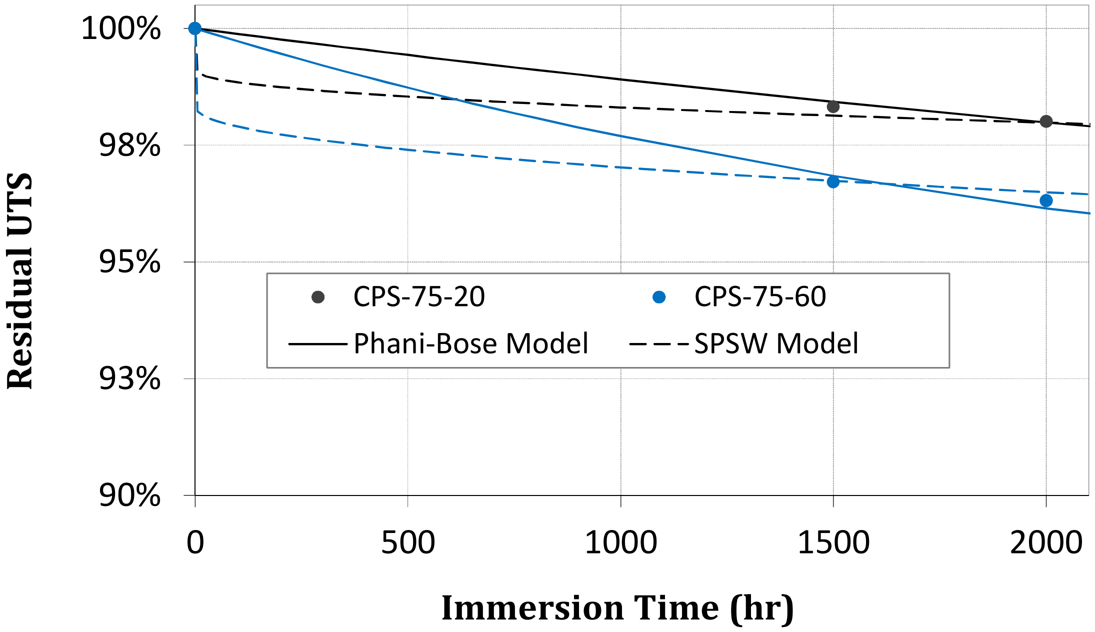

Figure 57. Model results for predicting residual UTS for CPS-75 conditions.

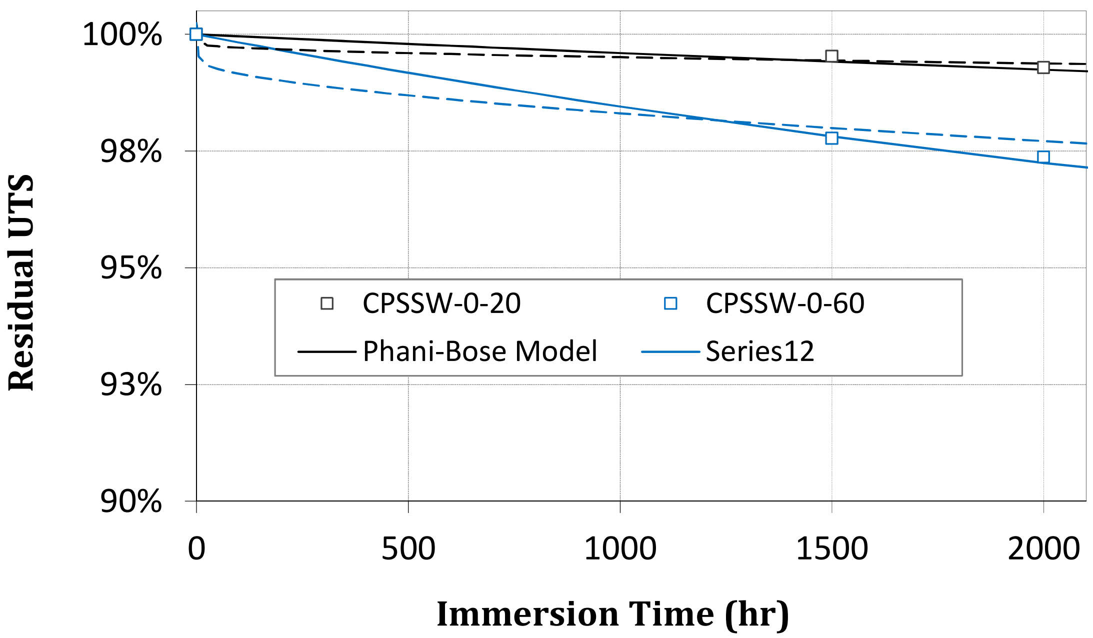

Figure 58. Model results for predicting residual UTS for CPSSW-0 conditions.

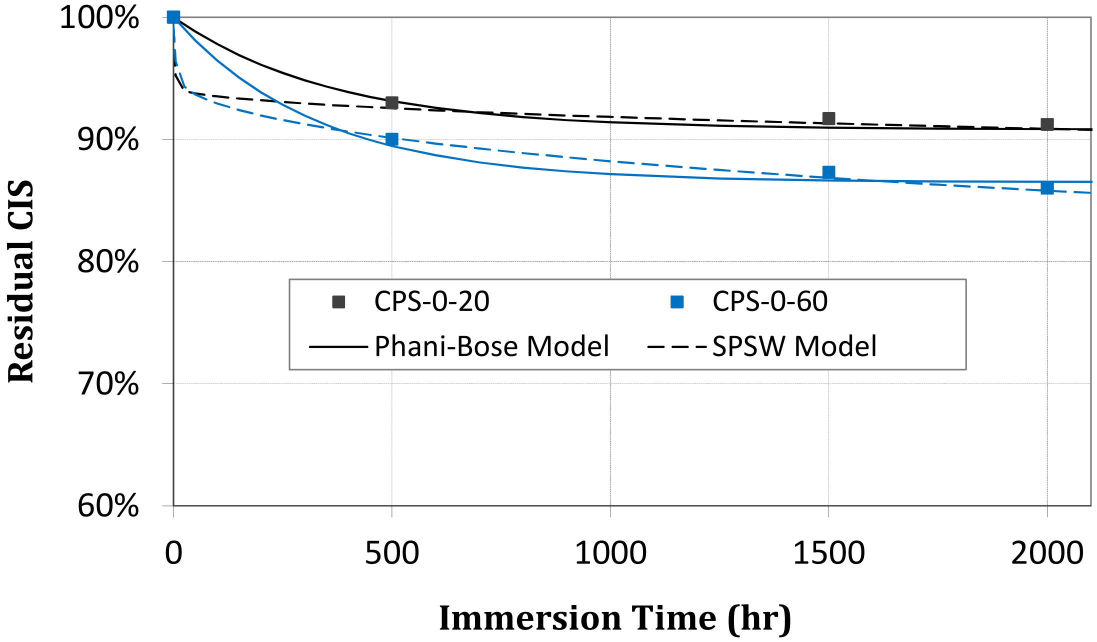

Figure 59. Model results for predicting residual CIS for CPS-0 conditions.

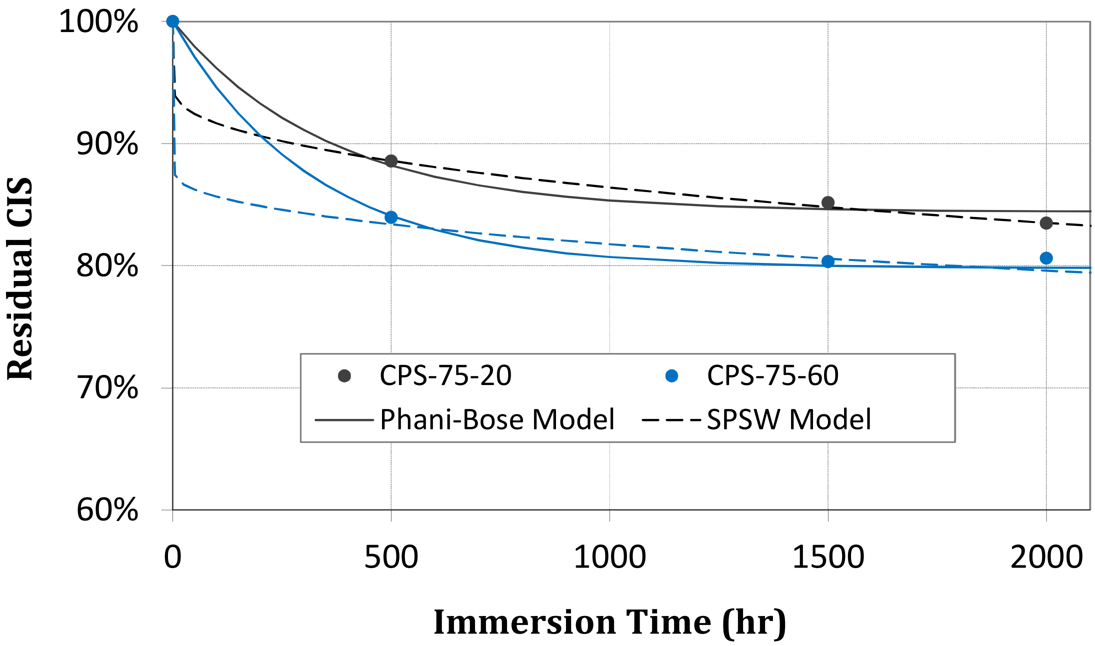

Figure 60. Model results for predicting residual CIS for CPS-75 conditions.

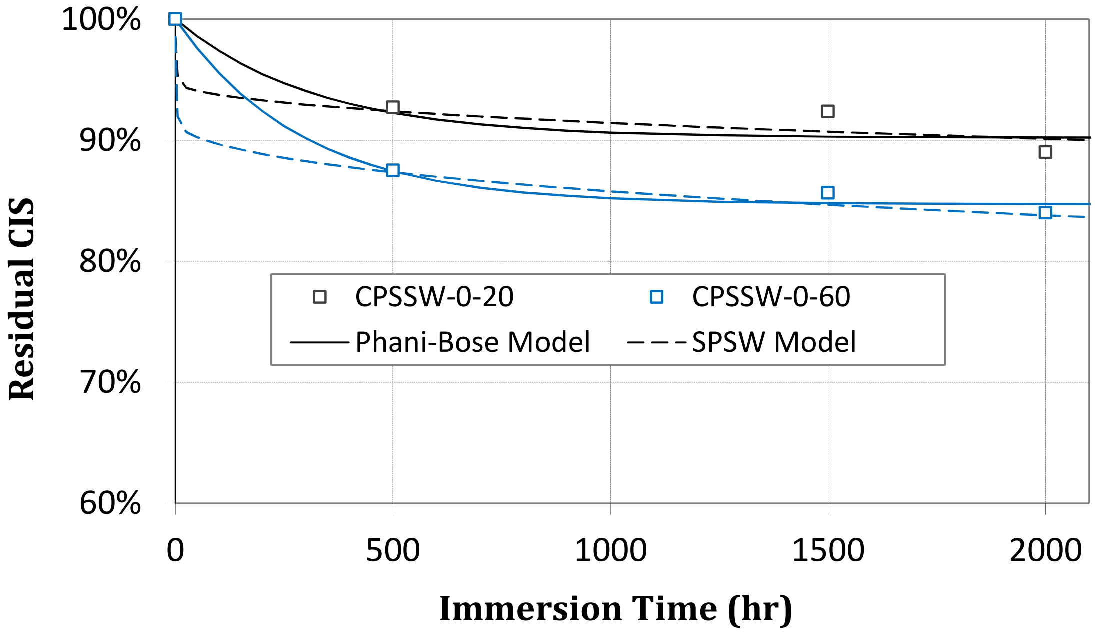

Figure 61. Model results for predicting residual CIS for CPSSW-0 conditions.